Depth Scanning Correlation Interferometric Microscopy for Label-Free Nanoparticle Detection

by

Uğur Aygün

A Dissertation Submitted to the
Graduate School of Sciences and Engineering
in Partial Fulfillment of the Requirements for
the Degree of

Doctor of Philosophy

in

Electrical and Electronics Engineering

KOÇ
UNIVERSITY

01 02, 2020

Depth Scanning Correlation Interferometric Microscopy for Label-Free Nanoparticle Detection

Koç University

Graduate School of Sciences and Engineering

This is to certify that I have examined this copy of a doctoral dissertation by

Uğur Aygün

and have found that it is complete and satisfactory in all respects,

and that any and all revisions required by the final

examining committee have been made.

Committee Members:

Prof. Dr. Hakan Ürey

Asst. Prof. Ayça Yalçın Özkumur

Prof. Dr. Alper Kiraz

Assoc. Prof. Onur Ferhanoğlu

Asst. Prof. Ahmet Can Erten

Asst. Prof. Serap Aksu Ramazanoglu

Date:

to my beloved wife and family

ABSTRACT

Detection of biological nanoparticles such as virus, protein aggregates or exosomes is critical for disease diagnosis and treatment monitoring applications, and for the development of novel biomarkers. Specifically, exosomes, cell derived vesicles, emerged as potential biomarkers for early detection of cancer and neurodegenerative diseases. Optical detection of these biological nanoparticles is quite challenging due to their small size and low refractive index contrast. Although fluorescence labeling based detection methods have emerged in recent years, these techniques rely on utilization of secondary probe molecules, which increases the complexity of the sample preparation. In addition to requiring complex labeling procedures, fluorescence-based detection also suffers from photo-blinking, bleaching and saturation. Label-free detection of nanoparticles overcomes these problems as well as provides the information about the intrinsic properties of the particles such as size and dielectric index. Wide-field interferometric microscopy is a label-free method that allows visualization of nanosized particles, however it has several drawbacks such as limited sensitivity and sizing capability, and false interpretations of the results due to spatial variations of the surface capture probe density.

In this thesis, we introduce two different interferometric detection systems to address the challenges present in interferometric microscopy. First, we introduce a low-cost interferometric biosensor developed by modifying a commercial flatbed scanner.

We demonstrated the DNA hybridization and DNA-directed antibody immobilization in a microarray format, with a scan time of 10 seconds for an area of 4 mm x 4mm area (scalable to the size of an A4 paper). The developed system can be used for characterizing the capture probe density on sample substrate prior to biological nanoparticle detection experiments or can be used as a standalone biosensor, especially in low-resource settings. Secondly, we show that sensitivity (minimum detectable size) of interferometric microscopy can be improved by utilizing unique defocus response of nanoparticles. We developed the novel depth scanning correlation (DSC) interferometric microscopy technique, where depth scans are captured and correlation analysis on a pixel-by-pixel basis is performed using post-processing. We demonstrated detection of polystyrene nanoparticles smaller than 30 nm with a wide field of view of 300 μm x 200 μm. Furthermore, by applying Bayesian approach (prior knowledge) in the data analysis pipeline, characterization of the particles can be performed in a more robust way. A physical model for the interferometric nanoparticle images is applied to the acquired data through Markov Chain Monte Carlo (MCMC) analysis to estimate the particle parameters. Moreover, as potential applications, detection of exosomes isolated from the tumor cells and visualization of neutrophil extracellular traps (NETs) in a label-free format is demonstrated.

ÖZETÇE

Virüs, protein veya eksozom gibi biyolojik nanoparçacıkların algılanması hastalık teşhisi, tedavi sürecinin izlenmesi ve yeni biyoayıraçların geliştirilmesi için önemlidir. Özellikle, hücrelerden salınan eksozomlar son yıllarda kanser ve nörodejeneratif hastalıkların erken teşhisi için önem kazanmıştır. Bu parçacıkların optik yöntemler kullanılarak algılanması, küçük boyutları ve düşük kırınım indisi kontrastından dolayı oldukça zordur. Son yıllarda floresan etiketler kullanımına dayalı çeşitli algılama yöntemleri geliştirilmesine rağmen, bu yöntemler ikincil bir ayıraç kullanımını gerektirmekte, bu durum da örnek hazırlama prosedürlerini karmaşıklaştırmaktadır. Bunun yanı sıra floresan etiket temelli algılayıcılar, fototoksisite, sönümlenme ve ışık doygunluğu gibi etkenlerden olumsuz olarak etkilenmektedir. Etiketsiz algılama yöntemleri bu gibi sorunlardan etkilenmediği gibi, parçacıkların boyu ve dielektrik indisi gibi parametreler hakkında da bilgi sağlamaktadır. Etiketsiz bir yöntem olan genişalanlı interferometrik mikroskopi tekniği nanoboyutlu parçacıkların görüntülenmesine olanak tanımaktadır. Fakat bu teknik kısıtlı hassasiyet, kısıtlı boyut ölçüm kapasitesi ve yüzey tutucu miktarındaki değişkenler nedeniyle sonuçların yanlış yorumlanması gibi sorunlara sahiptir.

Bu tezde, bu sorunların çözümü için iki ayrı interferometrik algılama sistemi önerilmiştir. İlk olarak, döküman tarayıcısının modifiye edilmesiyle elde edilen düşük maliyetli bir interferometrik biyoalgılayıcı tanıtılacaktır. 10 saniyede 4mm x 4mm (A4

döküman boyuna ölçeklenebilir), geliştirilen biyoalgılayıcıyla mikrodizi formatında DNA hibritleşmesi ve DNA yardımlı antikor bağlanması gösterilmiştir. Geliştirilen bu sistem tek başına bir biyoalgılayıcı olarak kullanılabilmesinin yanında, mikrodizi deneylerinden önce yüzey tutucu antikorların karakterize edilmesi için de kullanılabilir. İkinci olarak, interferometrik mikroskoplarda hassasiyetin (algılanabilecek en küçük parça boyutu), odak dışı görüntülerin analiz edilmesiyle arttırılabileceğini gösterilmiştir. Geliştirdiğimiz özgün bir yöntem derinlik taramalı korelasyon interferometrik miktoskobuyla, 30 nm çapındaki polistiren parçacıklar, 300 μm x 200 μm boyutlarında bir görüş alanda algılanmıştır. Bunun yanında, Bayez analizinin (ön bilgi), veri işleme aşamasında kullanılmasıyla daha sağlam bir şekilde parçacık karakterizasyonunun yapılabileceği gösterilecektir. Fiziksel bir modelin, elde edilen nanoparçacık interferometrik mikroskop verisine Markov Zinciri Monte Carlo yöntemiyle eklenmesi ile birlikte parçacık parametrelerinin tahmin edilmesi sağlanacaktır. Ek olarak, tümör hücrelerinden ayrıştırılan eksozomların algılanması ve nötrofil hücre dışı tuzaklarının görüntülenmesi, biyolojik uygulamalar olarak gösterilecektir

ACKNOWLEDGMENTS

Firstly, I would like to express my gratitude to my advisors Hakan Ürey and Ayça Yalçın Özkumur for their continuous support, guidance and encouragement throughout my research journey. Prof. Ürey's deep enthusiasm for scientific research was a motivation source for me to explore new ideas. He created a productive research environment at Optical Microsystems Laboratory and I was lucky to be a part of it. I would like to express deep gratitude to Dr. Ayça Yalçın Özkumur for her continuous support during my PhD studies, despite the time difference between Boston and Istanbul. She gave me a chance to work on this fascinating area. I would like to thank for her valuable time, effort and great advices.

I would like to thank my progress committee members Prof. Alper Kiraz and Prof. Onur Ferhanoğlu for their valuable comments and suggestions throughout my PhD studies. I would like to thank thesis committee members Prof. Ahmet Can Erten and Prof. Serap Aksu Ramazanoğlu for their valuable time and feedback.

During all these years, I was lucky to work with the experts of the field. A special thanks to Prof. M. Selim Ünlü for introducing me interferometric imaging and guiding my work in this area, Prof. Utkan Demirci and Prof. Gözde Durmuş for their valuable comments and support in exosome project, Prof. Crispin Barnes for teaching me the basics of experimental design and data analysis and allowing me to work in his laboratory at the University of Cambridge and Prof. Füsun Can for her support in NETs project.

I would like to express my gratitude to Dr. Barış Yağcı, Dr. Elif Seymour, Dr. Oğuzhan Avci, Dr. Adrian Ionescu, Sven Holmstrom and Selim Ölçer for their technical and intellectual contributions in various projects.

I would like to thank all past and present members of Optical Microsystems Laboratory for creating an excellent research and fun environment. I thank Kıvanç Hedili, Ulaş Adıyan, Erdem Ulusoy, Deniz Mengü, Burak Soner, Yusuf Samet Yaraş, Shoaib Soomro, Mahdi Kazempourradi, Soheila Kharratiankhameneh, Gökhan Sağlam, Osman Eldeş, Ali Cem, Koray Kavaklı, Emre Heves, Fehmi Çivitçi, Onur Çakmak and Gamze Yılmaz. Special thanks to my friend Burak Gurlek for our long conversations about science.

Last but not least, I would like to thank my family for their unconditional love and support. My parents for supporting me in all of my pursuits and raising me with a love of science. My sister for her unconditional support on all areas of my life. Finally, my wife for the endless love, support and encouragement. Nothing would be possible without their support.

TABLE OF CONTENTS

LIST OF TABLES

LIST OF FIGURES

NOMENCLATURE

CCD: Charge-Coupled Device

cfDNA: Circulating free DNA

CIS: Contact Image Sensor

CMOS: Complementary Metal Oxide Semiconductor

COBRI: Coherent Brightfield Microscopy

DDI: DNA-Directed Immobilization

DHM: Digital Holographic Microscopy

DSC: Depth Scanning Correlation

ELISA: Enzyme-Linked Immunosorbent Assay

GPU: Graphics Processing Unit

GRIN: Gradient-Index

IRIS: Interferometric Reflactance Imaging Sensor

iSCAT: Interferometric Scattering

LED: Light Emitting Diode

LUT: Look-up Table

MCMC: Markov Chain Monte Carlo

MEMS: Microelectromechanical System

MH: Metropolis Hastings

NA: Numerical Aperture

NETs: Neutrophil Extracellular Traps

NTA: Nanoparticle Tracking Analysis

OPD: Optical Path Difference

PALM: Photoactivated Localization Microscopy

PBS: Phosphate-Buffered Saline

SEM: Scanning Electron Microscopy

SMR: Suspended Microchannel Resonator

SNR: Signal to Noise Ratio

SP-IRIS: Single Particle Interferometric Reflectance Imaging Sensor

SPR: Surface Plasmon Resonance

SSC: Saline-Sodium Citrate

STED: Stimulated Emission Depletion

STORM: Stochastic optical reconstruction Microscopy

stroboSCAT: Stroboscopic Scattering Microscopy

UV: Ultraviolet

WGM: Whispering Gallery Mode

Chapter 1

INTRODUCTION

1.1 Motivation

The term nanoparticle corresponds to particles having at least one dimension on the order of 100 nm or less [1]. In recent decades, advancements in nanotechnology allowed the utilization of nanoparticles in a wide range of areas including biotechnology [2], cosmetics [3], food industry[4], commercial electronics [5] and various industrial applications [6]. One of the challenges in nanoparticle use is the requirements of sensitive characterization tools. Also, the potential hazardous effects of nanoparticles raised concerns as their use grows [7]. Because of their size, nanoparticles can easily penetrate the body through air-blood barrier and could affect the biological processes inside cells [8]. Engineered nanoparticles can be responsible for different types of lung and cardiovascular diseases [9]. Not only the size, but also the shape, concentration and material characteristics are important for the determination of toxicity characteristics of these particles [10]. Thus, sensitive quantification techniques are required.

Quantification of naturally occurring biological nanoparticles such as viruses, vesicles and protein aggregates is also critical both for both understanding of the governing dynamics of molecular interactions and for developing applications for areas such as disease diagnostics [11], treatment monitoring [12] and discovery of new biomarkers [13]. As experienced in recent Zika and Ebola outbreaks, rapid detection of viruses is important [14]. Beside viruses, exosomes, have attracted considerable interest due to their potential applications in early diagnosis, such as cancer [15] and neurodegenerative diseases [16].

Conventional characterization methods provide ensemble averaged (analog) information of the samples. However, individual assessment of the particles separately is critical due to the heterogeneity among particles. Single particle level characterization allows us to sense small variations between the particles, that can be lost in ensemble measurements. Furthermore, the concentration of the most promising biomarkers is below than the detection limit of currently available biosensors. Hence, to improve the sensitivity limit, single particle (digital) detection is required [17] (Figure 1.1).

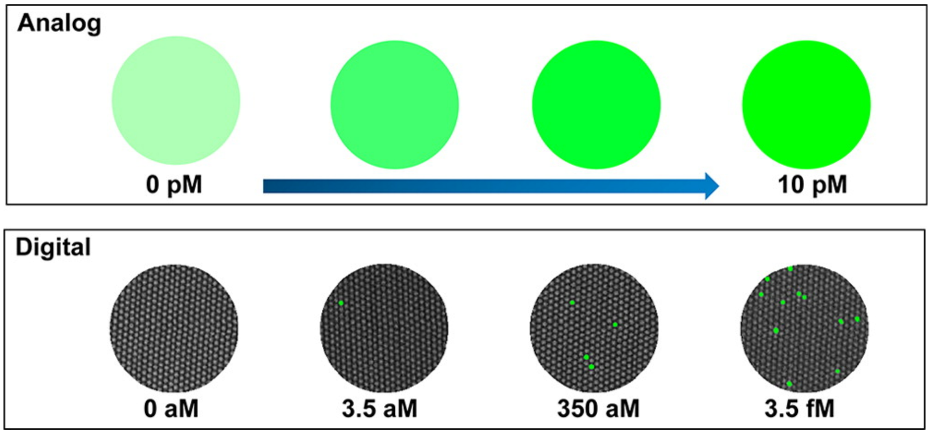

Figure 1.1: Digital Detection vs Analog Detection. In order to sense biomolecules at low concentration single particle detection is required [17].

According to their detection principle biosensors can be divided into different categories namely, optical, mechanical or electrical. Biosensors can also be classified on whether they use labels or not. Labeled techniques uses secondary labels to enhance the molecular signals, while in label-free techniques detect biomolecular interactions directly. In this chapter we will review the characterization techniques under two groups to better explain how common their use is in biological nanoparticle characterization. In the first group are the conventional techniques which found general use in laboratories. The second group consists of emerging techniques which have been specifically developed for biological particle detection but have not been translated to clinical use.

1.2 Conventional Methods for Biological Nanoparticle Detection

1.2.1 Fluorescence Microscopy

Fluorescence microscopy provides high contrast images of the sample by eliminating any background light. Sub-diffraction limited images of fluorophore tagged nano-sized structures can be acquired by using superresolution microscopy techniques such as STED [18, 19, 20], STORM [21, 22] or PALM [23], However, these techniques require labelling of the particles which can alter the state of the particles [24, 25]. Furthermore, these advanced imaging techniques have low throughput. Hence their potential is limited for biosensing applications in which detecting and counting the nanoparticles of interest over a large field of view is often desired [26].

1.2.2 Electron Microscopy

Electron microscopy uses electrons to visualize samples. Due to diffraction limit, resolution of the acquired images is limited by the wavelength of the illumination.

Wavelength of electrons is smaller, which makes them useful for acquiring high resolution images of biological specimens, in contrast to optical microscopes. However, electron microscopes require complex instrumentation as imaging is done with electrons, hence they are bulky and costly. Moreover, this method is low throughput, and its practical utilization in clinical settings is insufficient.

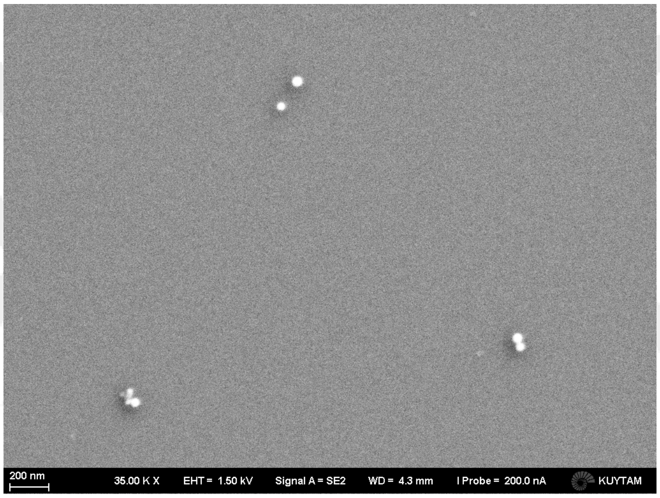

Figure 1.2: Electron Microscopy Image of Polystyrene Nanoparticles. Electron microscopy provides high resolution images of nanosized particles with a limited field of view. Scalebar is 200 nm.

1.2.3 Nanoparticle Tracking Analysis

Nanoparticle Tracking Analysis (NTA) is a measurement method which is widely employed for determination of the size distribution of the particles suspended in a liquid [27]. Depending on the viscosity and temperature of the solution, particles drift in Brownian motion. In NTA instruments, sample solution is illuminated with a laser beam, and scattered light is collected with an optical system and captured with a camera as shown in Figure 1.3.Then, captured images are processed to determine particle size distribution by solving Stokes-Einstein equations [28].

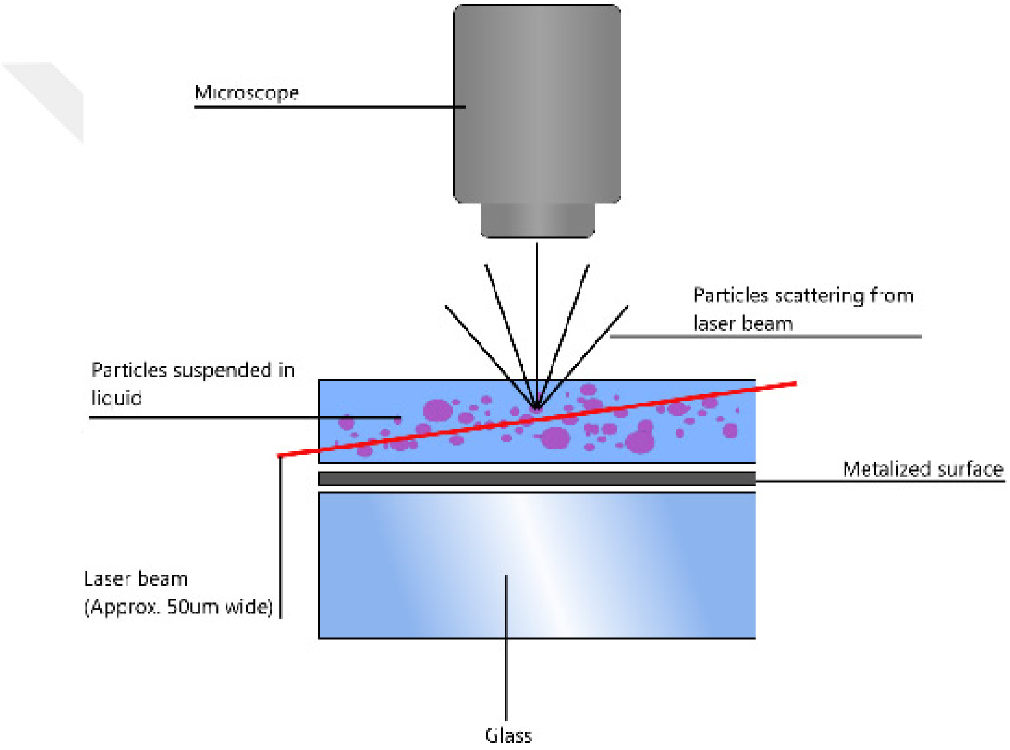

Figure 1.3: Nanosight NTA Working Principle. Sample is illuminated with a laser beam, and scattered light is collected. Temporal behaviour is analysed to determine size distribution of the sample. Figure is taken from [29]

Although NTA instruments are widely used for characterization of samples, this technique does not provide any information about the content of the particles without using any labels. Moreover, this method provides only ensemble averaged information, single particle level characterization is not possible.

1.3 Emerging Methods for Single Nanoparticle Detection

1.3.1 Mechanical Biosensing Platforms

Advanced mechanical biosensing platforms utilize the microelectromechanical system (MEMS) technology. Change in resonance frequency, phase or deflection can be measured according to detection mode of the microcantilevers after biomolecules bind to them. Sensitivity of MEMS biosensor is mainly related to the quality factor (Q-factor) of the resonator. Although high Q-factors can be achieved in air or vacuum, biosensing applications require operating in liquid. Another problem associated with these sensors is that the response is highly sensitive to the binding position which makes quantification challenging. These problems are well addressed in work by Manalis group [30]. They introduced a new type of mechanical biosensor called Suspended Microchannel Resonator (SMR) [31]. Microfluidic channels are embedded in the cantilever, which ensures that the resonator can be operated in vacuum conditions. Using this technique gold particles with 10 nm and exosomes with 39 nm in diameter can be detected with a Q factor of 22000 (Figure 1.4). However, this technique requires calibration steps for each cantilever individually.

1.3.2 Surface Plasmon Resonance Biosensors

Surface Plasmon Resonance (SPR) sensors are widely employed in chemical and biological sensing. The idea of SPR sensing is based on measuring the change of the resonance characteristics of the surface plasmons, oscillation of free electrons in dielectric-metal interface. Resonance excitation of the surface plasmon waves is sensitive to local

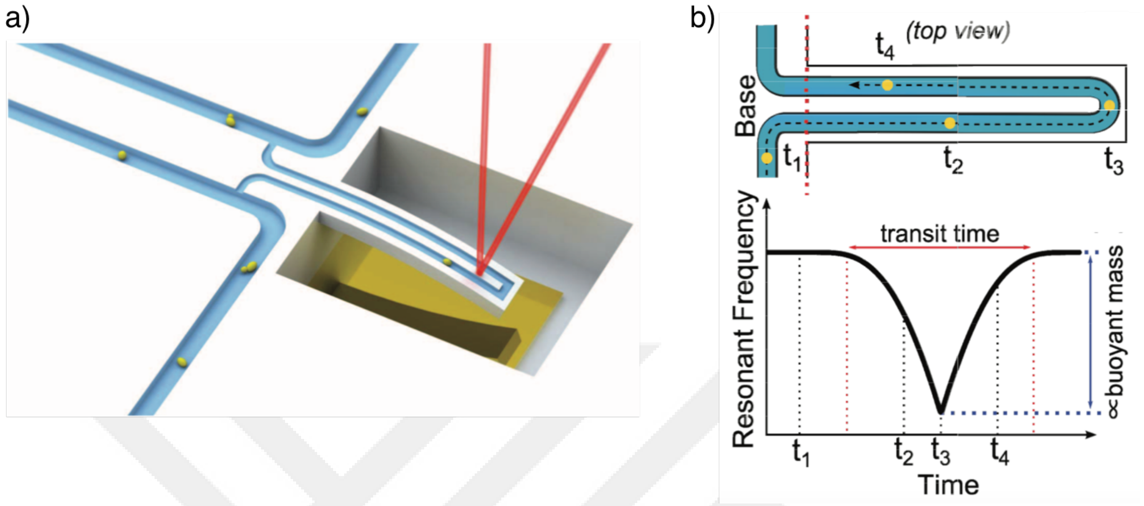

Figure 1.4: Illustration of Suspended Microchannel Resonator (SMR) for detection of single nanoparticles.(a) Microchannels are embedded in the cantilever (b) Resonance frequency changes depending on the position of the nanoparticle flowing inside the microchannel [32]

refractive index, which is modified by the binding of the biomolecules in biosensing applications. Although several commercial SPR biosensors are available, sensitivity level of these biosensors is not adequate to detect the nanoparticles individually. Wang et al. [33], demonstrated the detection of single virus and nanoparticles with 98 nm diameter. In a recent work, real time detection of polystyrene particles is achieved [34]. Sensitivity levels can be improved by modifying the metal coated surface. By implementing nanoscale antennas to localize surface plasmon waves Zhang et al. could detect single nanoparticles with 20 nm in diameter [35]. However, this technique requires complex fabrication of nanoantennas. Moreover, sensitivity is highly dependent on binding position and the determination of particle size is challenging.

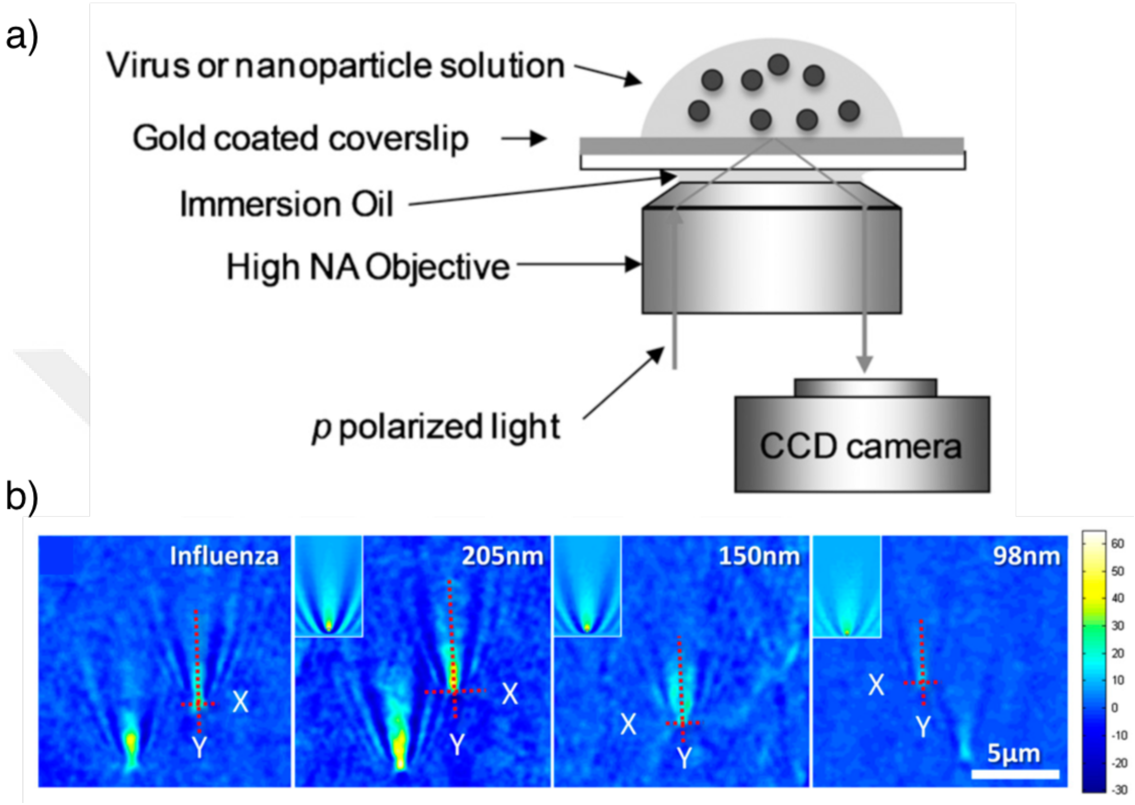

Figure 1.5: Surface plasmon resonance (SPR) biosensor for single particle detection. (a) Illustration of SPR biosensor setup. (b) SPR images of influenza and polystyrene nanoparticles with various sizes [33].

1.3.3 Whispering Gallery Mode Resonator Biosensors

Whispering Gallery Mode (WGM) resonators are dielectric microstructures the resonance frequency of which is defined by the optical path length that the wave travels inside the resonator [36]. Biomolecules accumulated on top of the resonator increases the optical path length, hence light transmission characteristics (transmission dips) changes [37] (Figure 1.6).

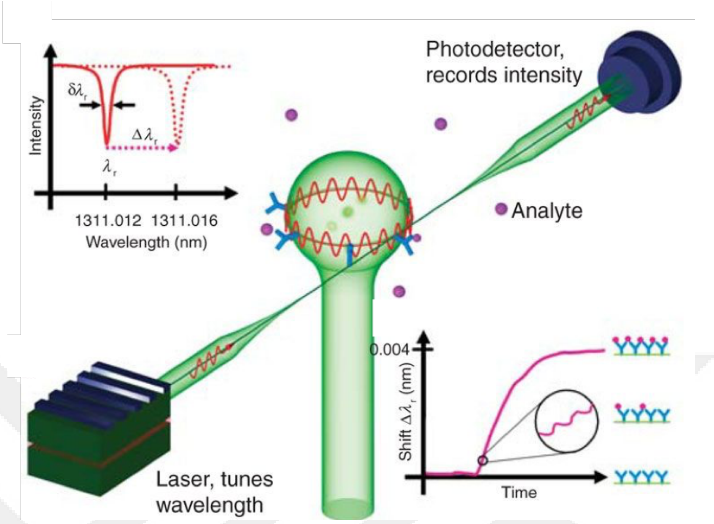

Figure 1.6: Whispering Gallery Mode (WGM) sensing working principle. Resonance frequency changes upon molecule binding. This shift can be monitored by a tunable laser source and detector pair. Shift is scaled with the adsorbed mass [37].

Using WGM Su et al. [38] detected single dielectric nanoparticles (5 nm diameter) in aqueous solution (Figure 1.7). This promising technique requires a complex process of fabrication hence, its adaptation to a high-throughput application is challenging. Also the signal is sensitive to binding location of nanoparticles.

1.3.4 Lensless Digital Holographic Microscopy

Lensless digital holographic microscopy (DHM) is based on capturing the holograms of the sample placed in the vicinity of a detector. As shown in Figure 1.8, the sample is illuminated from the top with a partially coherent light and inline holograms are captured. Captured holograms are further processed for reconstructing the image of the sample. This low cost imaging technique provides a large field of view (size of

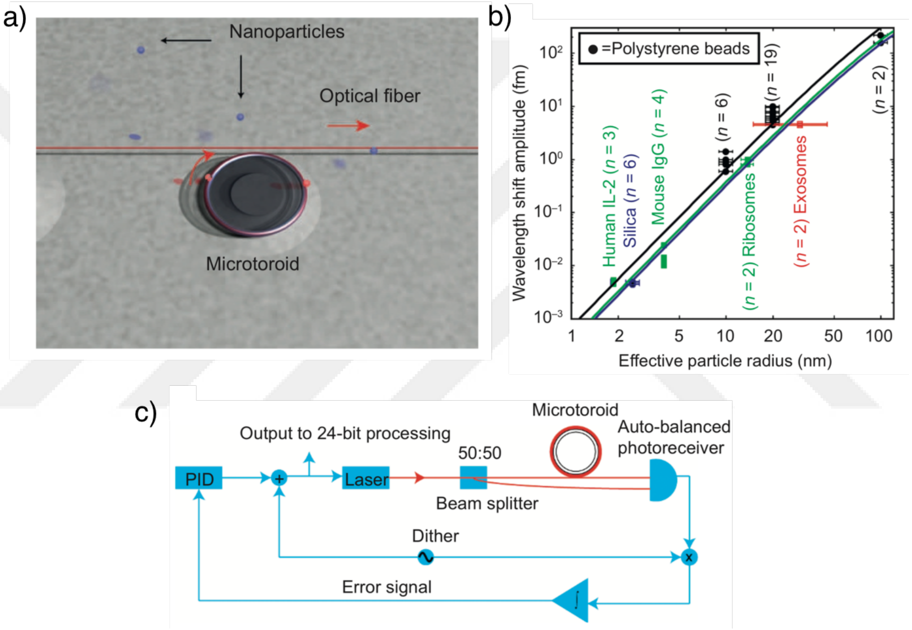

Figure 1.7: Illustration of microtoroid resonator used for single nanoparticle detection (b) experimental results for wavelength shift observed with respect to particle radius (c) block diagram of the readout system [38].

entire sensor chip) and has been successfully utilized in imaging of biological specimens such as bacteria, cells and tissue. However, translation of the capabilities of lensless DHM to single particle detection applications is challenging due to weak scattering cross-section of individual nanosized particles. One way to increase the contrast of single nanoparticles is the incorporation of self-assembled nanolenses by using wet-films [39]. Detection of single polystyrene particles with a diameter of 40 nm as well as individual H1N1 virus particles is demonstrated by creating nanolenses around each particle. In a recent work Daloglu et al. [40] further improved the sensitivity level of the technique by using ultraviolet (UV) light as the illumination source with the cost of complex illumination optics. Utilization of UV wavelength allowed the detection of 30 nm polystyrene nanoparticles without sizing capability.

1.3.5 Interferometric Microscopy

Interferometric techniques offer robust and easy-to-implement solutions for nanosized particle visualization. Although different acronyms are introduced such as iSCAT[41], SP-IRIS [42], COBRI[43] and stroboSCAT [44], the basic mechanism is the same: the interference of the reference light and the light scattered from the sample.

In any elastic scattering based method, total signal can be written as,

$$\begin{aligned} I_{total} &= |E_{background} + E_{scattered}|^2 \\ &= |\gamma . E_{illumination} + s . E_{illumination}|^2 \end{aligned} \tag{1.1}$$

Here, γ is the parameter that denotes the illumination field that reaches to the detector without interacting with the sample and s is the scattering coefficient of the particle.

The human eye is the traditional detector of microscopes. It has high dynamic range, however also has a nonlinear response to light intensity [45]. It is difficult to

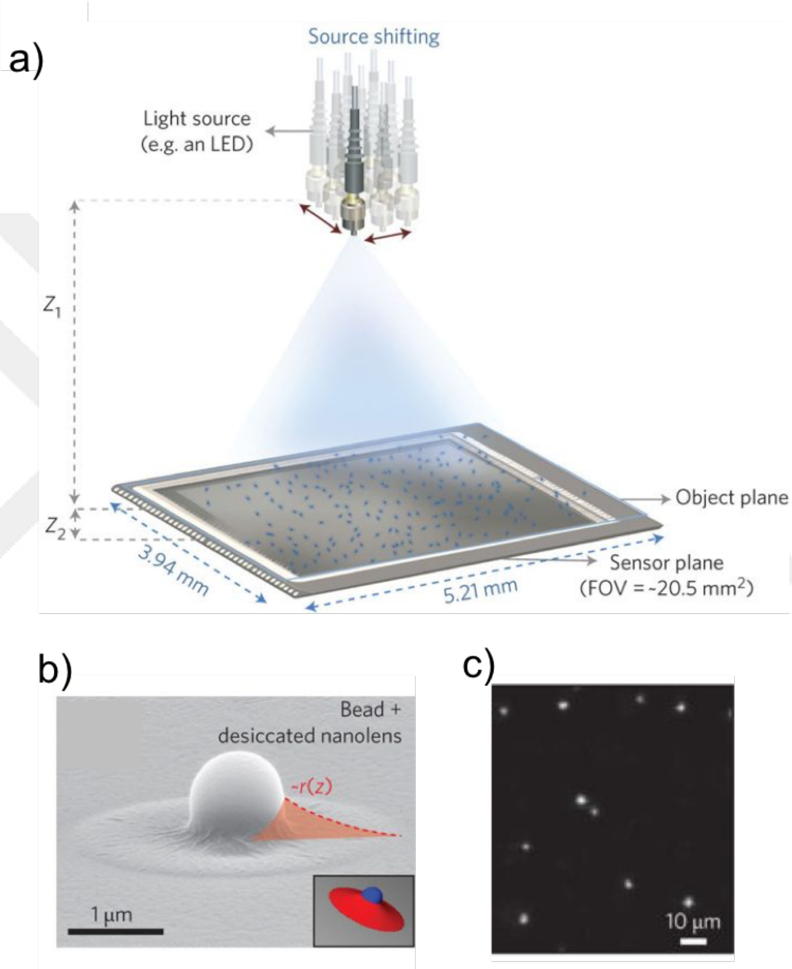

Figure 1.8: a)Lensless Digital Holographic Microscopy Setup. b) In order to visualize nanoparticles a self-assembled nanolenses are formed around the particle. c) Phase reconstruction of 100 nm polystyrene nanoparticles [39]

detect small intensity variations over a large background (seeing stars on a sunny day!). In 1902 Richard Adolf Zsigmondy and Henry Siedentopf introduced the dark-field microscopy, (at that time named as "*ultramicroscope*") which is based on the elimination of any background light ($\gamma \to 0$) to have high contrast [46]. They successfully demonstrated detection of gold nanoparticles. Equation 1.2 can be rewritten for dark-field microscopy as the expression given below,

$$I_{dark} = |E_{scattered}|^2 \sim \sigma = |s|^2 = 24\pi^3(\frac{n_m^4}{\lambda^4})(\frac{n_p^2 - n_m^2}{n_p^2 + 2n_m^2})V^2 \tag{1.2}$$

where σ is the scattering cross-section of the particle, n_p and n_m are the refractive index of the particle and the medium respectively, and λ is the wavelength of illumination. Since the total intensity is scaled with the square of the volume, the detection becomes challenging, especially for smaller particles. This scaling factor can be modified in interferometric microscopy by deliberately introducing a background field (γ=r($reflection\ mode$) or γ=t ($transmission\ mode$), where r and t denote the reflection and transmission coefficients of the surface where reference field coupled to the system, respectively.).

$$\begin{aligned} I_{interferometric} &= |r.E_{illumination} + s.E_{illumination}|^2 \\ &= [(|r|^2 + |s|^2 + 2|r||s|\cos(\phi)].|E_{illumination}|^2 \end{aligned} \tag{1.3}$$

The first term ($|r^2|$) has a constant value and can be characterized easily. Although the second term ($|s|^2$) becomes dominant in dark-field techniques, this term can be ignored for nanosized particles. If the coherence length of the illumination source is larger than the optical path difference between the scattered field and background field, a cross term comes into play. Normalized interferometric signal can be written as;

$$I_{normalized} \approx (\frac{2|s| \cos\phi}{|r|}) E_{illumination} \tag{1.4}$$

Please note that now the signal is scaled with $|s|$, i.e. the volume of the particle. The intensity also depends on the phase difference between scattered and background fields. Implementation of successful background removal methods in interferometric imaging enabled the detection of individual viruses [47], exosomes [48] and even single proteins [49]. A number of different interferometric microscopy configurations can be built depending on the illumination layout (widefield or confocal) or how the background (reference) field is coupled to the system (reflection or transmission and common path or double path). Here, we will review the details of two state-of the art interferometric microscope systems, namely iSCAT and SP-IRIS.

Interferometric Scattering Microscopy (iSCAT)

SCAT uses a standard cover glass as the sample substrate and the scattered light from the nanoparticles is interfered with a reference beam. The reference beam is reflected by the interface of a medium and the cover glass as shown in Figure 1.10. In order to have interference, a laser diode is used as a light source which introduces unintended interference signals (interference due to reflections from the lenses etc.). Due to the sensitivity of the interferometric measurements, impurities on the sample substrate also introduce artifacts on captured images. Noise due to the impurities on the sample substrate and light source is eliminated by subtracting the background from images then applying frame averaging [49] using high frame rate camera, with a trade-off in the field of view. iSCAT has been successfully utilized for detection of virus [50], formation of lipid layers[51] and visualization of single molecule binding [?]. Moreover, recently 3D motion of gold labeled epidermal growth factor receptor (EGFR) on live cell membrane has been tracked over 10 minutes, with nanoscopic resolution [41].

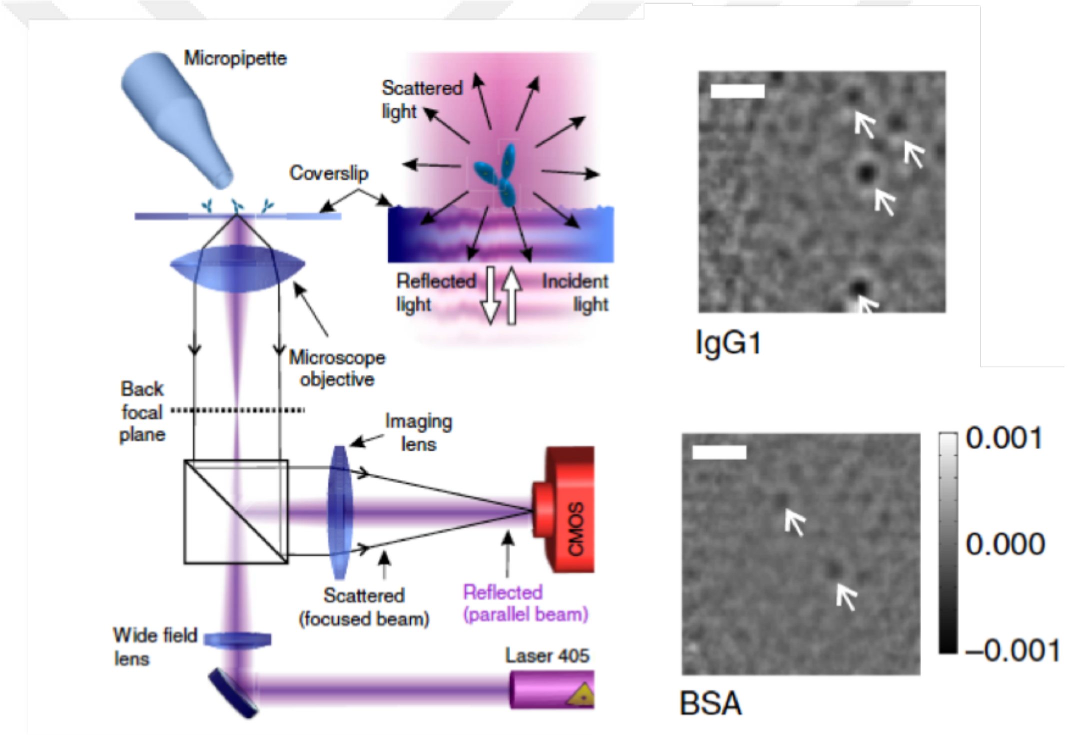

Figure 1.9: Interferometric Scattering Microscopy (iSCAT) setup. Biomolecules are immobilized on top of a standard coverslip and illuminated with a laser diode. Scattered field together with the reflected field from the back surface of the coverslip is collected and imaged on a CMOS camera with a high NA objective lens. Scalebar is 5 μm [49]

Single Particle Interferometric Reflectance Imaging Sensor (SP-IRIS)

SP-IRIS [42] implements a microfabricated sensor surface comprising thin film as a sample substrate, which provides a relatively uniform background. Utilization of this special substrate allows the light sources to be low coherent (LED). Integration of Fourier filters to selectively control the reference field enables the detection of 50 nm polystyrene particles [52] in the air.

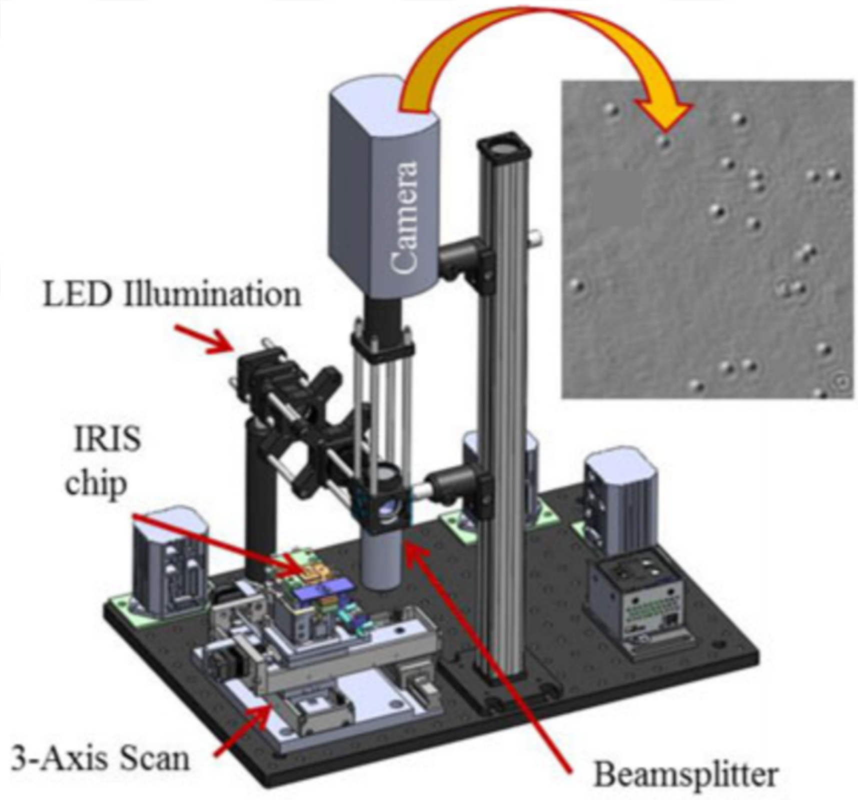

Figure 1.10: Single Particle Interferometric Reflectance Imaging Sensor (SP-IRIS) setup [53]

1.4 Contributions of the Thesis

The need for robust, high-throughput, sensitive and easy to use biosensors is ever increasing. Detection of single particles is the ultimate limit for biosensing. However single particle level quantification of biological nanoparticles such as viruses and exosomes is challenging due to their small size and low dielectric contrast. Fluorescence based methods are highly preferred, however they require labelling which may perturb the functionality of the particle of interest. On the other hand, wide-field interferometric microscopy allows the detection of sub-diffraction limited nanoparticles without using any labels. However wide-field interferometric microscopy has several limitations that need to be improved for its translation to clinical use. In this thesis we address the solutions to some of the limitations as explained below,

Contribution I: Development of a Probe Immobilization Calibration Tool for Microarray Experiments

In most of the biosensing experiments the sensor surface should be activated with probe molecules (i.e. antibodies) prior to the detection step in order to have selective capture of target molecules. Microarray technology, which is based on creating antibody spots on separate locations on the sensor surface, is commonly preferred in various applications thanks to its multiplexed nature and low sample volume requirement. Even though oligonucleotide microarray technology is proved to be highly effective in clinical applications, protein microarrays are not translated to clinical use due to high spot-to-spot and chip-to-chip variations. Therefore, sensitive and easy-to-use calibration tools for the quality control and calibration of arrays is required. We demonstrate the implementation of a label-free interferometric sensor by modifying a commercial flatbed scanner [54]. With this USB powered instrument, we have shown the detection of DNA hybridization in a microarray setup with comparable performance to a table-top IRIS system. Our instrument costs ∼100 USD and is capable of scanning a 4mm x 4mm area (scalable to a A4 paper size) in 30 seconds with ∼10 μm lateral resolution [55]. We expect that the developed system is going to draw interest as a label-free biosensing application in low-resource settings and a low-cost quality control device in microarray applications. Details of this work is given in Chapter 2.

Contribution II: Improvement of the Sensitivity Limit of Interferometric Microscopy by Implementing Depth Scanning Correlation Technique

Detection limit on size in interferometric detection methods is determined mainly by the signal-to-noise ratio (SNR) of the system. We utilize the defocusing response of dielectric nanoparticles to enhance the contrast of interference-based detection. We propose a method termed Depth Scanning Correlation (DSC) Interferometric Microscopy, where z-stack images of the immobilized nanoparticles on top of a sample substrate are captured and a correlation analysis is performed to enhance the visibility of the nanoparticles while diminishing the noise in the background. We show that DSC enhances the contrast of interference-based detection and improves both the signal-to-noise ratio (SNR) and the detection limit of size [56]. Details are given in Chapter 3.

Contribution III: Development of A Robust Quantification Method for Size Estimation in Depth Scanning Correlation Technique

Even though Depth Scanning Correlation (DSC) Interferometric Microscopy is proved to be highly sensitive for detecting nanosized particles, the capability for size determination is limited. Interferometric images are highly sensitive to the axial position of the sample. On the other hand, signal-to-noise ratio of the detected particles in DSC images is highly dependent on parameters of the analysis such as defocus range. In order to estimate the size of the detected particles, we utilize Bayesian inference. By using a forward model for the defocus response of nanoparticles, we fitted a Markov Chain Monte Carlo (MCMC) model to experimental data to determine the size of the particles. Details are given in Chapter 4.

Application Development for Interferometric Microscopy: In order to demonstrate the label-free detection capability of the developed platforms, exosomes isolated from tumor cells are visualized. Furthermore, neutrophil extracellular traps (NETs) are imaged in label-free format. Details are given in Chapter 5.

Chapter 2

HIGH-THROUGHPUT DETECTION OF BIOMOLECULES USING A MODIFIED FLATBED SCANNER BIOSENSOR

2.1 Motivation

Detection and quantification of biomolecular interactions such as DNA-DNA, antigen-antibody, or DNA-protein is important for biosensing applications as well as understanding the fundamental mechanisms in biology. Specifically, development of simple to-use, low-cost, portable and multiplexed biosensors are demanding. Commonly used methods such as ELISA and fluorescence microarrays require utilization of labels. However labeling often increases the complexity of the experiments and instruments hence it is time consuming and requires trained personnel. Another limitation of fluorescence microarrays stems from the need to characterize initial probe density. Especially for protein microarrays, probe immobilization density has huge chip-to-chip and spot-to-spot variation, which is the bottleneck for its translation to clinical settings [57]. Thus, characterization of initial probe density is critical for interpreting the final results correctly.

Alternatively, label-free methods are able to quantify biomolecular interactions by detecting a change in physical properties of the sample such as refractive index, mass, viscosity or conductivity [58]. Elimination of labels simplifies the assay preparation procedures and washing steps, which is essential for translating biosensing platforms to low resource settings.

Accordingly, the advancement in commercial electronics in the last decades allows us to reach powerful hardware components such as sensors, microprocessors or optical elements with relatively low cost. In this chapter we will introduce a label-free, high-throughput, low-cost biosensor, which is based on a modified commercial flatbed scanner. Details of the detection principle, namely Interferometric Reflectance Imaging Sensor (IRIS) will be given in Section 2.2.Hardware modifications on the flatbed scanner and sample preparation procedures will be explained in Section 2.3 and Section 2.4 respectively. In Section 2.5, performance of the developed biosensor is tested with DNA Hybridization and DNA Directed Antibody Immobilization experiments.

2.2 The Detection Principle - Interferometric Reflectance Imaging Sensor (IRIS)

The biodetection principle of the developed biosensing platform is based on Interferometric Reflectance Imaging Sensor (IRIS), a technique developed by Prof. M. Selim Ünlü's group at Boston University ([42, 59, 60]). This method relies on detection of the optical path difference in thin film layers using interferometry. As illustrated in Figure 2.1-a the sensor chip is made of a thermally grown SiO_2 layer on a Si substrate. When the sensor chip is illuminated, a part of the light is reflected from the top of the surface and part of the light is reflected from the buried interface. Depending on the thickness of the oxide layer, a wavelength dependent reflectance curve is observed (Figure 2.1b). Any biomass accumulated on top of the surface will increase the optical path difference, creating a shift in the reflectance curve. This shift can be quantified for layered substrates by the well-known Fresnel reflection formula given below;

$$R = \frac{r_{12}^2 + r_{23}^2 + 2r_{12}.r_{23}.\cos(2\phi)}{1 + r_{12}^2 + r_{23}^2 + 2r_{12}.r_{23}.\cos(2\phi)} \tag{2.1}$$

where r_{12} and r_{23} are the Fresnel reflection coefficients ($r_{ij} = (n_i - n_j)/(n_i + n_j)$) for air SiO_2 and $SiO_2 - Si$ interfaces, and ϕ is the optical path difference defined as;

$$\phi = \frac{2\pi t}{\lambda} n_2 \cos\theta \tag{2.2}$$

where t is the total thickness of the oxide layer, λ is the wavelength of illumination and θ is the angle of incident light.

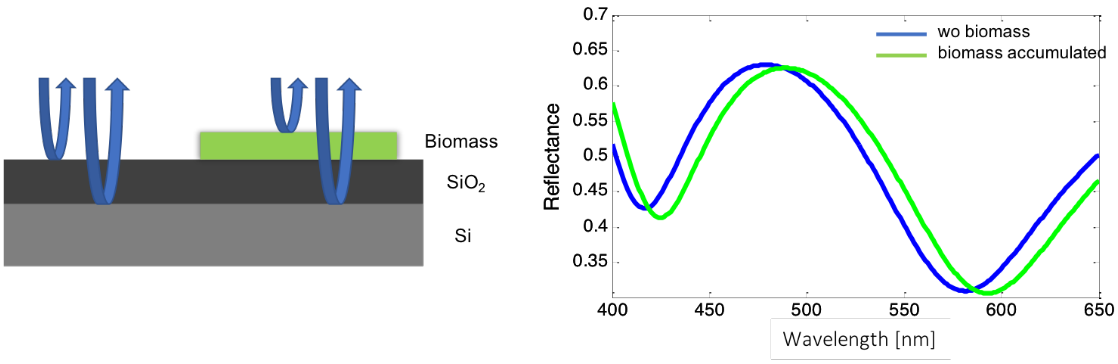

Figure 2.1: Interferometric Reflectance Imaging Sensor (a) Layered sample substrate utilized for biosensing. (b) Wavelength dependent reflectance curve for the layered substrate. Any biomass accumulated on top of sensor chip creates a wavelength dependent ship on reflection curve.

The reflectance spectrum can be sampled by sequential illumination with single-color LEDs and imaged onto a commercial CCD camera. Film thickness can be calculated by solving the Equation 2.1 and 2.2 for each pixel.

Accumulated biomass on top of an oxide region increases the optical path difference. The increase in the OPD can be assessed under several approximations:

i)Fixed height approximation: Refractive index of the layer changes depending on the concentration of adsorbed materials [61]

. ii)Fixed index approximation: Adsorbed mass causes the thickness to increase while the refractive index of the biomaterials stays identical to the thin film [62].

To simplify the calculations we apply the fixed index approximation. In an earlier work, Ozkumur et al.[63], carefully generated a relation between the increase in the thickness and adsorbed biomass. Once the increase in the thickness due to adsorbed biomass is determined, total biomass can be calculated using these conversion factors.

2.3 Flatbed Scanner based IRIS

Benchtop setup of IRIS is shown in Figure 2.2. Optical setup includes LEDs, illumination and collection optics with an objective lens and a CMOS camera.

For adaptation of the capabilities of the IRIS system to field use, it is important to lower the cost, make it more portable, easy-to-use, robust and reliable system. Flatbed scanners have great potential for such an adaptation as they have the necessary hardware for IRIS operation and moderately powerful imaging capabilities. For the adaptation of the capabilities of the IRIS system to field use, it is important to lower the cost, make it more portable, easy-to-use, robust and reliable. Flatbed scanners have great potential for such an adaptation as they have the necessary hardware for IRIS operation and moderately powerful imaging capabilities. In recent decades,

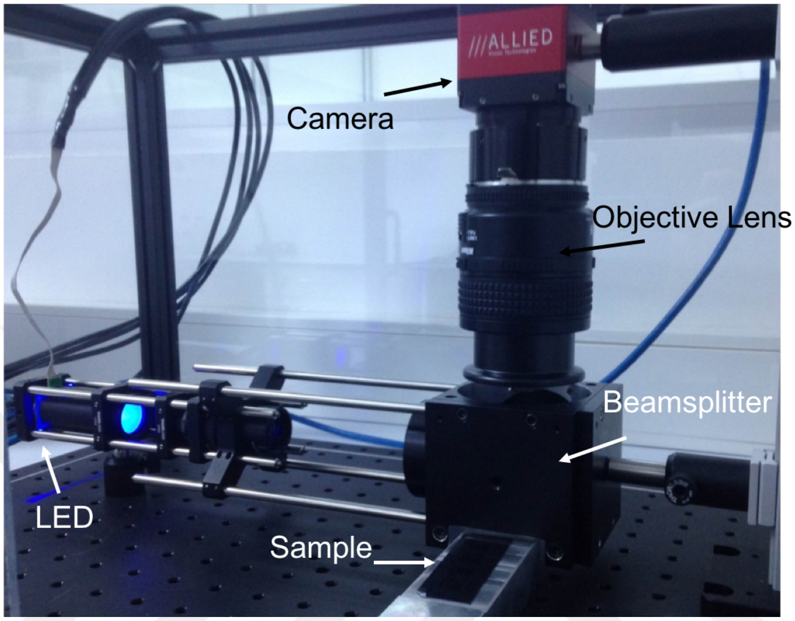

Figure 2.2: Benchtop Interferometric Reflectance Imaging Sensor Setup.

mobile, low cost, and high-performance consumer electronics devices became available to public. Various commercial electronic devices such as mobile phones [64, 65, 66] or wearable devices [67] are utilized in scientific imaging and detection applications [68]. Specifically, flatbed document scanners [69] capable to scan A4 size documents with high resolution, includes optical and electronic components that can be used for biosensing applications.

Depending on the imaging structure, commercial document scanners can be divided into two categories namely (i) CCD based and (ii) Contact Image Sensor (CIS) Scanners. CCD based scanners have fluorescence light bulbs or white LEDs as illumination source and through demagnification optics, the reflected light from the documents are imaged onto a 2D CCD sensor array with color filters. Even though the scanning performance is superior in terms of depth of field, this type of scanners are expensive, requires a large amount of power and bulky. On the other hand, CIS scanners have a more compact imaging system. During scanning, a scanning head (Figure 2.3-b) moves through the document and captures the images line by line. The scanning head consists of LEDs, a light guide, a GRIN lens array, a monochromatic detector array and a scanner glass holder (Figure 2.3b-c). Red, green and blue LEDs sequentially illuminate the document surface. Reflected light is collected by the GRIN lens array and imaged to the detector array. These types of scanners are relatively inexpensive, portable and can be powered through a USB cable.

In this work a CIS type flatbed scanner (Canon LIDE 210, Figure 2.3-a) is selected as the base hardware platform for our biosensor because it is low cost (100 USD), provides illumination at different wavelengths and the modification for its adaptation as an IRIS is feasible. Illustration of the scanning head is shown in Figure 2.4-a in the document scanning setting. Because the reflection type for a document is diffuse reflection, scattered light can be collected by GRIN lens array and successfully imaged to the CMOS sensor array. However, if the paper is replaced by a sensor chip, reflected light will not reach to the detector, because specular reflection becomes dominant. Hence, we made a number of modifications to the flatbed scanner.

2.3.1 Scanner Modifications

In order to capture the most of the reflected light and create an image of the sensor chip, several modifications on the flatbed scanner is required. In contrast to CCD based scanners, depth of field in CIS scanners is quite low (on the order of a few hundred μm).

The scanner glass provides the fixed distance between the document and the lens

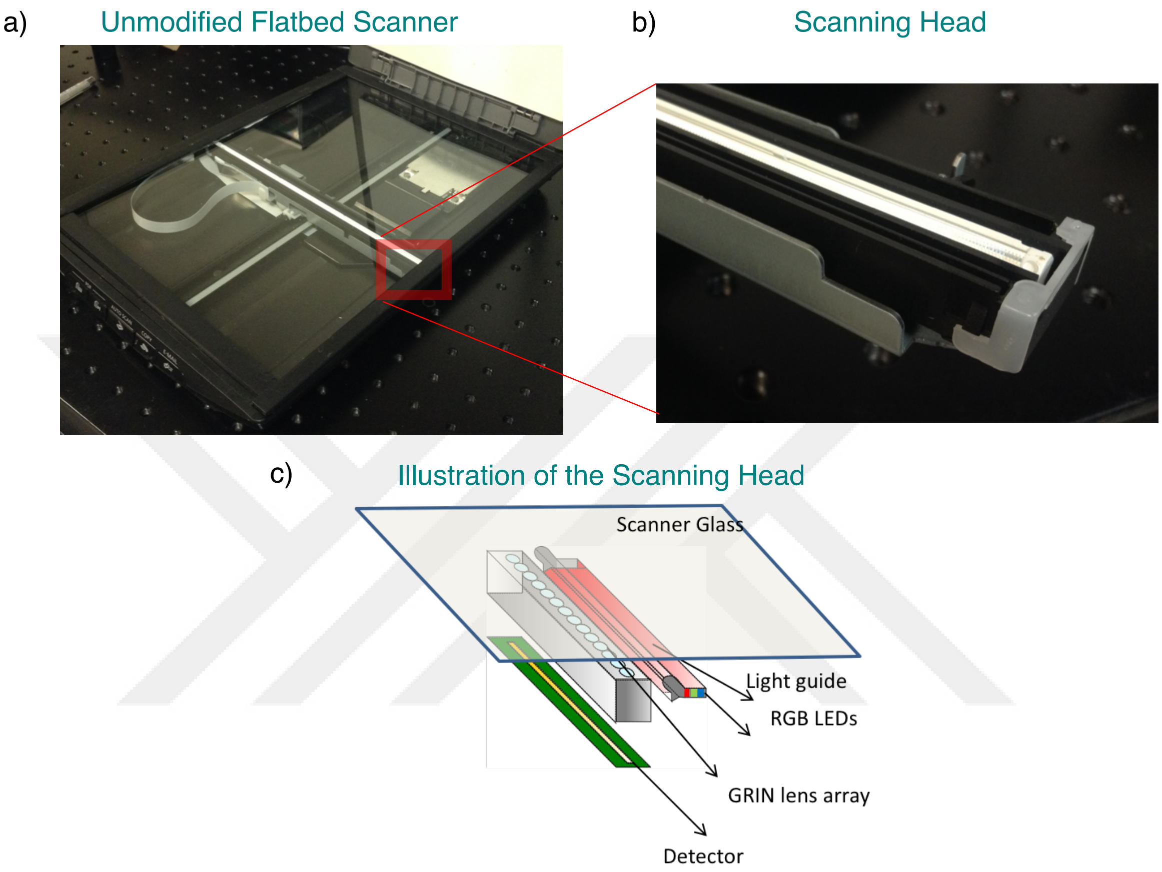

Figure 2.3: Flatbed Scanner and the Scanning Head (a)Unmodified Flatbed Scanner (b) Scanning head (c) Illustration of the scanning head. Scanning head is composed of RGB LEDs, light guide, GRIN lens array and a line detector.

array. Any object above the document plane is not imaged properly by the imaging optics. Therefore tilting the sample to direct the reflected light to the lens array is not a viable solution. We decided to tilt the scanning head to collect the specularly reflected light (Figure 2.5-a). In order to tilt the head, we inserted a 3D printed wedge beneath it as shown in Figure 2.5-d. We also replaced the existing plate holders with

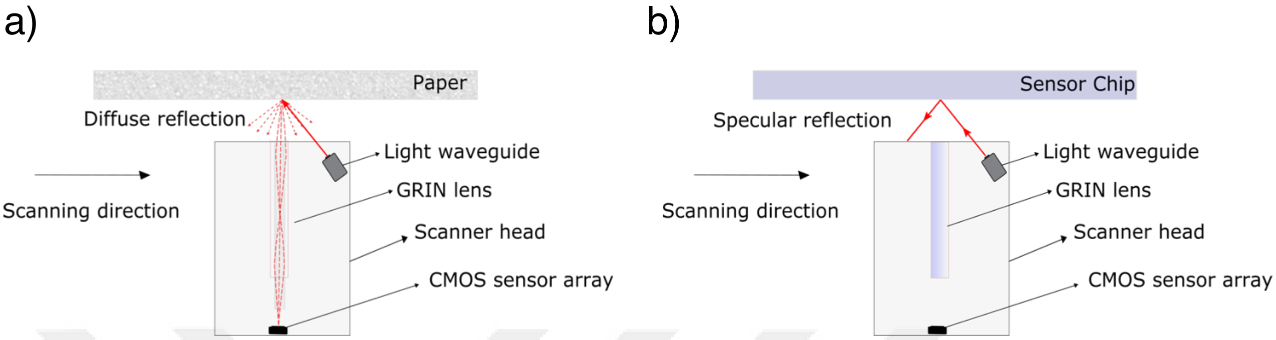

Figure 2.4: Diffuse vs Specular Reflection in Flatbed Scanners

3D printed ones to keep the angle fixed during the scan Figure 2.5-b. Furthermore we replaced the scanner glass with a CNC fabricated custom sample holder which contains wells to place sensor chips. In Figure 2.5-c and d the final setup with the rotated scanner head and custom sample holder is shown.

2.3.2 Data Acquisition and Processing

Instead of the commercially available software which provide only restricted access to the sensor array and LEDs, we used Scanner Access Easy Now (SANE), an open source application programming interface (API) to control Genesys Logic GL124 which is the main controller of the scanner. This allowed us to determine the gain of the sensors, illumination LEDs to use and the region to scan.

Resolution and bit depth is set to 4800 dpi and 16-bit respectively, in all measurements. For each measurement 10 consecutive scans (frames) are averaged. Interferometric images of the sensor chip in color mode (under illumination with Red, Green and Blue LEDs sequentially) are captured. In this work, instead of solving Fresnel equations for each pixel individually to determine the corresponding thick-

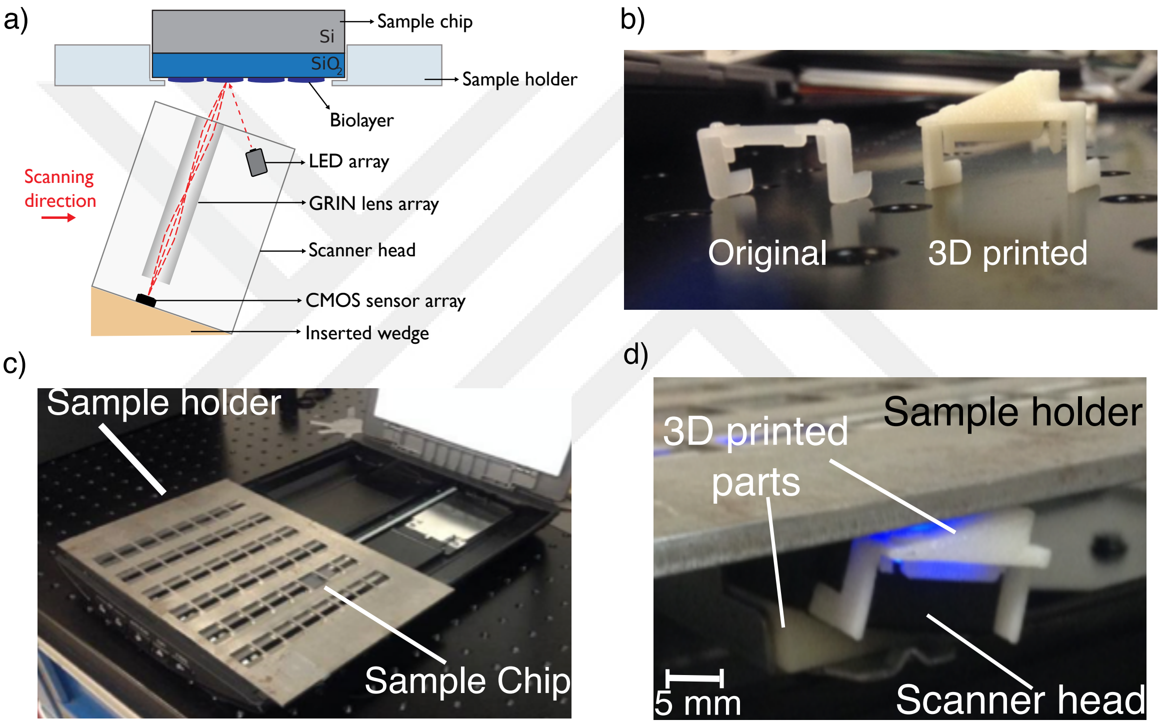

Figure 2.5: Mechanical Modifications on Flatbed Scanner (a) Illustration of tilted scanning head. (b) Glass panel holders are replaced with 3D printed holders to tilt the scanner head (c)Flatbed scanner after mechanical modifications (d) sideview of scanning head and the sample holder.

ness, a lookup table (LUT) approach, explained in [70] is implemented. In summary, as shown in Figure 2.6, the image of the reference region (SiO_2) is captured and normalized reflectance values are calculated by averaging over the region. The corresponding film thickness of the reference region is calculated by minimizing the cost function given below,

$$\chi^2 = \sum_{x=1}^{3} |I_x(d) - \int_{\lambda_{min}}^{\lambda_{max}} R(\lambda, d) S_x(\lambda) d\lambda|^2 \tag{2.3}$$

where I_x is the measured normalized intensity value for each channel (i.e. x=1 is red, 2 is green and 3 is blue), $R(\lambda, d)$ is the reflectivity of the layered substrate which can be computed from Equation 2.1 and $S_x(\lambda)$ is the spectrum of the LEDs which is measured beforehand. Firstly, by minimizing the cost function, a reflectance curve is fitted to the measured reflectance values to find the correct film thickness (SiO_2) for the reference region (Figure 2.6-b). Then using these parameters and Equation 2.1 , we create a look-up table as shown in Figure 2.6-c which show the thickness of the film associated with the expected reflectance value. Once this LUT is generated, a thickness value can be assigned to each pixel according to measured intensity.

Raw image of the sensor chip captured by the modified scanner is shown in Figure 2.7. Note that white bright spots are the alignment marks (etched Si regions). Although the microarray spots are visible in raw images, quantification is difficult due to scanning artifacts. The artifacts that are perpendicular to the scan direction are associated to the GRIN lens array. These artifacts can be removed by dividing the raw image to a reference image which is a scan of an empty sensor chip. Alternatively, the reference image can be generated directly from the raw image by upsampling a line cut of SiO_2 region, since the fringes are repeated in the scanning direction. Following

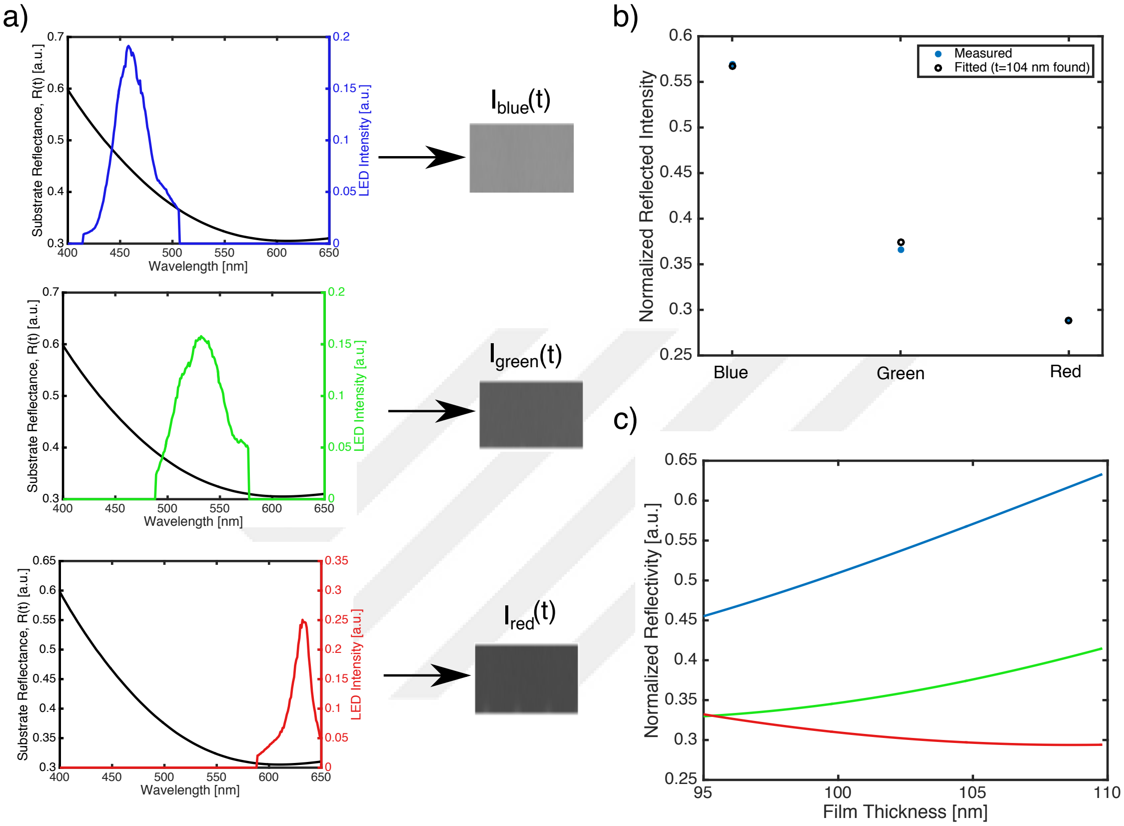

Figure 2.6: Look-up Table Generation for Scanner Biosensor (a) Spectrum of each LED and the reflectivity of the layered substrate (b) Measured and the fitted reflected intensity (c) calculated look-up-table

the detection and removal of alignment marks (bright spots), film thickness value is calculated for each pixel using the lookup table. Microarray spots are detected using a custom script written in MATLAB. The height of each spot is calculated by subtracting the average thickness of annuli surrounding the spot (area between the blue circles in Figure 2.7) from the average thickness of the spot's central area which is calculated by averaging all the pixels inside the central region (green circle).

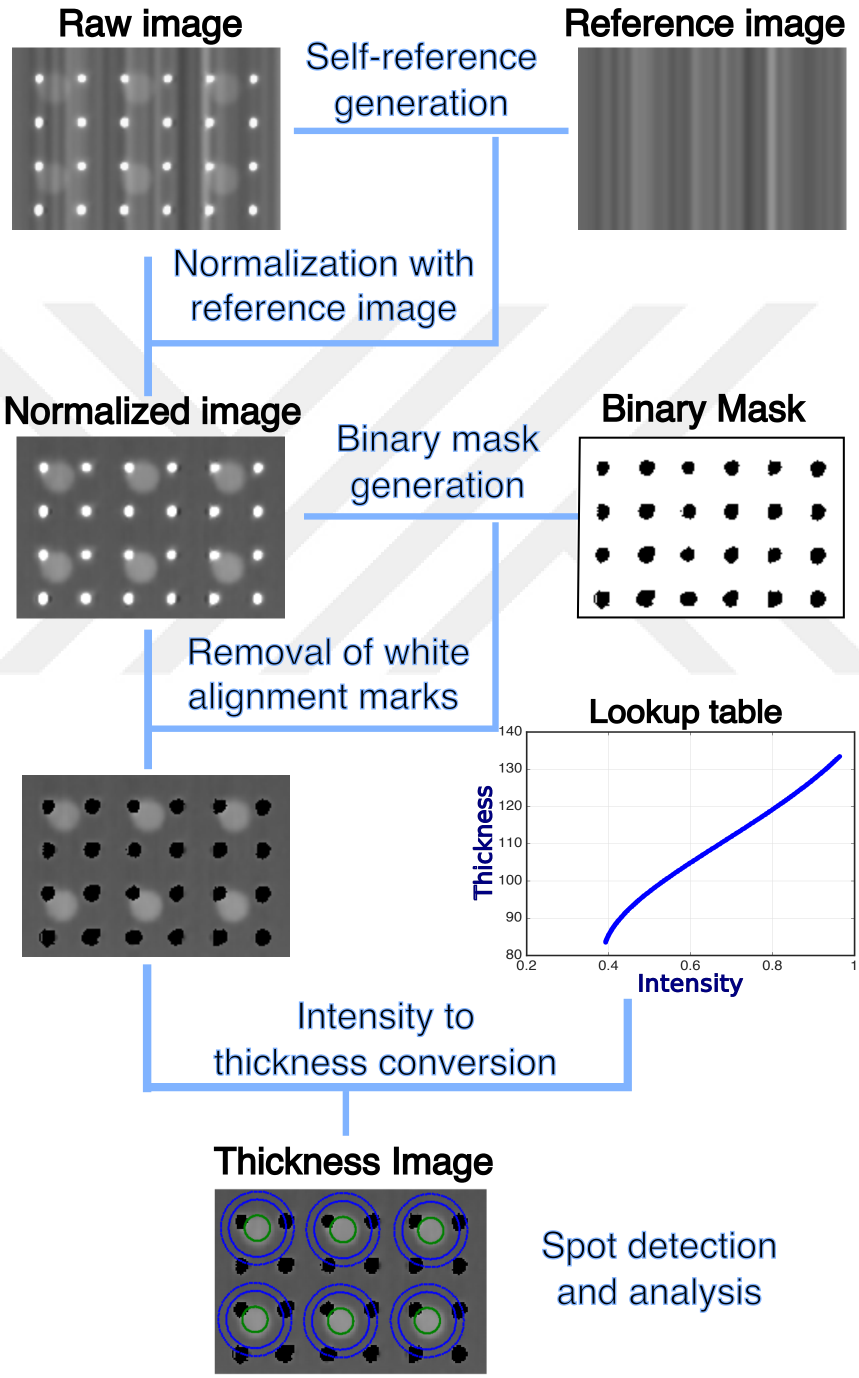

Figure 2.7: Data Analysis Pipeline for Flatbed Scanner Biosensor.

2.4 Sample Preparation

Si/SiO_2 substrates with 100 nm oxide thickness is purchased from Silicon Valley Microelectronics (SVM) and cut into 1 cm x 1 cm squares. Upon applying a standard wash (sonication in acetone, rinsed in methanol and DI water), chips are dried with nitrogen. Chip surface is functionalized by coating the surface with copoly (DMA-NAS-MAPS). For the coating process clean chips are pretreated with 1 M NaOH for 30 min, and rinsed with DI water. The chips are then immersed in a a polymeric solution (DMA-NAS-MAPS at 1 w/v concentration) (Lucidant Polymers) for 30 min. Following the wash in DI water, chips are dried under nitrogen gas, and baked for 15 min in the oven at 80 °C. Polymer coated chips are stored in the desiccator, until DNA spotting.

DNA microarrays are prepared using a microarray spotter (sciFLEXARRAYER S3,Scienion). The spotted chips kept in a humid chamber (67% humidity) overnight and washed with 50 mM ethanolamine in 1 Tris-buffered saline (150 mM NaCl and 50 mM Tris-Hcl, Fisher Scientific), pH = 8.5, for 30 min. Finally they are washed with PBST (PBS with 0.1 % Tween) for 30 min, rinsed with PBS, and dried with nitrogen.

2.5 Experimental Results

2.5.1 Benchmarking with Benchtop IRIS

In order to test the performance of Flatbed Scanner Biosensor, a DNA microarray chip with varying biomass concentration is prepared (5 replicated spots with 7 different concentrations). Same chip is imaged both with benchtop IRIS and our modified flatbed scanner. In Figure 2.7 visualization of microarray spots captured both of the setups is given. As expected microarray spots with higher concentrations have higher contrast in captured images. Following the determination of the thickness value of each pixel by using the look-up table, height of each spot is calculated by subtracting the average thickness of the background region from the average thickness of the central part. Calculated heights (increase in OPD due to biomass) are in good agreement for both of the methods (Figure 2.7b). Errorbars represents the variation between the replicated spots.

In order to quantify noise floor of our measurement system, same chip is measured 6 times with 10 frames averaged in a 1 hour period. The standard deviation of height of the same spot is calculated as 0.04 nm. This noise floor corresponds to biomass of 33 pg/mm^2 for DNA and 50 pg/mm^2 for protein microarrays, by using the conversion factors between the OPD and the biomass determined in earlier works on Interferometric Reflectance Imaging Sensor ([63]).

2.5.2 DNA Hybridization Experiments

In order to demonstrate that developed system is capable to detect biomass change, we designed DNA hybridization experiments. Related DNA sequences used in the experiments is given in Table 2.1. Here the target A' is complementary to surface probe A.

Surface probe A is immobilized to functionalized sensor surface at varying concentrations 0 to $50\mu M$ while keeping the total spotting concentration is constant ($50\mu M$). In order to achieve this, A is mixed with an unrelated sequence C at different ratios ($0\%, 10\%, 20\%, 40\%, 60\%, 80\%$ and 100%). As seen from the prior incubation scans (Figure 2.9), spot morphology is uniform across the sample. Total microarray con-

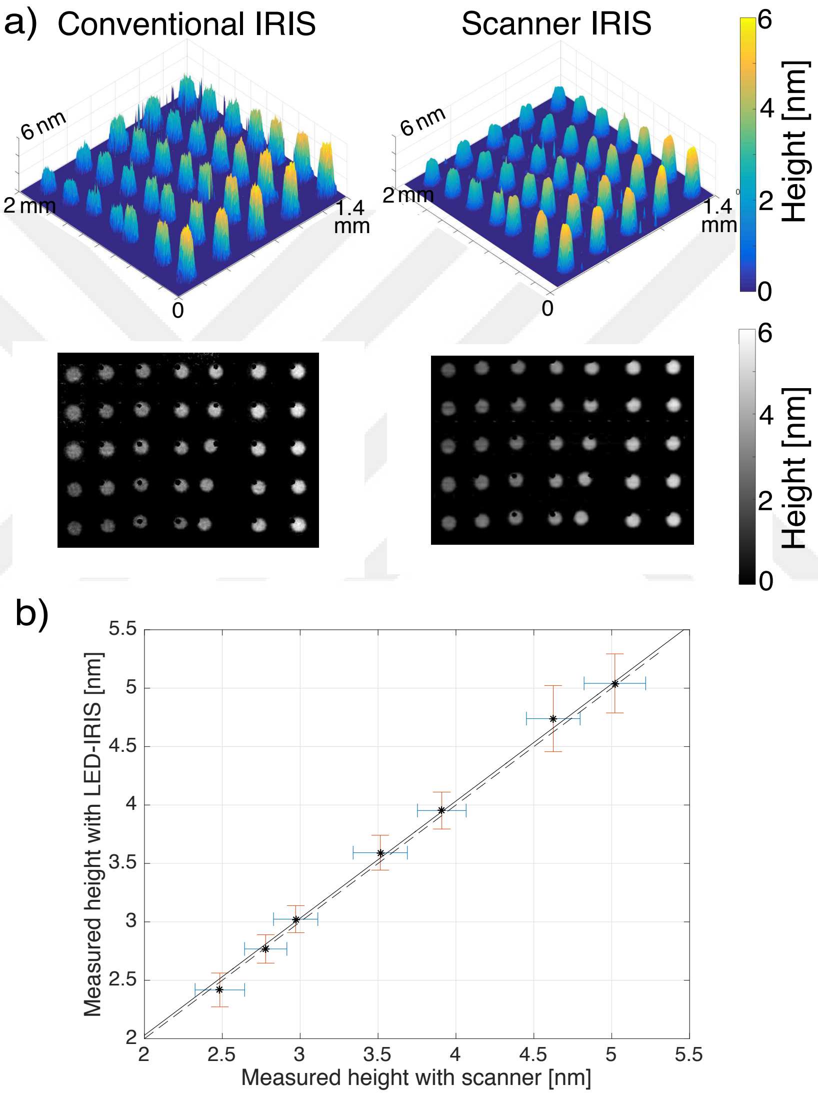

Figure 2.8: Benchmark of Scanner IRIS with Tabletop IRIS

Table 2.1: Surface Probes and Corresponding Target Sequences

Name	Sequence	Antibody
A	$5'$*ATC TGA ACC CAC CGC TAT TCC ATG CAC TTG ATT CCG AGG C* $3'$	-
A'	$5'$*GCC TCG GAA TCA AGT GCA TGG AAT AGC GGT GGG TTC AGA T* $3'$	-
B	$5'$*ATC CGA CCT TGA CAT CTC TAC CAC TGC GAC TAA CTC TGT A* $3'$	-
$B' - 13F6$	$5'$*AAAAA TAC AGA GTT AGT CGC AGT GG* $3'$	$13F6$
C	$5'$*ACT TAG GAC TCA GTA CAG GAT AGA CTT CAG CGT GGT TGG A* $3'$	-

tains 7 replicated spots for each mixing ratio. Upon probe immobilization chips are stored in a humid chamber overnight and washing protocols are applied as explained in previous section.

Prior to hybridization, samples were scanned with the modified flatbed scanner, to quantify probe immobilization density (Figure 2.9-a). Then samples are incubated with target oligonucleotide A' at a concentration of 1 μM (in PBS). Hybridization is done at room temperature for 1 hour. Upon incubation samples were washed 3 times in 2xSSC for 3 min, once in 0.2x SSC for 3 min and once in 0.1x SSC for 10 sec to remove DNA strands that are not hybridized.

Figure 2.9-b shows the post incubation images of the sample acquired with modified flatbed scanner. As expected the contrast of individual spots with rich sequence A content is higher.

2.5.3 DNA Directed Antibody Immobilization Experiments

The high spot-to-spot and chip-to-chip variation in protein microarrays in comparison to DNA microarrays is a bottleneck in their clinical use [71, 72]. For better spot morphologies and increased reproducibility of protein microarrays, immobiliza-

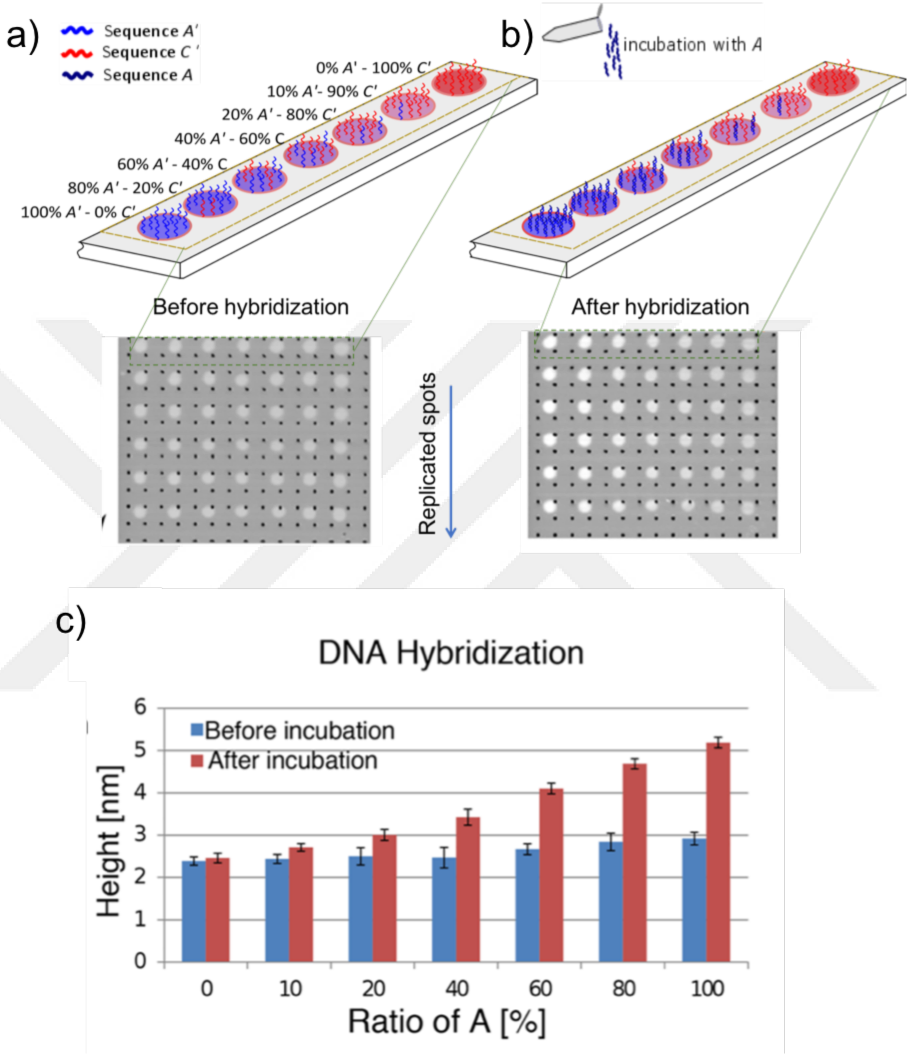

Figure 2.9: DNA Hybridization Experiment

tion through oligonucleotides has been suggested [73]. This technique, DNA-directed antibody immobilization (DDI), has been shown to elevate the antibodies from the surface and improve their capture efficiencies [74]. To show the suitability of the scanner as a quality control instrument for antibody microarrays, we conducted a DNA-directed antibody immobilization experiment (Figure 2.10). DNA probes of two different sequences (B and C) mixed in varying ratios are spotted on the functionalized sensor surface, and the array is incubated with the B'-13F6 conjugate. Preincubation and postincubation images are shown in Figure 2.10 , where the quality of each individual spot can be inspected. The measured spot heights and spot-to-spot variations are indicated in Figure 2.10-c. As expected, since the size of the antibodies is larger in comparison to the size of the oligonucleotides, the antibody-conjugated DNA hybridization is detectable at a lower mixing ratio (10%) than DNA hybridization. For the same reason, saturation of the spots is also observed for high mixing ratios ($> 80\%$).

2.6 Conclusions

Low-cost, portable, and easy-to-use label-free biosensors are gaining importance for their potential use in low resource settings and point-of-care applications. In this chapter, we demonstrate the utilization of a commercial flatbed document scanner as a label-free interferometric biosensor for high-throughput imaging of DNA and protein microarrays. We use a Si/SiO_2 layered substrate, and implement hardware and software modifications on the scanner. The interference-based sensing relies on the changes in the optical path difference between the interfaces upon biomass accumulation on the top surface. The added biomass results in a quantifiable shift in spectral reflectivity, which is sampled at different wavelengths to determine its thickness.

We provide a comparison of the system against a well-established label-free interferometric sensor (IRIS), and report a noise floor of 40 pm, which corresponds biomass

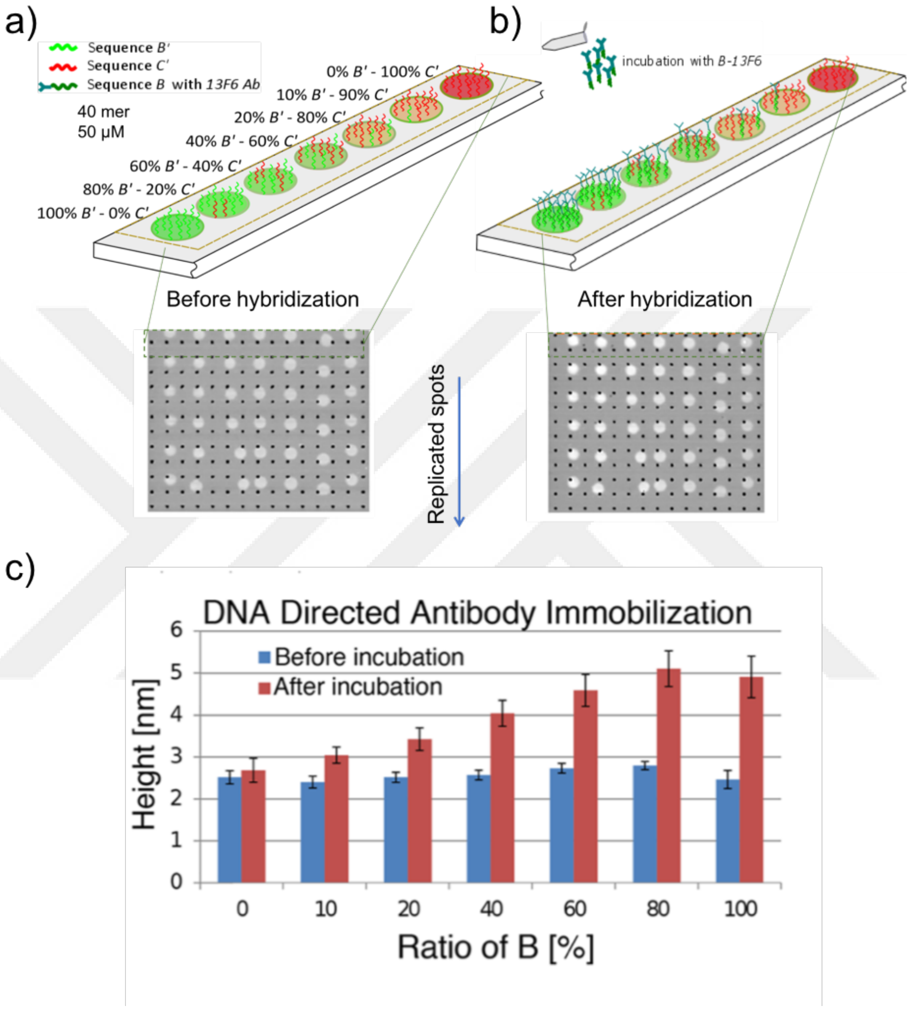

Figure 2.10: DNA Directed Antibody Immobilization Experiment

of 50 pg/mm^2 and 33 pg/mm^2 for protein and DNA microarrays, respectively. With a cost as low as 100 USD, this platform can be used in label-free diagnostics applications, especially in low-resource settings. More importantly, it can easily be integrated into the existing protocols of fluorescence based detection assays to address variations across and between arrays by providing true quantitative quality control, as well as possible calibration of arrays of molecular probes (DNA or protein).

Chapter 3

SINGLE PARTICLE DETECTION USING DEPTH SCANNING CORRELATION (DSC) INTERFEROMETRIC MICROSCOPY

3.1 Single Nanoparticle Detection using Wide-field Interferometric Microscopy

Direct detection of biological nanoparticles is challenging due to their small size and low dielectric contrast. Scattering of spherical particles can be modeled with Mie theory, which reduces to Rayleigh theory for nanoparticles [75]. According to this theory scattering cross-section (σ) is scaled with the square of the polarizability of the particle (α), which is a function of particle volume (V). Hence the scattering strength is scaled with the sixth power of the particle radius (r) as given in the following equations,

$$\sigma = \frac{8}{3}\pi^3\alpha^2\frac{n_m^4}{\lambda^4} \tag{3.1}$$

where polarizability is written as,

$$\alpha = 3V\frac{n_s^2 - n_m^2}{n_s^2 + 2n_m^2} \tag{3.2}$$

This scaling factor causes the scattering intensity to go below the noise limit of the measurement systems for nanoparticles and makes digital quantification difficult.

However, interferometric detection can be implemented by combining the scattered field with a reference field. In interferometric methods, detected signal can be written as,

$$I_{det} = |E_{ref} + E_{sca}|^2 = s^2 E_{inc} + r^2 E_{inc} + 2.r.s. \cos{(\phi_s - \phi_r)} E_{inc} \tag{3.3}$$

where E_{inc} is the illumination field, r is the reflection coefficient of the sample substrate, s ($\sim V$) is the scattering coefficient of the particle and $(\phi_r - \phi_s)$ is the phase difference between the two fields. Note that in contrast to purely scattering based techniques, where particle signal is scaled with the square of the volume, the interference term in interferometric techniques (Equation 4.7) is scaled with s and thereby with the volume of the particle.

$$I_n = \frac{|E_{ref} + E_{sca}|^2}{|E_{ref}|^2} \approx \frac{2|E_{sca}| \cos{(\phi_r - \phi_s)}}{|E_{ref}|} \tag{3.4}$$

Ignoring the DC term and assuming that $|E_{sca}|^2$ iis very small and can be ignored for nanoparticles, the total signal or the contrast of the nanoparticle image is mainly dominated by: (i) the amplitude of the scattered field $|E_{sca}|$ (envelope term) and (ii) the phase difference between the reference and scattered fields, $\cos(\phi_r - \phi_s)$

3.2 Defocus Response as a Contrast Mechanism

Interferometric signal is highly sensitive to the phase difference between the scattering and the reference field. A typical defocus response for a polystyrene particle is shown in Figure 3.1 as the blue curve. This behavior can be modelled as a sinusoid (due to phase difference, $cos(\phi_s - \phi_r)$ term in Equation 3.4) multiplied by a Gaussian envelope (due to amplitude of scattering signal, $|E_s|$ term in Equation 3.4). Conventionally, the focal plane is determined as the plane in which the particle exhibits the maximum contrast. Once the nominal focal plane is defined, interferometric image is captured for further analyses such as the determination of number of particles, size distribution etc. Yet simpler, this approach has a few shortcomings: (i) It requires a constant feedback mechanism to keep the sample in focus; (ii) Particles can be localized on different axial positions. Furthermore, due to the size scaling factor ($|E_s|$), attainable contrast for small particles is low and this contrast signal can be easily overwhelmed by the background noise. On the other hand, it is apparent from the defocus plot

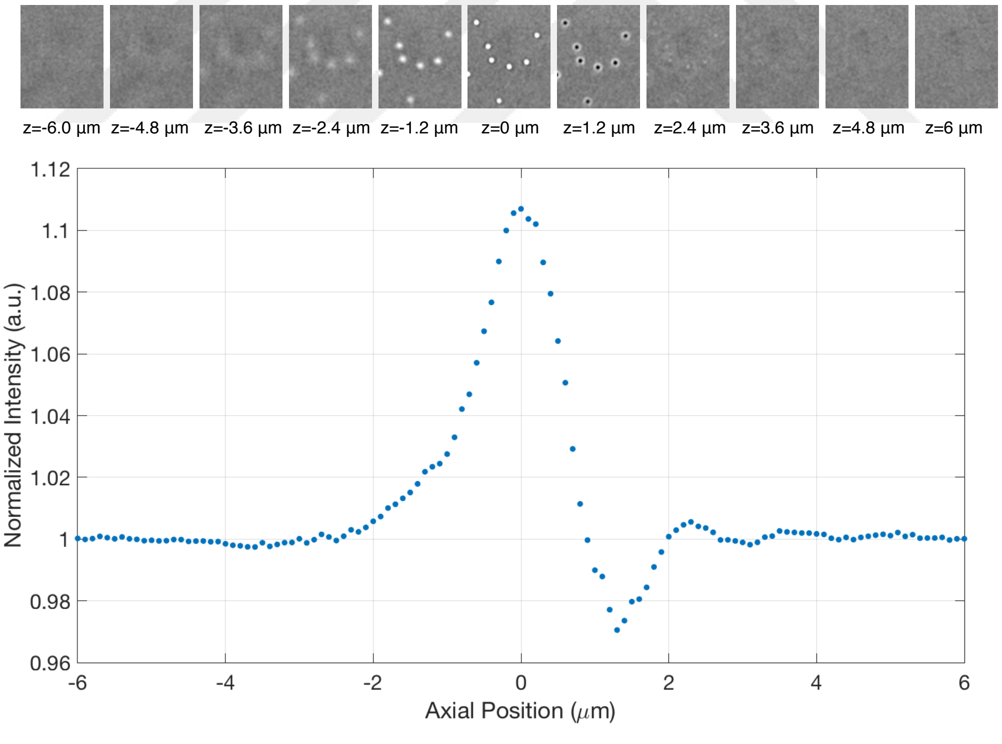

Figure 3.1: Defocus Response for 100 nm Polystrene Nanoparticle in Wide-field Interferometric Microscopy.

that not only the nominal focus point (peak value), but also defocused images carry information about the presence of the particle. Furthermore, the defocusing response of the background and the particle has distinct features that can be used to selectively amplify the particle signal while suppressing the background noise. Instead of analyzing only one point (peak point), the overall behaviour can be used to enhance the visibility of particles.

One way to improve the contrast of nanoparticle images in interferometric microscopy is to calculate difference images [53] by calculating the difference between the maximum (constructive interference) and the minimum (destructive interference) intensity value of each pixel in defocused images.

3.3 Depth Scanning Correlation Image Generation

3.3.1 Optical Setup

Our imaging platform is a custom built wide-field interferometric microscope based on a special platform named as Single Particle Interferometric Reflectance Imaging Sensor (SP-IRIS). Figure 3.2 shows a simple layout of our platform. As a sample substrate we used a layered Si/SiO_2 chip, that provides a flat background which is important for decreasing the background noise. Patterned and thermally grown oxide wafers are purchased from Silicon Valley Microelectronics, and cut into squares of 1 cm width.

As the light source a green LED (M530L3, Thorlabs Inc.) is used. Note that in our configuration the distance between the nanoparticle and the surface from which the reference field is reflected is around 200 nm. This allows us to use low coherent light sources such as LEDs. Utilization of a low coherent source as opposed to lasers is beneficial to decrease the noise associated with speckles and interference fringes due to multiple reflections in the optical path.

In order to have wide-field illumination, the LED is focused to the back focal plane of a microscope objective (Plan Fluor 0.8 NA, 40x, Nikon Instruments). The same objective is used for collecting the reflected and scattered fields from the sample substrate and nanoparticles, respectively, and focusing these fields to a CMOS Camera (Point Gray 3.0). Sample position is controlled by a high precision piezoelectric stage with vacuum chuck. Images with a field of view of 300 μm x 200 μm are captured.

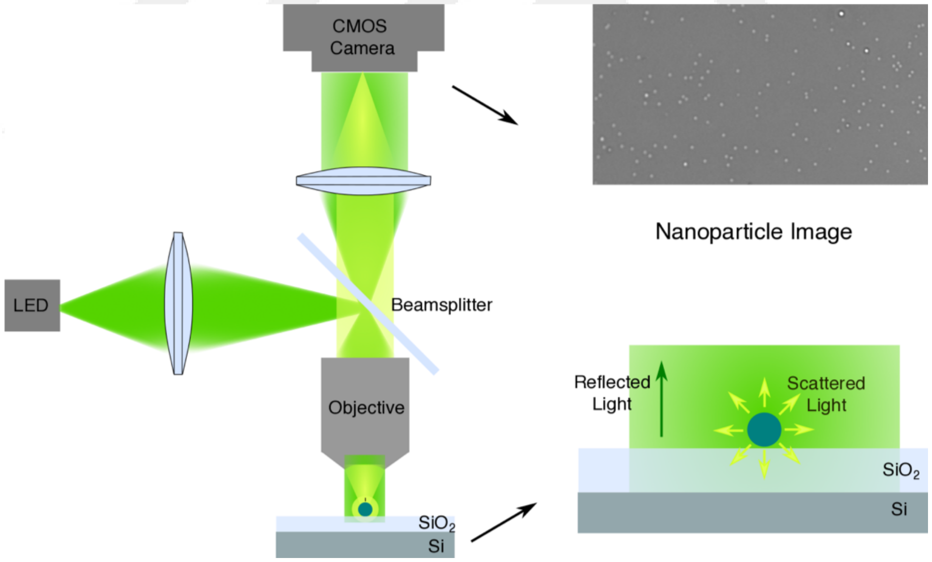

Figure 3.2: Interferometric Microscopy Optical Setup. Nanoparticles are immobilized on top of a thin film sample substrate which is illuminated with a LED in widefield configuration. Scattered field and reference field is collected with a high magnification objective lens and imaged to the camera to have interferometric images.

3.3.2 Data Acquisition and Processing

In order to utilize this defocusing behaviour to selectively enhance the nanoparticle images, we introduce the depth scanning correlation (DSC) technique as shown in Figure 3.3. Sample stage is actuated in z-direction and a cross-correlation analysis is performed between the actuation signal and every pixel in the captured images (Figure 3.3). Pearson correlation coefficient ρ is calculated for every pixel location (x, y) as follows,

$$I_{corr}(x,y) = \rho(x,y) = \frac{1}{N-1}\sum_{z=z_0}^{z_{N-1}}\left(\frac{I_z(x,y) - <I(x,y)>}{\sigma_I}\right)\left(\frac{R(z) - <R>}{\sigma_R}\right) \tag{3.5}$$

where $I_z(x,y)$ and $R(z)$ are the pixel's intensity and the actuation signal's level at axial position z, while σ_I and σ_R are the standard deviation of pixel intensity and actuation signal, respectively. $< I(x,y) >$and $< R >$ denote the values of pixel intensity and actuation signal over one period. The final correlation image is composed of the correlation values of each pixel. Deducing from Equation 3.5, ρ can get values between -1 and 1. $\rho = 0$ corresponds to highly uncorrelated signal, whereas $\rho = 1$ indicates a highly correlated signal (Negative values correspond to anti-correlated behaviour). In order to obtain a highly correlated signal for the background signal, and thus distinguish nanoparticles from the background, the illumination is slightly tuned to have a converging beam on the sample so that the background will vary along z-scan. In this way, an inverse relation between the background signal intensity and the axial position (actuation signal) of the sample is achieved as shown in Figure 3.3 , with a <0.5% variation in background signal over one period.

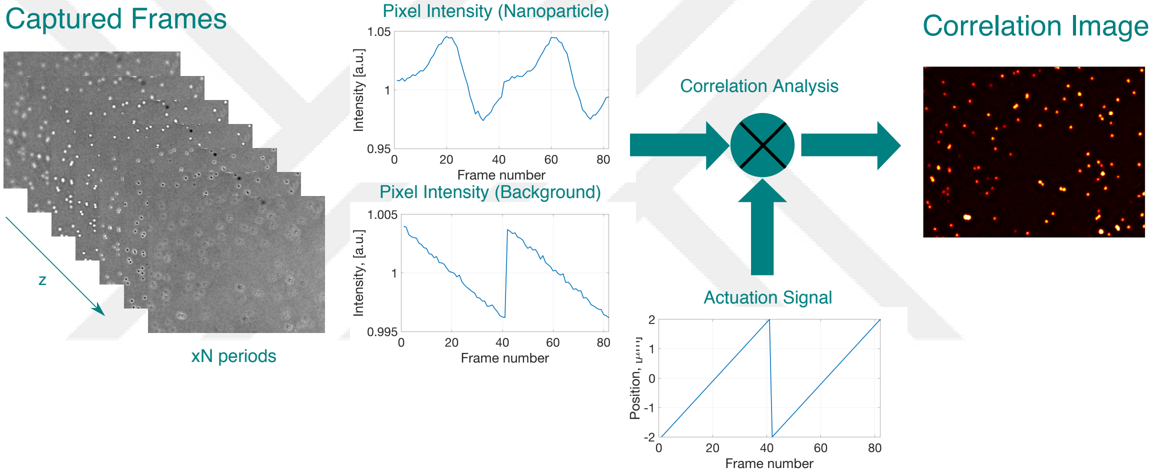

Figure 3.3: DSC Image Generation Algorithm Workflow: An image stack is captured by actuating the sample stage in axial direction and cross correlation analysis is performed between the pixel intensity value and the actuation signal (position of the sample stage) for each pixel individually. The correlation image is composed of calculated cross-correlation values.

3.4 Experimental Results

3.4.1 Detection of Polystyrene Nanoparticles

The proposed technique is used to enhance the visibility of the nanoparticles. The performance of the method is first tested with polystyrene (PS) nanoparticles. Particles with a mean diameter of 100 nm and 50 nm are immobilized on separate substrates, and after a rough initial focusing, the sample stage is actuated with 100 nm steps for a total of 10 μm z-displacement. Captured image stacks are processed to calculate (i) difference image (in which a peak to peak difference is calculated for each pixel) and (ii) DSC image. In DSC image generation a simple search algorithm for finding the optimum axial sweep region that maximizes the SNR of the particles is implemented. In Figure 3.4, the difference image (a) and the DSC image (b) for 100 nm PS particles are shown. In Figure 3.4-d, it is demonstrated that there is an enhancement of 2-fold in the signal to noise ratio (SNR) of individual nanoparticles with the DSC method.

In Figure 3.5 the difference and DSC images of polystyrene particles with 50nm mean diameter are shown. Similar to 100 nm particles, DSC improves the SNR of 50 nm particles significantly. However, a wide variation in SNR values is observed. This might be due to heterogeneity in the size of the particles and particle aggregates or the distance the particles is less than the diffraction resolution limit. In order to investigate special cases, Scanning Electron Microscopy (SEM) images of a number of specific areas are captured. In Figure 3.6 DSC images and corresponding SEM images are given. As it can be seen from the Region 1 and Region 2 in Figure 3.6-b, the contrast of the nanoparticles in DSC images are correlated with the size of the particles. However, it can be inferred from Region 3 that the particle aggregates have higher SNR. Similarly, the particles that are closer to each other than the diffraction

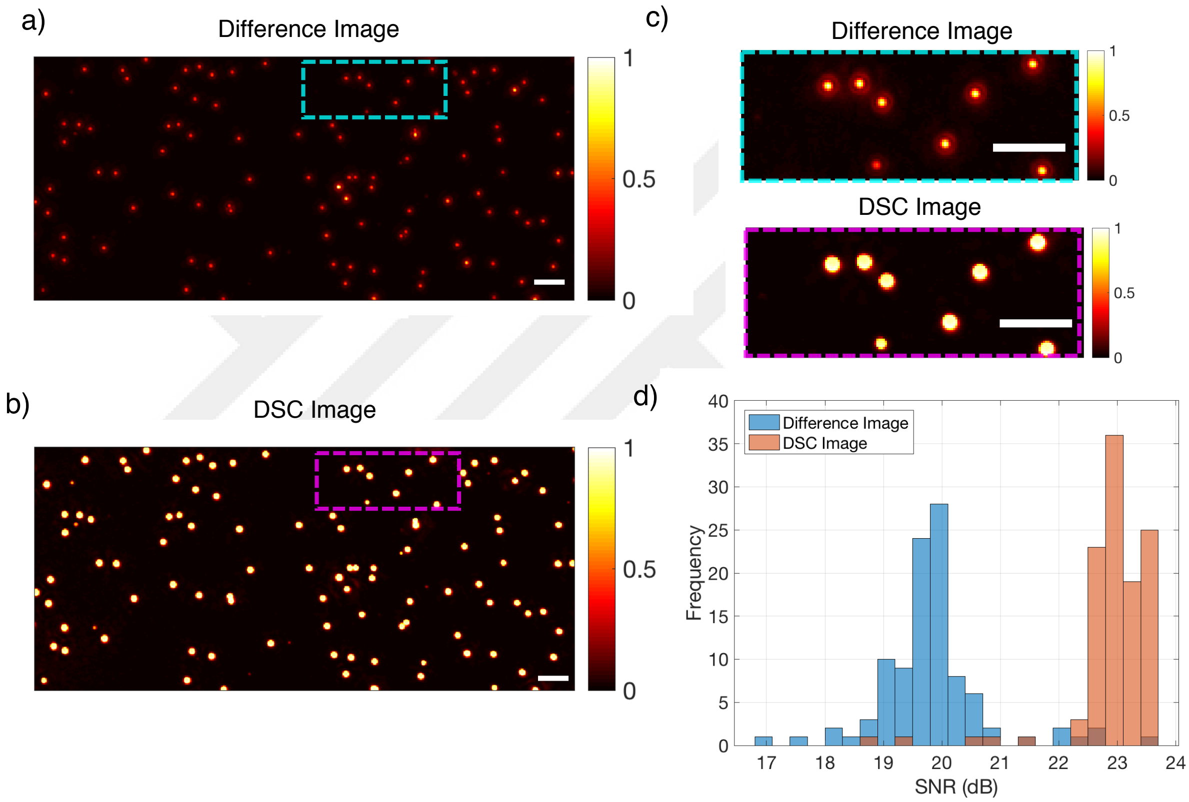

Figure 3.4: a) Difference and b)Depth Scanning Correlation image of polystyrene particles with 100 nm mean diameter. Scalebar is 5 μm c) Zoomed in images of (a) top and (b) Scalebar is 1 μm d) SNR distributions of the detected particles in both methods

limited resolution appear as bright spots (high SNR) in our DSC images (Region 4 in Figure 3.6-b).

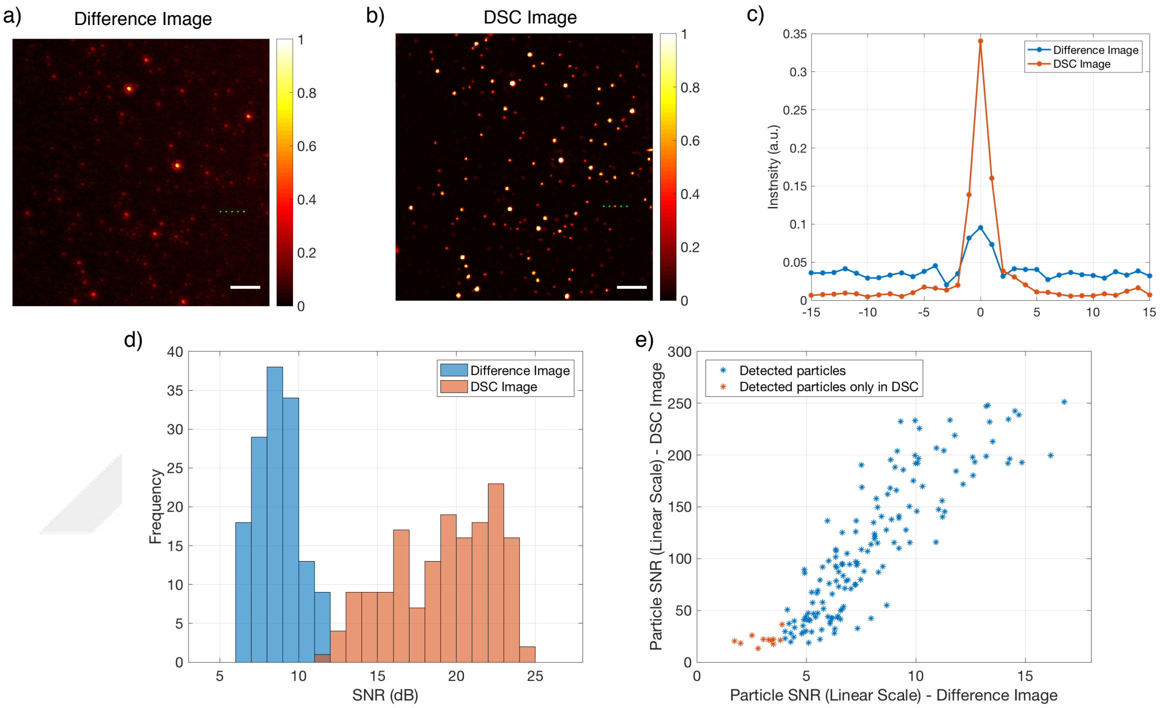

Figure 3.5: a) Difference and b)Depth Scanning Correlation image of polystyrene particles with 50 nm mean diameter. Scalebar is 5 μm c) Lineprofile along the dashed lines shown in (a) and (b) d) SNR distributions of the detected particles in both methods e) Particle SNR comparison for both methods

In order to demonstrate that depth scanning correlation enhancement enables the detection of smaller nanoparticles by analysing the difference images alone, we performed experiments that incorporate smaller nanoparticles. In Figure 3.7, we present a comparison between images obtained with both methods. In Figure 3.7-c, Scanning Electron Microscope (SEM) images of the same region are given. The

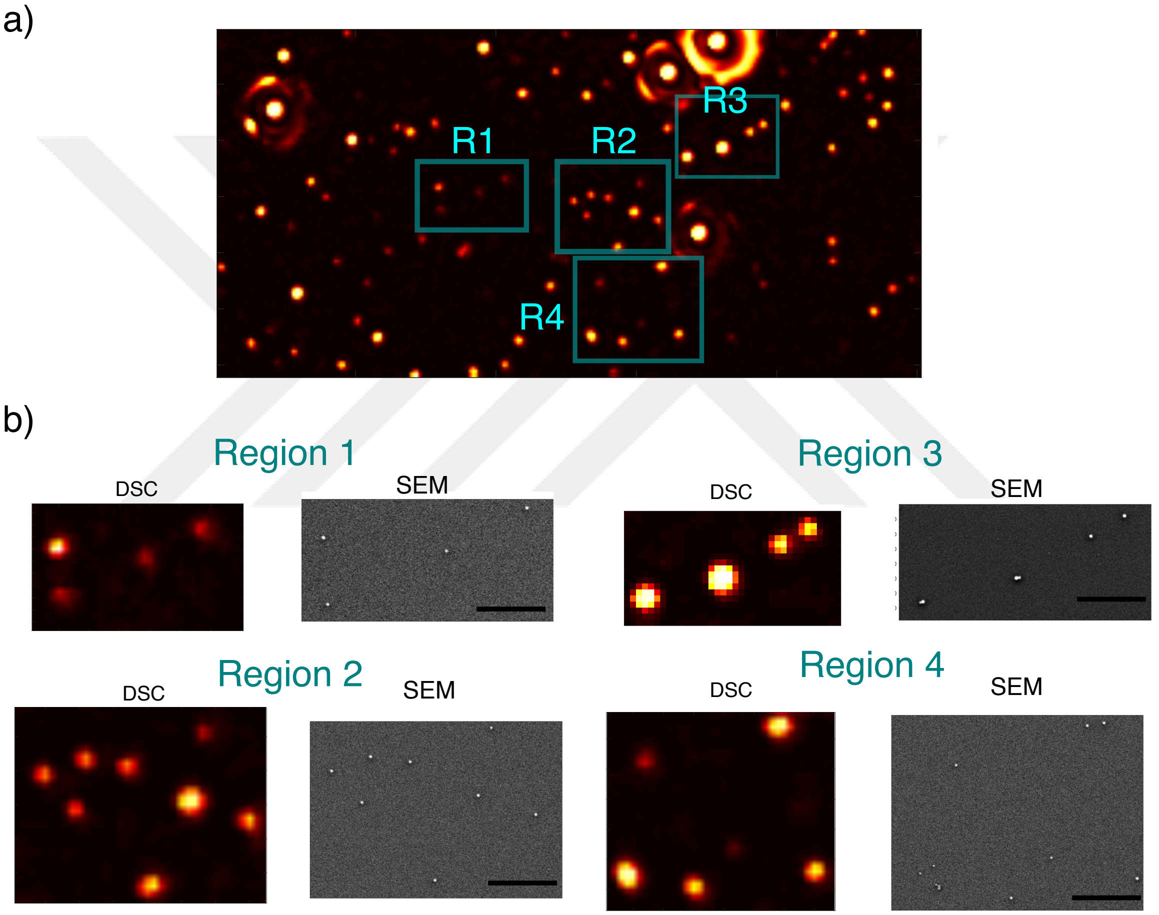

Figure 3.6: a) DSC image of polystyrene particles of various sizes b) SEM and DSC images of selected regions. Scalebar is 1 μm

diameter of the smallest particle (32.88 nm) is measured by focusing to the particle with SEM (Figure 3.7-c-right). This particle is detected in the DSC image with an SNR of 14.93 (11.74 dB) indicated with a green arrow (Figure 3.7-b-right)

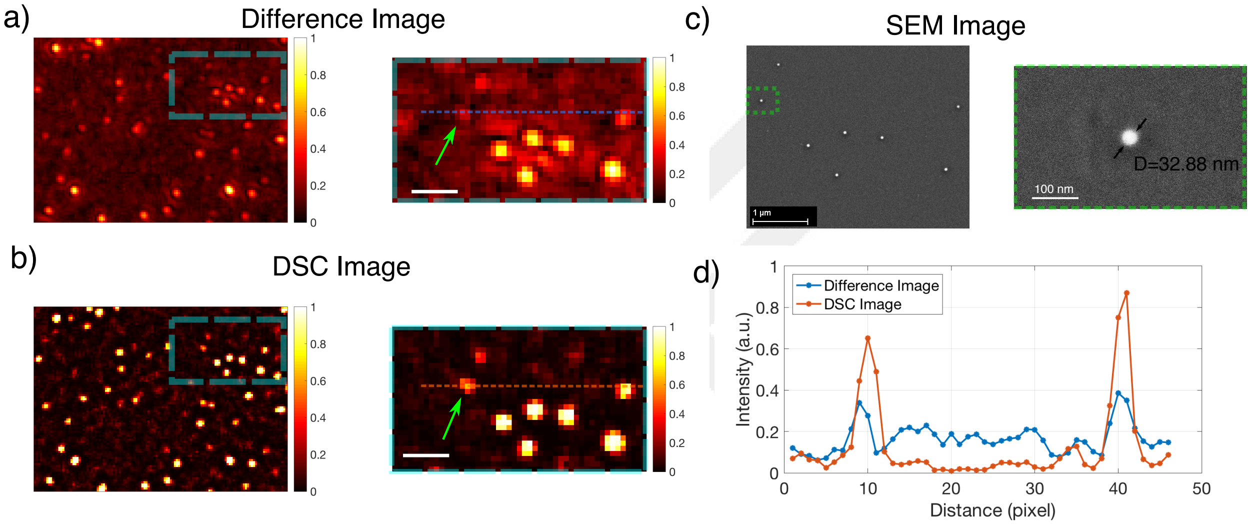

Figure 3.7: a)Difference and b)DSC image of various sized polystyrene particles. Scalebar in zoomed in images is 1 μm. c) SEM image of the same region and focused SEM image of the selected particle which is also visible in DSC image d) Lineprofiles along the dashed lines shown in (a) and (b)

3.4.2 Signal to Noise Ratio vs Defocus Range in Depth Scanning Correlation Interferometric Microscopy

Depth Scanning Correlation Interferometric Microscopy that we introduce in this work utilizes the defocused images to enhance the visibility of immobilized nanoparticles. Determination of the optimum defocus range is critical for maximizing the signal to noise ratio of detected particles especially for the ones that with a diameter smaller than 50 nm. Typical defocus curves for different nanoparticles are given in Figure 3.8. Note that the envelope as well as the amplitude of the interferometric signal is scaled with the size of the particles. In Figure 3.9, variation of experimentally measured particle signal (Pearson coefficient) with respect to depth scan range is presented. If the nominal focal plane is selected as the end point of the defocus window, the highest signal intensities are acquired.

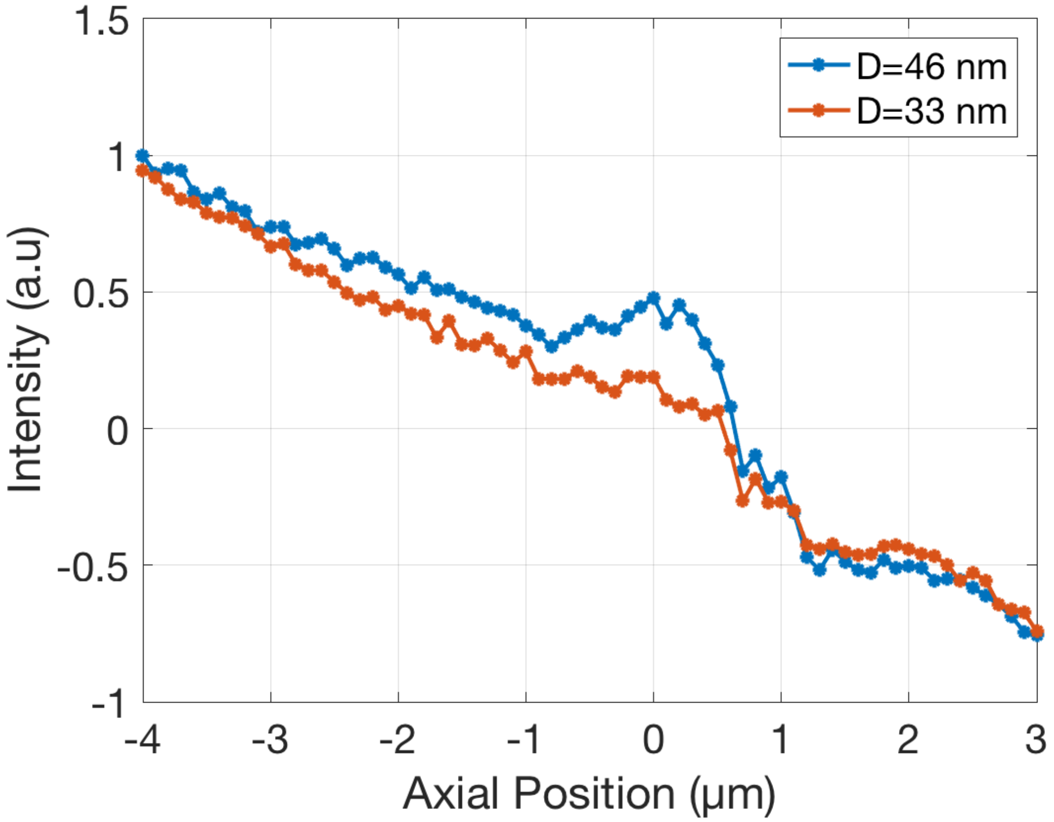

Figure 3.8: Experimental defocus response of 46 nm diameter and 33 nm diameter polystyrene particles.

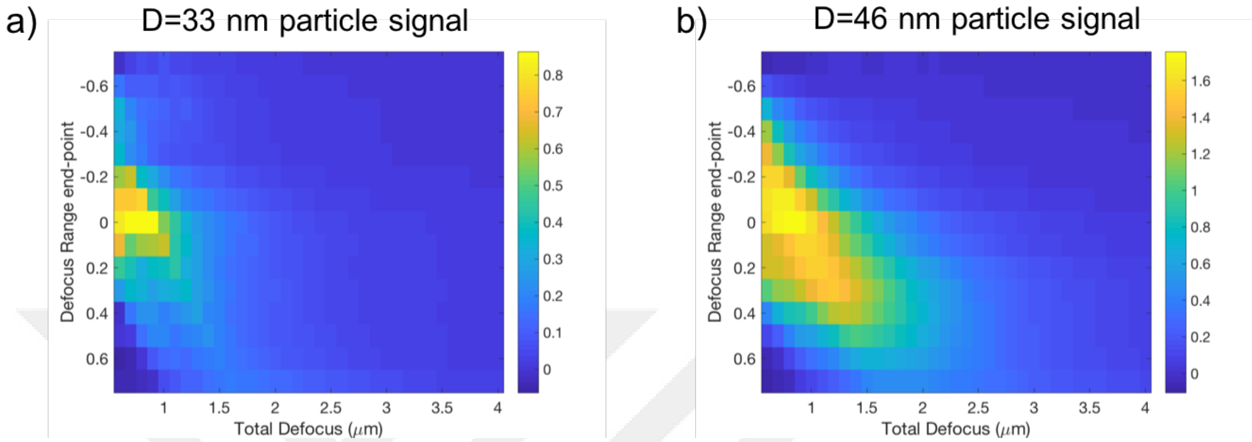

Figure 3.9: Calculated particle signals for different defocus windows. a) D=33 nm polystyrene particle b) D=46 nm. In order to have highest signal, nominal focal plane should be selected as the end point of the defocus range. Optimum total defocus depends on the size of the particle.

In Figure 3.10 a-b, particle signal and noise level as a function of total defocus range is given, respectively. As expected, by increasing the defocus range the noise level is decreased, due to averaging. On the other hand, the particle signal initially increases up to a certain point (where the interferometric signal starts to inhibit positive contrast on background) and then it decreases. In terms of noise, wider the defocus range is better. However in terms of signal, we have an optimum defocus range. In Figure 3.10-c, signal to noise ratio of these two particles is given.

Depending on the particle size, there is an optimum point to have maximum SNR. In this example for the 44 nm nanoparticle, the optimum depth scan range is [-1.5,0] μm, while for the 33 nm particle, the optimum defocus range is [-0.9, 0] μm. This shows that even though the size of the particle and the DSC SNR are correlated, the determination of the size is not straightforward, especially for heterogeneous samples

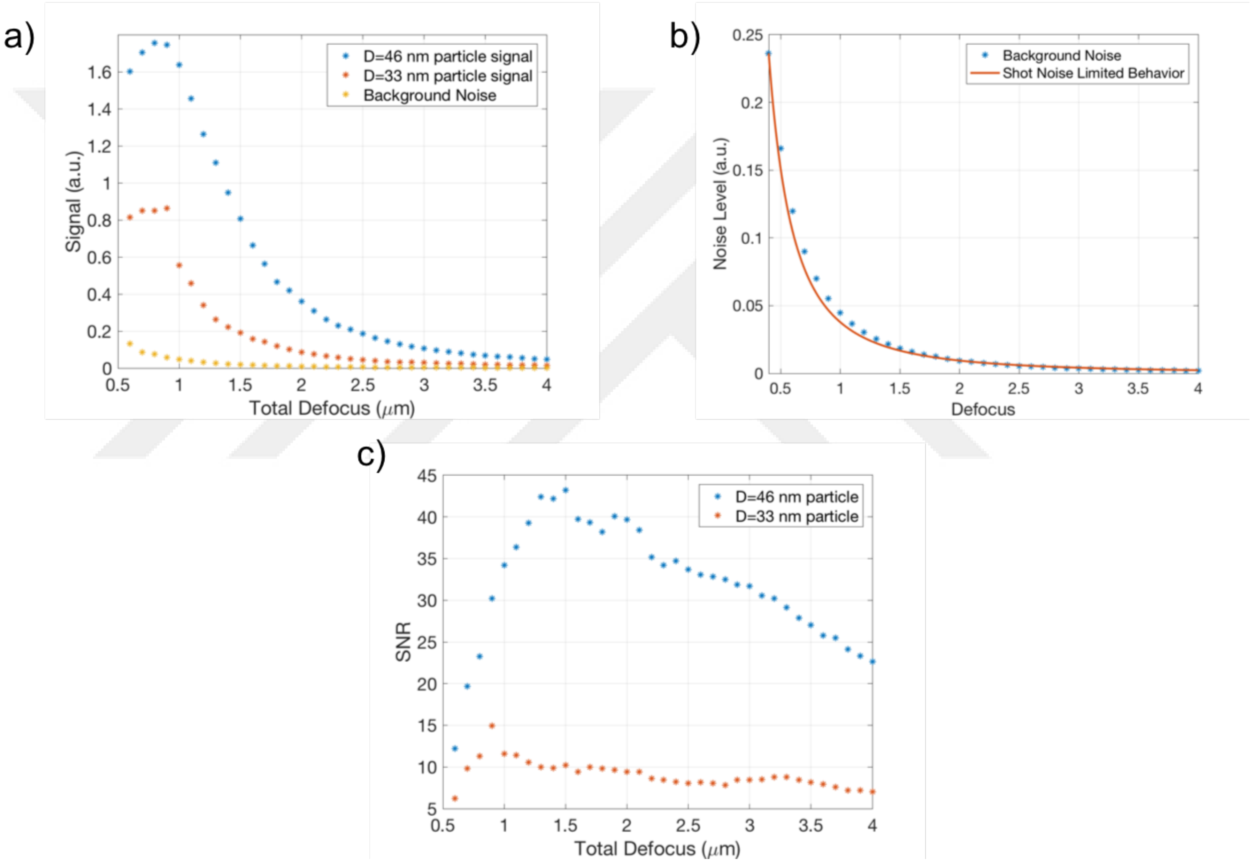

Figure 3.10: SNR dependence to defocus range

as DSC images are highly sensitive to analysis parameters.

3.5 Conclusions and Outlook

In this chapter, a new method, DSC interferometric microscopy is proposed for the detection of dielectric nanoparticles. It is shown that the integration of mechanical actuation to interferometric imaging can be used to further enhance the visibility of the nanoparticles. The utilization of defocusing improves the detection of the presence of the particles due to their unique defocusing response. Using correlation analysis, this response can be used to selectively amplify the particles in the image, while suppressing the background. Similar to the other interferometric detection techniques, the SNR of a particle carries information about the size of the particle (scaled with the volume). We experimentally showed that this method can be used for the direct detection of dielectric nanoparticles as small as 32 nm in diameter without using any optical or mechanical resonant behaviour. We anticipate that the presented method can be used for a wide range of applications ranging from sample characterization to diagnostics, where label-free detection of individual biological nanoparticles is needed.

Chapter 4

ROBUST SIZE DETERMINATION IN DEPTH SCANNING CORRELATION INTERFEROMETRIC MICROSCOPY

4.1 Motivation

Interferometric microscopy proved to be useful for detection of nanosized particles, however its sizing capability is limited. Interferometric images are highly sensitive to the axial position of the sample as well as the size of the particles. Especially for applications of biological particle detection, quantification is even more challenging due to irregularities on the sensor surface introduced by special surface activation procedures. Depth Scanning Correlation improves the sensitivity limit of interferometric microscopy by utilizing depth scan images. However SNR of detected particles is highly dependent on defocus range. In this chapter we demonstrate that size information of the detected particles can be estimated by using theoretical model. First we discuss the Bayesian Inference framework in Section4.2. In Section 4.3, we introduce the theoretical model that we used in the analysis. Then, in Section 4.4, experimental results are given.

4.2 Bayesian Inference

Bayesian inference aims to draw conclusions from observed data. These conclusions can be either validity of a model or parameters of the model assuming that the model is correct. Statistical inference acknowledges that experimental results are always incomplete and contains measurement errors. Therefore, in contrast to deductive inference method which gives definite yes-no answers or exact model parameters, statistical inference produces probabilistic conclusions.

Bayesian inference depends on the Bayes' theorem which is given below;

$$p(H|D,I) = \frac{p(H|I)p(D|H,I)}{p(D|I)} \tag{4.1}$$

where H denotes the proposition asserting the truth of hypothesis (model parameters, or model itself !), I stands for the proposition representing prior information, and D is the proposition representing the experimental data. Therefore, probabilities in Equation 4.1 can be defined as

$p(H|D,I)$: posterior probability of hypothesis

$p(H|I)$: prior probability of hypothesis

$p(D|H,I)$: probability of obtaining data D, if H and I are true (likelihood)

$p(D|I)$: normalization factor

Normalization factor $p(D|I)$ ensures that integration of posterior distribution over all possible hypothesis space (i.e. possible parameter values) is equal to unity. Therefore,

$$\int p(H|D,I)dH = \frac{\int p(H|I)p(D|H,I)dH}{p(D|I)} = 1 \tag{4.2}$$

normalization constant can be written as,

$$p(D|I) = \int p(H|I)p(D|H,I)dH \tag{4.3}$$

Therefore, Bayes' relation (Equation 4.1) can be rewritten as

$$p(H|D,I) = \frac{p(H|I)p(D|H,I)}{\int p(H|I)p(D|H,I)dH} \tag{4.4}$$

In parameter estimation problems, generally one is interested in determining more than one parameter. Calculation of the integral in the denominator in Bayes? formula can be difficult. There are different simulation methods to increase computational feasibility of Bayesian inference. Implementation of Markov Chain Monte Carlo (MCMC) methods is common practice to find posterior probability distribution. MCMC is the general name given to different algorithms that generate a chain of values sampled from the posterior distribution. The term ?Monte Carlo? denotes the algorithm used for generating a random number, and Markov Chain refers to the step in which the generated chain is checked if it satisfies the Markov property (random variable x[n] depends on x[n-1], but does not depend on x[n-2],x[n-3]... x[1],x[0] etc). Here, we use Metropolis-Hasting (MH) Algorithm to implement MCMC. In MH algorithm, initial parameter set θ_0 is generated from the prior distribution $\pi_0(\theta)$ and assigned as θ_{old}. In each step a candidate parameter set θ^* is generated from a proposal distribution $q(\theta^*|\theta_{old})$ (i.e. same as prior distribution with a mean at θ_{old}, or a uniform distribution as in original paper [76]. Then, a coefficient called Metropolis ratio (r) which is the ratio of the likelihood for the candidate and previous parameters is calculated to decide whether to accept the candidate θ^* as θ_{new}.

$$r = \frac{p(\theta^*|y)}{p(\theta_{old}|y)} \frac{q(\theta_{old}|\theta^*)}{q(\theta^*|\theta_{old})} \tag{4.5}$$

if $r > 1$, then θ^* is accepted and assigned as θ_{new}. Otherwise another random number (u) is generated from a uniform distribution [0,1], and if $r > u$, then θ^* is accepted. Upon acceptance θ_{new} assigned as θ_{old}. If the proposed candidate is rejected ($r <$

u), θ_{old} is not updated. Same steps are repeated until the parameter distribution converges to the target distribution. Note that there can be cases of the new parameter set being accepted, even though it is not better than the prior set, in order to not get stuck in local minima. Illustration of the algorithm to estimate the posterior probability is shown in Figure 4.1. In this work we implemented this algorithm using an open source MATLAB toolbox [77].

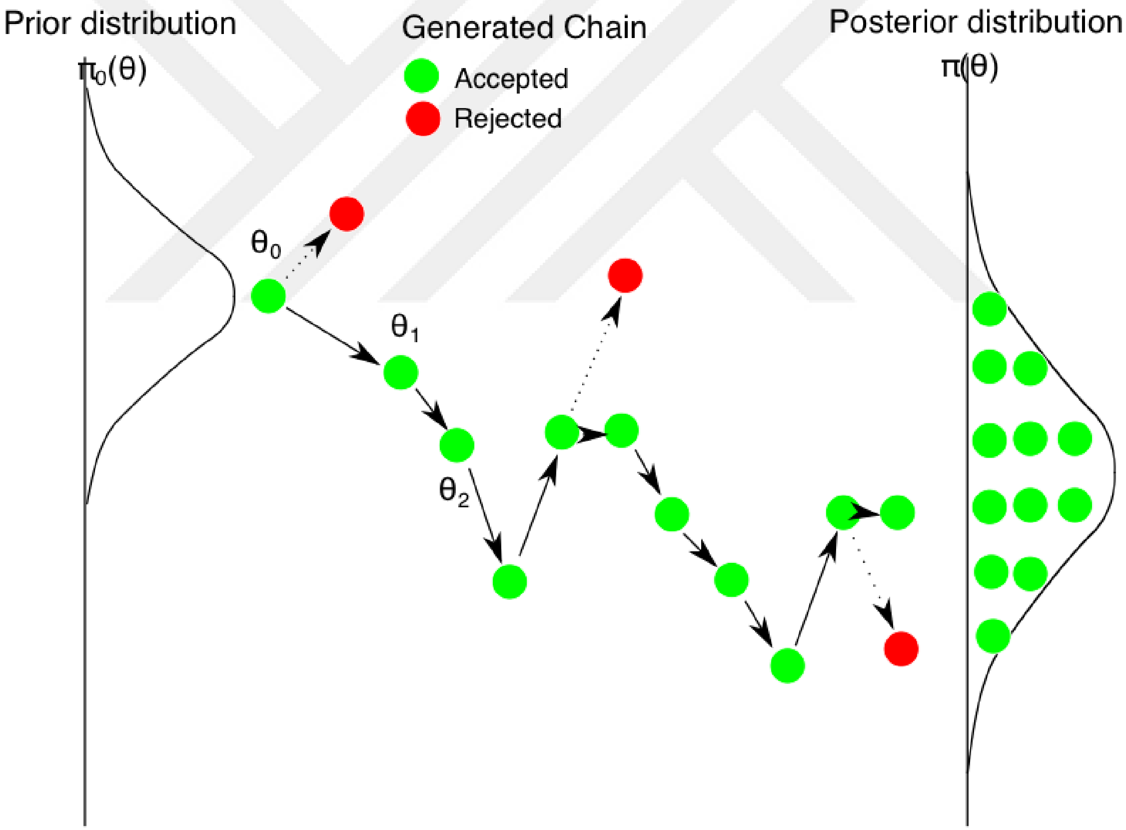

Figure 4.1: Illustration of Monte Carlo Markov Chain. Starting from initial probability distribution, parameter set is generated randomly.

4.3 Theoretical Model and Simulations

Implementation of Bayesian inference requires experimental data and an analytical model. In this work the experimental setup is a wide-field interferometric microscope as illustrated in Figure 3.2. The point spread function of this configuration is carefully analyzed in [78]. Simply, single nanoparticles on top of a layered substrate can be modeled as point dipoles with an orientation determined by the illumination field. Image of each nanoparticle can be calculated by using point dipole of the imaging system. The field due to a point dipole ($\boldsymbol{\mu}$) located at $\mathbf{r_0}$ (Figure 4.2) can be written as

$$E_{scattered}(r') = G(r', r_0).\boldsymbol{\mu} \tag{4.6}$$

where $G(r', r_0)$ is Green's function. In widefield interferometric microscopy signal at detector plane due to a nanoparticle can be written as

$$\begin{aligned} I_t(r') &= |E_{reference} + E_{scattered}|^2 \\ &= |E_{reference} + G(r', r_0).\boldsymbol{\mu}|^2 \end{aligned} \tag{4.7}$$

Derivation of Green?s function is given in Appendix. In short, the total signal can be written as a function of particle size (magnitude of point dipole) and particle height (position of the point dipole). Simulated defocus curves is given in Figure 4.3. As illustrated in Figure 4.3-a depending on the axial position of the sample substrate positive and negative contrast is observed in nanoparticles images. Simulations are in agreement with the experimental data as shown in Figure 4.3-b. In order to demonstrate the effect of particle size on defocus response, particles with various sizes are simulated (Figure 4.3-b). Observing constructive and destructive interference by changing the axial position of the sample might be counterintuitive at first.

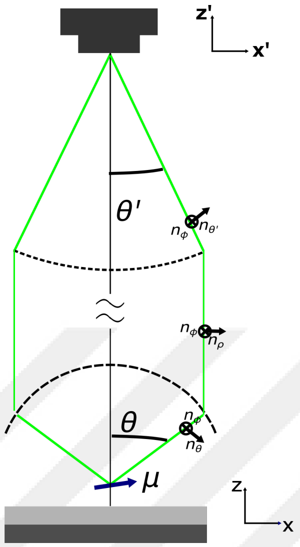

Figure 4.2: Coordinate system and the layout used for the derivation of the theoretical model

Physical distance between the reference mirror (sample substrate) and nanoparticles is not changing, in contrast two double-path configurations (i.e. Michelson interferometers). It is deductive to analyze spectral components of the scattering field. In general, dipole radiation at far field can be written as (Eq.10.32) in [79]).

$$\mathbf{E}_\infty(\theta,\phi) = \begin{pmatrix} E_\theta \\ E_\phi \end{pmatrix} = \frac{k^2}{4\pi\epsilon^2}\frac{e^{ikr}}{r}\begin{pmatrix} \Phi_2\cos\theta\cos\phi & \Phi_2\cos\theta\sin\phi & -\Phi_1\sin\theta \\ -\Phi_3\sin\phi & \Phi_3\cos\phi & 0 \end{pmatrix}\begin{bmatrix} \mu_x \\ \mu_y \\ \mu_z \end{bmatrix} \tag{4.8}$$

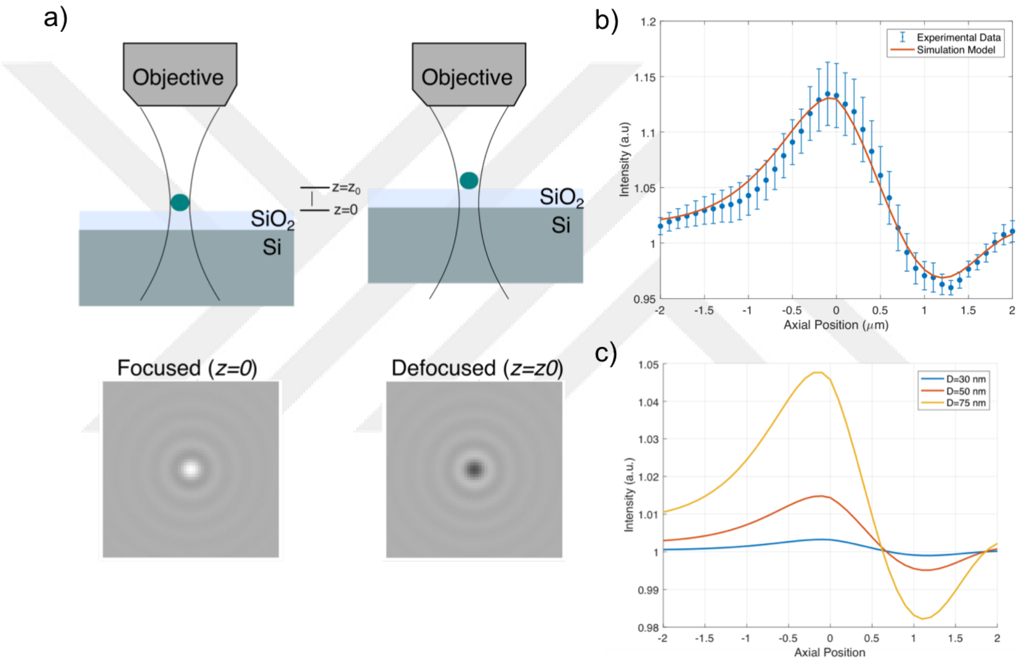

Figure 4.3: a) Simulated nanoparticle images. Depending on the distance between sample and the objective lens, positive or negative contrast can be observed b) Experimental defocus curve (100 nm PS particles) and simulated defocus curve. Errorbars correspond to variation among 20 particles c) Simulated defocus curves for different sized nanoparticles.

where

$$\Phi_1 = [e^{-ikz_0 \cos\theta} + r^p(\theta) e^{ikz_0 \cos\theta}] \tag{4.9a}$$

$$\Phi_2 = [e^{-ikz_0 \cos\theta} - r^p(\theta) e^{ikz_0 \cos\theta}] \tag{4.9b}$$

$$\Phi_3 = [e^{-ikz_0 \cos\theta} + r^s(\theta) e^{ikz_0 \cos\theta}] \tag{4.9c}$$

k is the wavenumber, μ_x, μ_y and μ_z are the point dipole moment components in cartesian coordinates as shown in Figure 4.4-a, z_0 is the axial position of the point dipole, r^s and r^p are the Fresnel reflection coefficients for the s- and p- polarized light respectively. Dipole emission profiles at the back aperture plane of the collection objective lens is shown in Figure 4.4-b. Radiation intensity increases at higher angles (NA). On the other hand, reference field propagates along the optical axis, due to low NA illumination (to have widefield illumination). Therefore, even though the phase of the scattered field and the reference field cannot be adjusted independently, phase difference can be changed by defocusing due to different angular components of these signals, to have constructive and destructive interference.

4.4 Experimental Results

In this work we fitted the model equations to the experimental z-stack data to estimate particle size and particle position (height). Defocus curve of a particle (54 nm) together with fitted curve is shown in Figure 4.5. Solid black curve is the theoretical defocus curve calculated by using the mean values of the estimated parameters. Red curves (n=500) are the samples generated from the posterior distribution of the parameters. In Figure 4.6, posterior probability distributions of particle size and particle height is given. Note that particle size is estimated correctly. We expect that

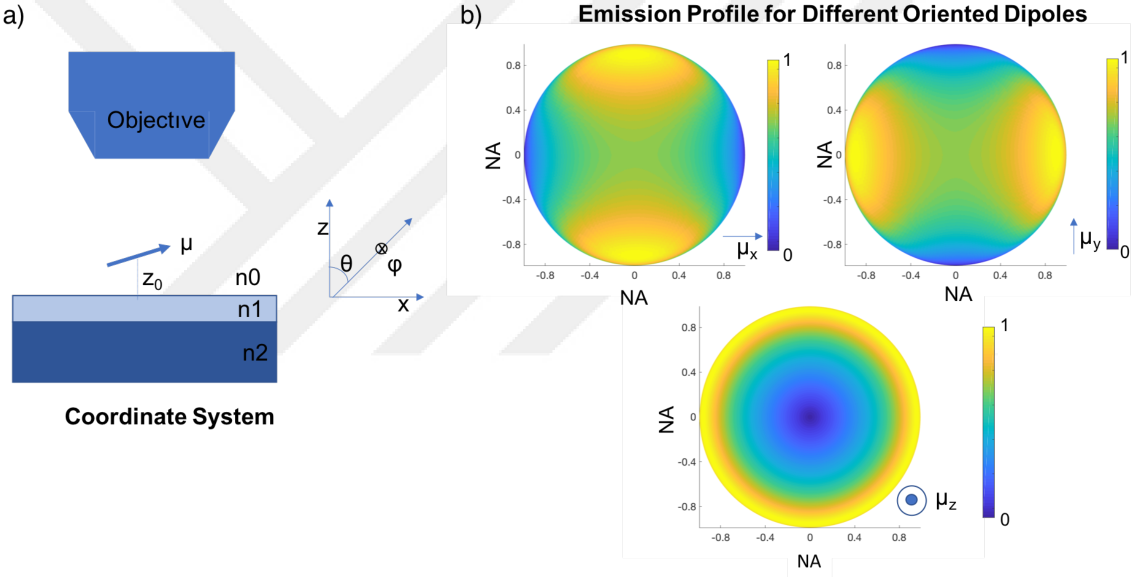

Figure 4.4: Far field emission patterns of point scatterers a) Coordinate system b) Field distributions at back focal plane of the collective objective for different oriented dipoles

the height (center of the dipole) of the immobilized particle to be the radius of the particle, which is also in the range of estimation.

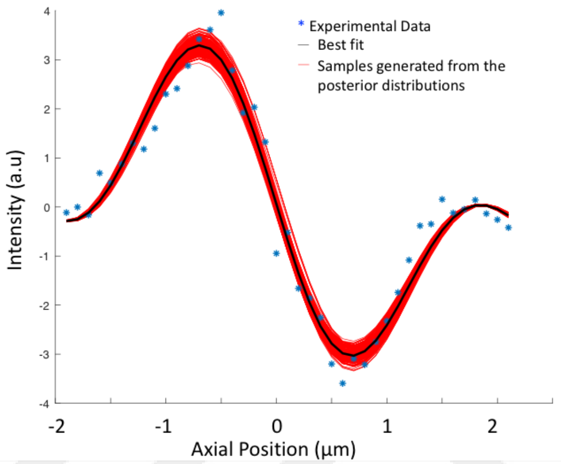

Figure 4.5: Experimental defocus curve of polystrene nanoparticle with 54 nm and Bayesian Fit results. Blue dots are experimental datapoints. Solid black curve is the best fit. Red curves are the sample curves generated from the posterior distributions

Generated chains during the parameter estimation is shown in Figure 4.7. Distant initial points are selected intentionally to test whether the algorithm is converging or not. As can be seen from the figure, after an initial search phase, chain is sampled from the posterior probability of the parameters. Once the model parameters are determined, defocus curves can be reconstructed using the analytical model. In Figure 4.8, interferometric images with various sizes of polystyrene particles which are processed using different techniques are shown. DSC enhances the visibility of the particles as discussed in the previous chapter. However, size determination is not straightforward.

Disadvantage of Bayesian fitting is the high computation cost. In order to decrease

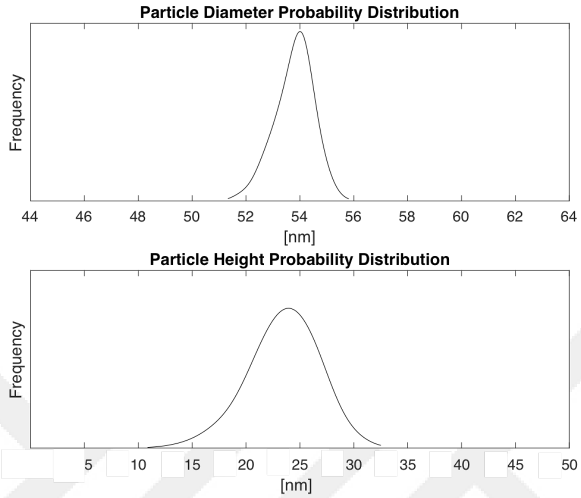

Figure 4.6: Generated posterior probability distributions for the data given in Figure 4.5

computation time, we applied DSC algorithm to the acquired data to detect particles first. Once the particles or candidate particles are detected, MCMC fit is applied to corresponding pixels only.

In order to determine the true size of the particles, SEM image of the same region is captured. SNR of the detected particles in DSC images vs their size is shown in Figure 4.9-a. SNR of the particles larger than 50 nm is very similar. The size discrimination capability is quite limited due to saturation. Besides, SNR distribution of the particles with 45 nm diameter is quite wide. On the other hand, as the particle size is a model parameter, size can be estimated directly in Bayesian approach. In Figure 4.9-b, estimated size of the same particles are given. In contrast to DSC, no saturation but a linear trend is observed.

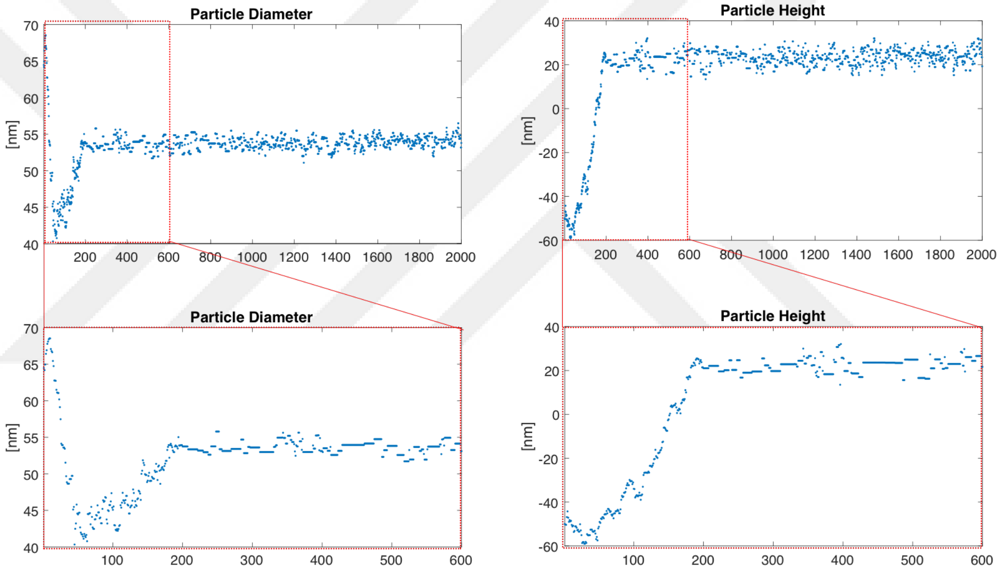

Figure 4.7: Generated Monte Carlo Markov Chains for particle size and particle height estimation. Note that even though initial guess is bad, parameters quickly converges to optimum values

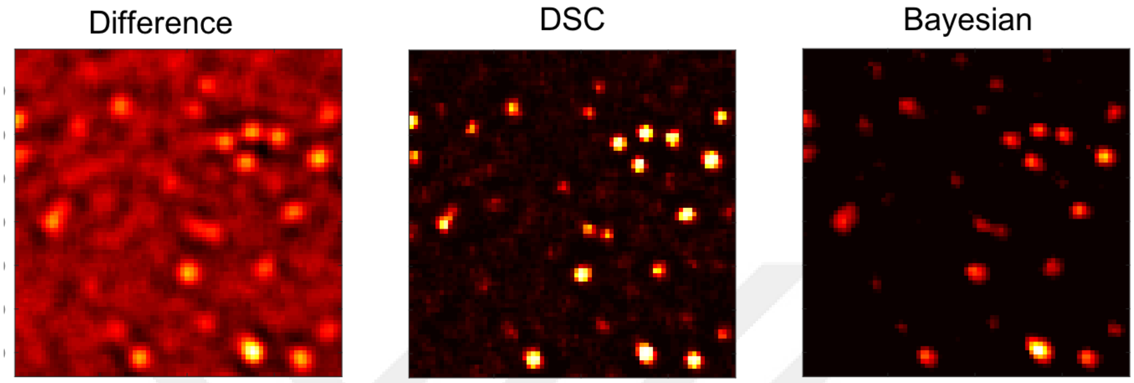

Figure 4.8: Interferometric images of various sized polystyrene particles generated using different techniques. Upon acquiring z-stack images a) Difference: by taking difference between maximum intensity and minimum intensity. b) Depth Scanning Correlation: correlation analysis on a pixel-by-pixel basis is performed c) Bayesian inference (model fit) to estimate the particle size

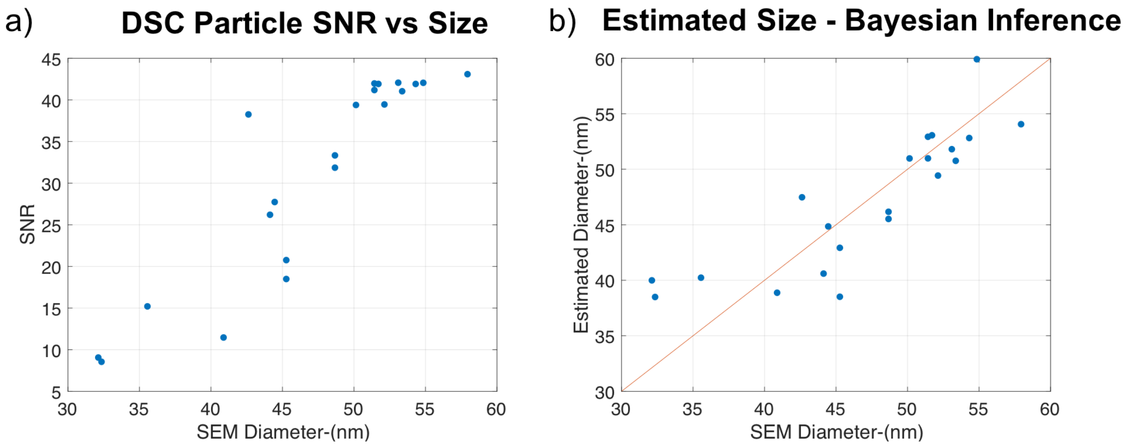

Figure 4.9: a) Size vs SNR of detected particles in DSC images b) Estimated size of the same particles using MCMC Fit. Red curve is the y=x curve

4.5 Conclusions

Interferometric microscopy proved to be a sensitive technique for nanosized particle detection. However, as sensitive as they are, interferometric images are highly prone to small variations, such as the position of the particle, mechanical oscillations, stability of the sample substrate etc. Thus, quantification of the acquired images is challenging. Robust data processing techniques are needed to improve quantification capability of the method. In the previous chapter we introduced Depth Scanning Correlation (DSC) technique to improve the visibility of nanosized particles. However, size determination capability is limited, as SNR is highly dependent on analysis parameters. In this chapter we demonstrated that, utilization of the theoretical model in the data analysis pipeline is useful for determination of the size of the particles. As model fitting is time consuming, it can be implemented in tandem with the DSC technique. While detection of the particles can be performed by DSC, and quantification can be done with Bayesian inference.

Chapter 5

APPLICATIONS OF DEPTH SCANNING CORRELATION INTERFEROMETRIC MICROSCOPY

5.1 Direct Detection of Single Exosomes

Exosomes are nanometer sized (30-150 nm) extracellular vesicles, found in the body fluids such as blood, saliva, cerebrospinal fluid and urine [80]. They are secreted from nearly all types of cells and contain various molecules including RNAs, DNA, proteins and lipids (Figure A.6). Exosomes play important roles in intercellular communication and transportation of macromolecules between the cells. In recent years, exosomes emerged as potential biomarkers for cancer and neurodegenerative diseases [81, 16]. Specifically, a variety of exosomal biomarkers are discovered for cancer diagnostics such as pancreatic cancer [82], melanoma [83], lung cancer[84], ovarian cancer [85] and prostate cancer [86].

The most efficient way to decrease the mortality rate of cancer is early detection. For example, breast cancer causes the highest number of cancer related deaths among women (over 600.000 deaths in 2018) [87] , however early diagnosis and treatment can increase the 5-year survival rate up to 99% [88]. Thus, effective and sensitive screening methods have a significant impact on decreasing the number of deaths due to cancer [89]. Liquid biopsy techniques based on detection and characterization of biomarkers circulating in body fluids, received great attention as potential screening and monitoring tools [90]. Contrary to conventional tissue biopsy, liquid biopsy provides information from all cancer tumors which is required for determination of an effective end personalized treatment strategy. Furthermore, liquid biopsy techniques are minimally invasive, low cost, high-throughput and potentially provide real-time monitoring of the disease progression and response to treatment. Besides, conventional liquid biopsy targets such as circulating tumor cells of cfDNA, tumor derived exosomes are valuable sources of information about the state of the disease. Although utilization of exosomes holds great potential for clinical applications in early diagnosis and treatment monitoring, rapid, high-yield exosome isolation and robust, sensitive, high-throughput exosome characterization tools are required to translate the exosome research into clinical practice.

Conventional exosome isolation methods such as ultracentrifugation is labor intensive and time consuming. On the other hand, standard analytical characterization techniques such as ELISA or western blot analysis require large volumes of sample and complex labeling procedures [92]. Aside from increasing the complexity of the sample preparation protocols, labelling might also perturb the functionality of the particle of interest. Another characterization tool frequently used in laboratories is Nanoparticle Tracking Analysis (NTA) [93] which measure the concentration and size distribution of the particles. However, this technique does not provide any information about the content of the particles without using labels. Moreover, all these methods provide only ensemble averaged information, making single particle level characterization impossible.

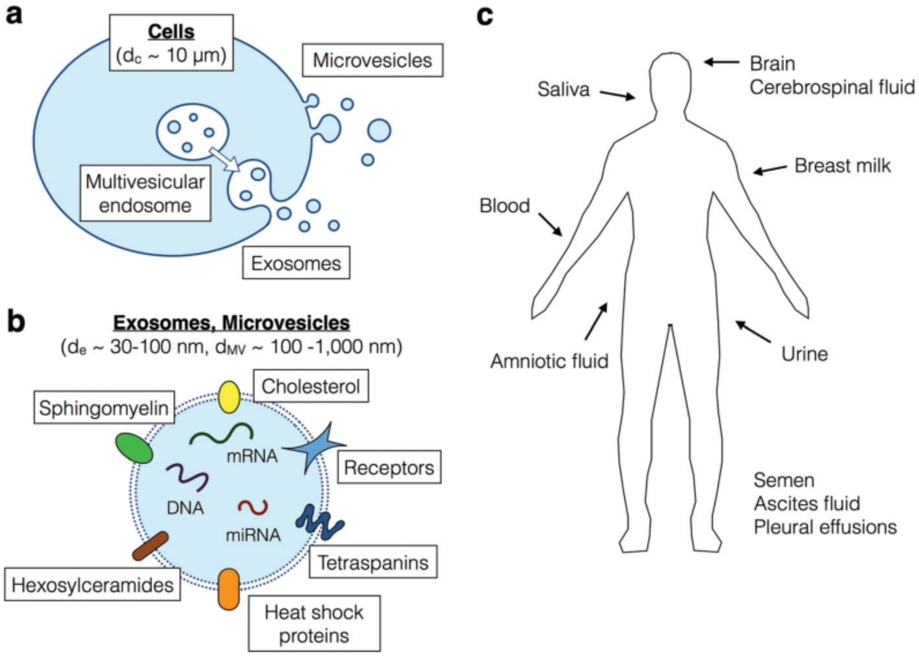

Figure 5.1: a) Exosomes Overview. Exosomes are nanosized particles secreted from cells. b) They contain DNA, RNA, surface proteins and lipids c) Exosomes are found in various body fluids [91].

5.1.1 Isolation of Exosomes from Cell Culture

In this work we utilized the Exosome Total Isolation Chip (ExoTIC) developed at BAMM Laboratory, Stanford University [94]. ExoTIC is a filtration based method which allows purification of extracellular vesicles from various biofluids including cell culture medium, plasma and urine. ExoTIC is a low-cost, easy to built and high-throughput method, that provides higher yields in comparison with other isolation methods such as ultracentrifugation and polyethylene glycol (PEG) based methods. A detailed fabrication and experiment procedure of the ExoTIC is given in [94].

In isolation experiments cell culture medium is injected to the ExoTIC by using a syringe pump with an injection rate of 5 ml/h, as shown in Figure 5.2-a. The cell culture medium is supported with exosome FBS depleted medium 24 hours prior to the experiment. 50 nm membrane filters are used in isolation experiments. While particles with a diameter larger than 50 nm are captured by the membrane filter, the rest of the molecules such as nucleic acids, protein aggregates etc, is passed through the device with excess fluid. Once whole medium is filtered, the chip is unscrewed and the membrane filter is taken out carefully (Figure 5.2-b). Next, the membrane filter is stored inside an eppendorf tube filled with 10 ml PBS solution overnight at +4 C to release the exosomes.

5.1.2 Exosome Detection Experiments

Exosomes isolated from the cell culture are immobilized on top of the sample substrate via spin coating. DSC images of the chip both before and after exosome immobilization are shown in Figure 5.3-a. Placed exosomes appear as bright spots. Zoomed in image of the chip is shown in 5.3-b. Due to the heterogeneous nature of exosomes, a

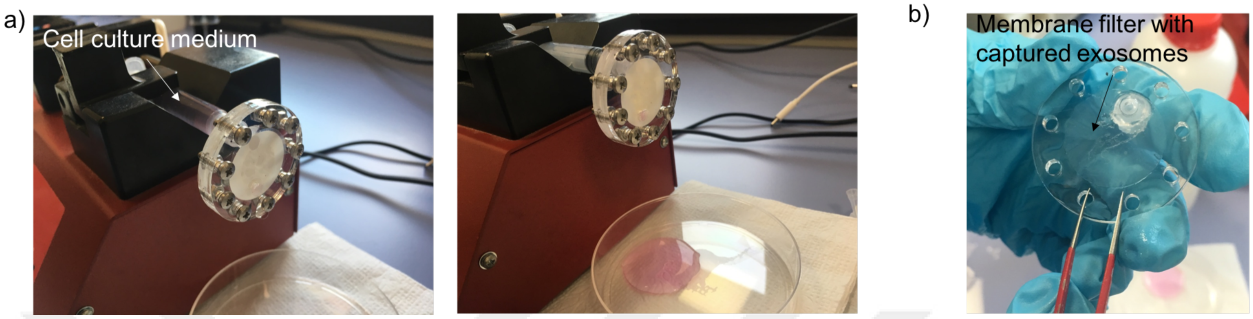

Figure 5.2: Exosome Total Isolation Chip a) Cell culture medium is injected to microfluidic chip using a syringe pump. b) Exosomes are captured by the membrane filter.

variation is observed in SNR of the detected particles as it can be seen inFigure 5.3-c.

In Figure 5.4, SEM and DSC image of the exosomes are given for comparison. The zoomed in image of the same region is given in Figure 5.5. Due to the fragile nature of exosomes, focusing is challenging in SEM. Especially small particles disappear when electrons are focused on them. All of the exosome particles observed in SEM images are also detected in DSC images. Corresponding particle groups are enclosed in circles. DSC images contain more particles compared to SEM images. This may be because SEM causes the smaller particles to evaporate during the scan.

5.2 Visualization of Neutrophil Extracellular Traps(NETs)

Initially described in 2004 [95], neutrophil extracellular traps (NETs) are network of extracellular fibers released by white blood cells in response to various types of pathogens including funghi, virus and bacteria. NETs formation (NETosis) is the suicidal attack of neutrophils to kill the pathogen, when other killing mechanisms are

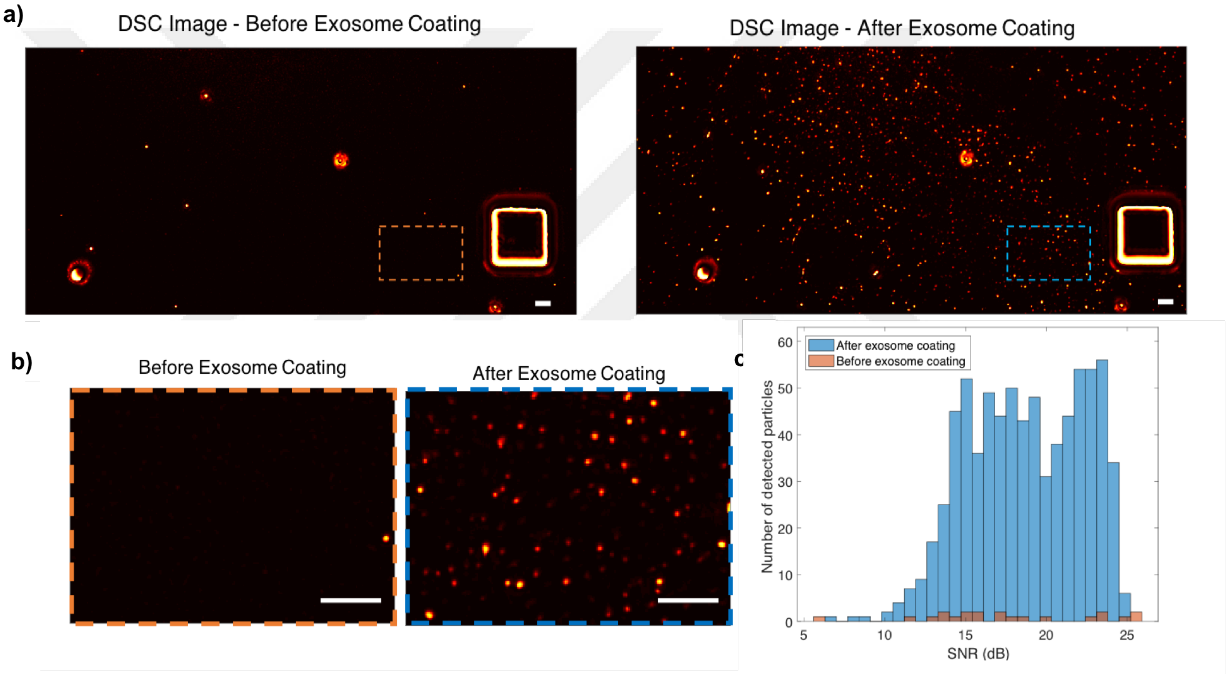

Figure 5.3: Exosome Detection Experiment. a) DSC image of the same region before and after exosome immobilization b) Zoomed in image of (a) c) SNR distribution of the detected particles in (a) Scalebar is 5 μm

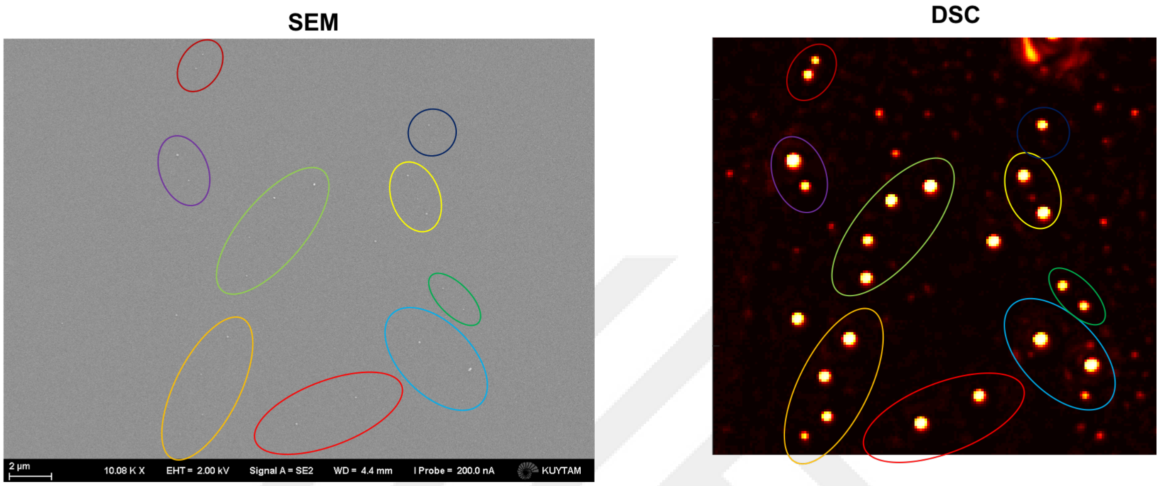

Figure 5.4: SEM and DSC images of exosome sample

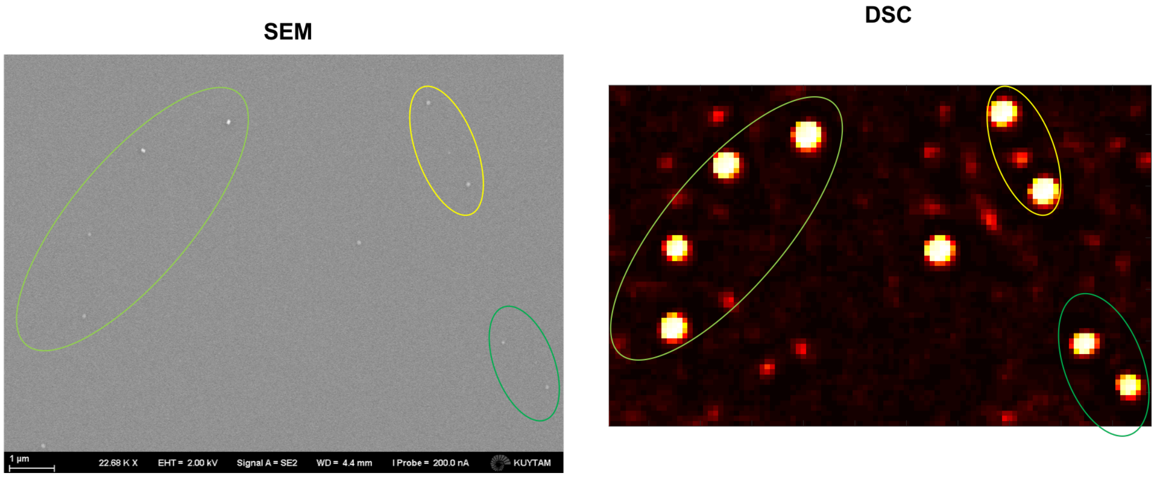

Figure 5.5: SEM and DSC images of exosome sample

unsuccessful, namely phagocytosis and degranulation (Figure 5.7). During NETosis neutrophils arrange their chromatin and granular contents to form web like structures. Following this morphological transformation, neutrophils release these traps to the extracellular medium to capture and destroy pathogens [96, 97].

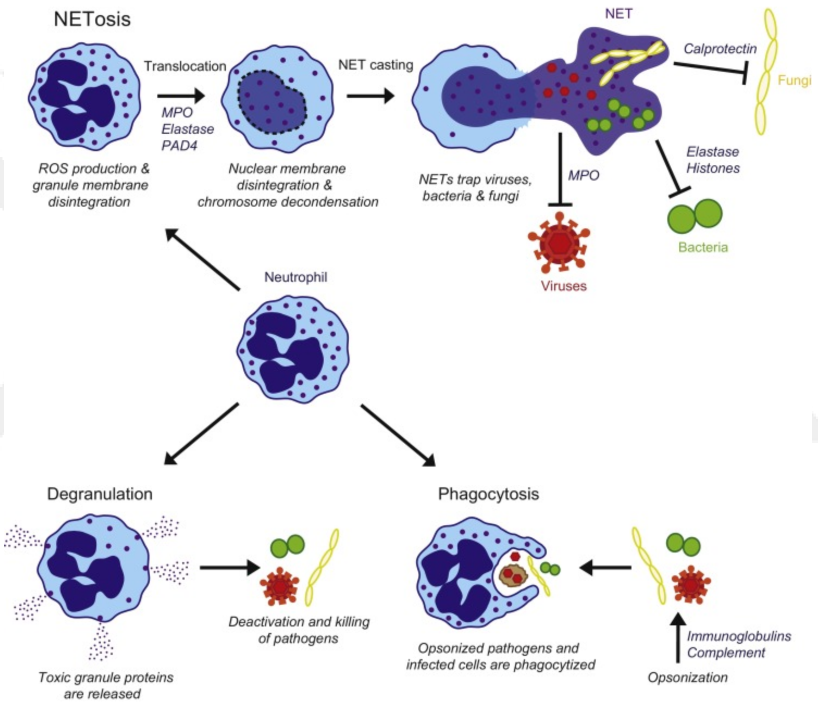

Figure 5.6: Neutrophil defense mechanisms:Triggered by pathogens morphological changes occurs, including formation of NETs, rupture of cell membrane and nuclear envelope, resulting with cell death(NETosis). Other mechanisms are release of toxic proteins (degranulation) and phagocytosis [96]

.

Although they have a central role in immune defense system, NETs can cause pathological conditions [98], such as enhancing platelet binding leading to an increase in the risk of thrombosis [99]. Beside killing pathogens, NETs also damage epithelial and endothelial cells. Excessive NETs formation can also directly or indirectly induce tumor metastasis [100], atherosclerosis [101] or diabetes [102]. In order to understand the role of NETs in various processes, robust quantification tools are needed.

NETs can be visualized by using electron microscopy or fluorescence microscopy [103]. Even though electron microscopy provides high resolution images [104], this technique is not convenient for high throughput measurements. Furthermore, live imaging of cells is not possible with electron microscopy. Current gold standard is fluorescence microscopy with immunofluorescence labeling, which requires neutrophil markers to be labeled. Specifically, immunofluorescence confocal microscopy enables high resolution, localization and high specificity due to utilization of labels. However, in practice the number of available dyes is limited, restricting the number of molecules that can be observed. Furthermore, phytotoxicity and photobleaching limits the observation time.

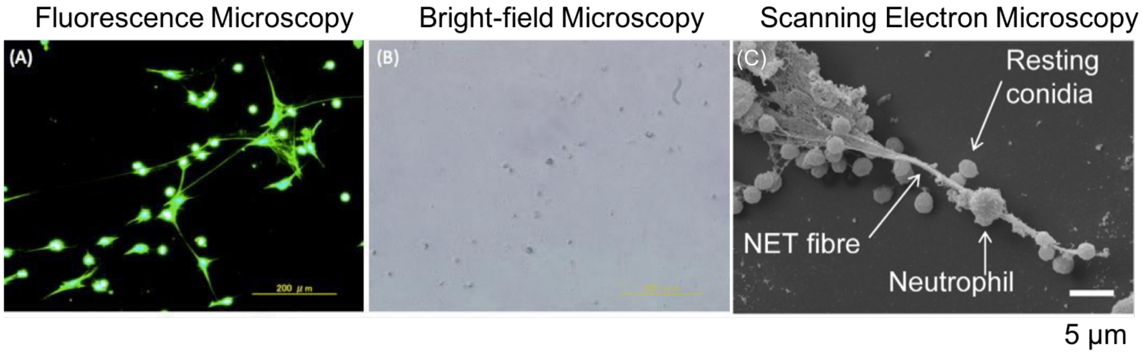

Figure 5.7: NETs images captured with different microscopy methods a) Fluorescence b) Brightfield c) Scanning Electron Microscopy [104]

Interferometric imaging provides label-free images of transparent objects. In Figure 5.9 an image of neutrophil extracellular traps (NETs) captured with our imaging system is shown. Cells and NETs can be distinguished easily due to morphological differences with our label-free method though selectivity is not provided. Because our system measures optical path difference, the resulting interferometric images also carry information about the surface profile. Furthermore, the images contain information about the height of the cell in the form of interference fringes on the cell images.

5.3 Conclusions

In this chapter we demonstrate two biological applications of the developed platform. As a first application detection of individual exosomes isolated from tumor cells is given. Exosomes are extracellular particles, carries information about the origin cell which they are secreted. Quantification and characterization of these particles is quite important in liquid biopsy applications. Secondly, we demonstrate visualization of neutrophil extracellular traps (NETs) without using any labels. Characterization of NETs is important for understanding their roles in disease mechanisms. Developed platform offers high-throughput and sensitive imaging capability that can be used in visualization of NETs, without requiring complex sample preparation procedures.

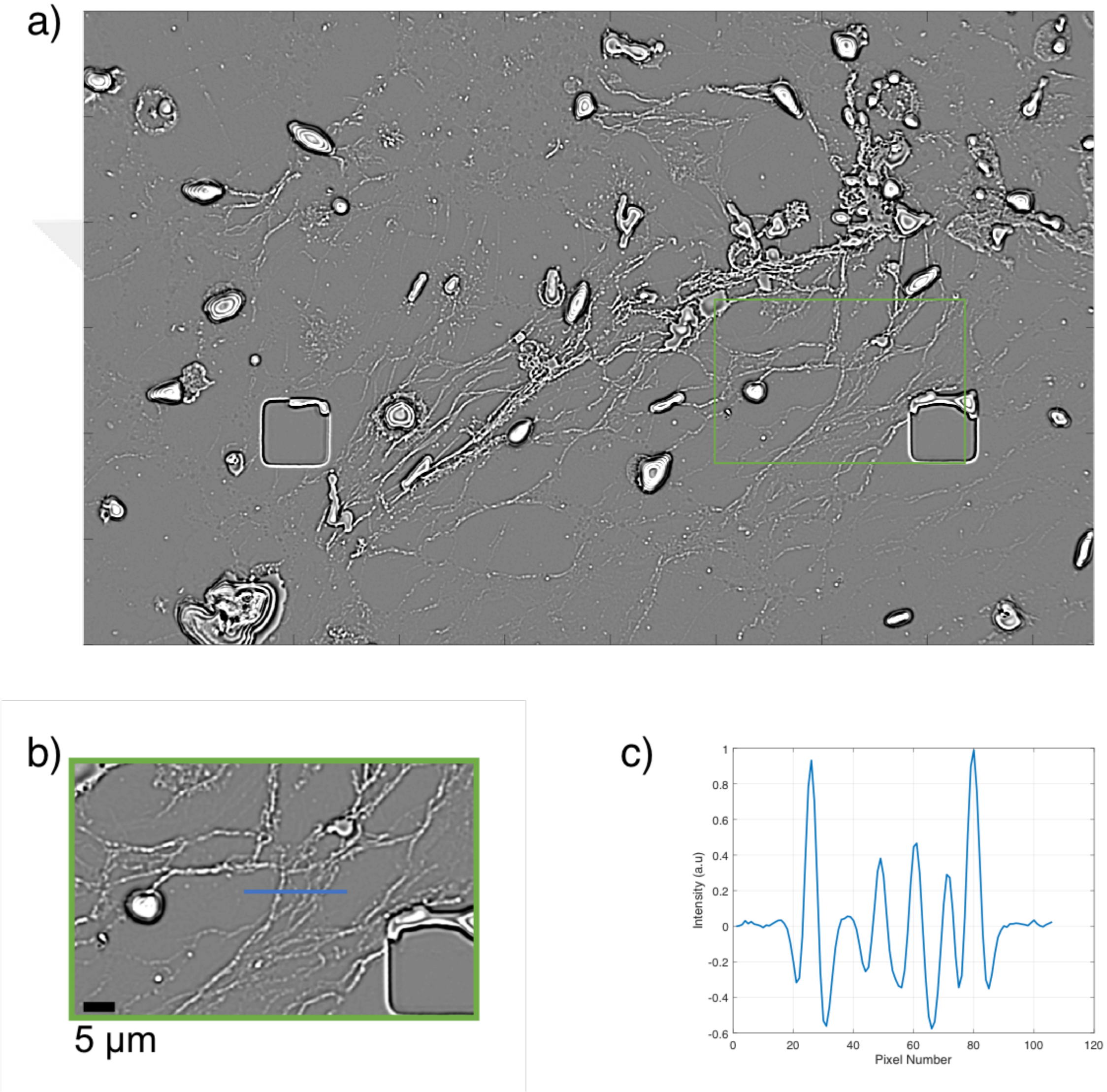

Figure 5.8: Visualization of Neutrophil Extracellular Traps using Interferometric Microscopy

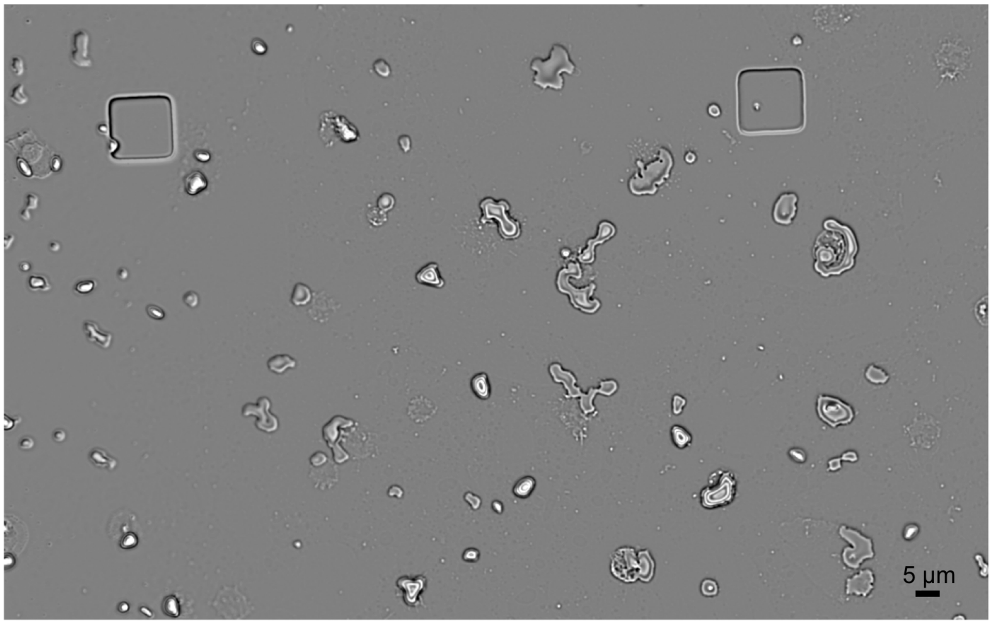

Figure 5.9: Images of neutrophils with no NETs formation

Chapter 6

CONCLUSIONS

In this thesis we introduce two imaging systems and several data processing techniques that can be used for label-free biological nanoparticle detection and characterization applications. We address several challenges present in interferometric detection, such as limited sensitivity and quantification capability.

In Chapter 2 we demonstrate a low-cost, high-throughput, label-free and portable biosensor that is developed by modifying a commercial flatbed scanner, as an example of how commercial electronic devices offer a unique opportunity to scientists and engineers to access sensors, electronic controllers and optical elements with relatively low cost. We explain the mechanical and optical modifications implemented on hardware for developing the biosensor. Then we present the results of DNA hybridization and DNA directed antibody immobilization experiments in microarray format. We show that the proposed system can be used as a biosensor in low resource settings and as a quality control and calibration tool in microarray applications.

In Chapter 3, we introduce Depth Scanning Correlation (DSC) Interferometric Microscopy. This technique is based on utilization of defocused images in interferometric microscopy. We demonstrate that by implementing a correlation analysis, sensitivity level of the system can be improved. Developed system is capable of capturing images with high field of view (200 μm x 300 μm) and can detect nanoparticles as small as 30 nm in diameter.

Depth Scanning Correlation (DSC) technique provides high sensitivity, however its sizing capability is limited. In Chapter 4, we demonstrate that the theoretical model can be used in data analysis pipeline for robust analysis of captured images. We show how the implementation of MCMC fitting to the acquired data improves the estimations on the particle size.

In Chapter 5, two biological applications of the developed imaging system are demonstrated. Firstly, exosomes, tiny bioparticles isolated from tumor cells are detected using DSC. Label-free detection and individual characterization of these particles is critical for translation of exosome research into clinical applications. As a second application we visualize neutrophil extracellular traps (NETs) using developed imaging system. NETs are formed after a special type of cell death called NETosis. NETs are discovered in 2004 and there are still a lot of questions about their role in a variety of biological processes. Developed platform offers label-free images of NETs, which is important for observing their natural behavior.

One practical aspect of DSC is that the correlation analysis can be done in parallel for each pixel. We plan to implement DSC algorithm on GPU in the future, which would decrease computation time drastically. In this way ?realtime? DSC images can be acquired. Similarly, MCMC algorithm which is used for size estimation of the detected particles can also be implemented on GPU. Another important future work is to conduct in fluid experiments. This would enable us to capture live cell images using our label-free method making the visualization of whole NETosis events in realtime possible.

BIBLIOGRAPHY

[1] J. Jeevanandam, A. Barhoum, Y. S. Chan, A. Dufresne, and M. K. Danquah, "Review on nanoparticles and nanostructured materials: History, sources, toxicity and regulations," *Beilstein Journal of Nanotechnology*, vol. 9, no. 1, pp. 1050–1074, 2018.

[2] O. V. Salata, "Applications of nanoparticles in biology and medicine," *Journal of nanobiotechnology*, vol. 2, no. 1, p. 3, 2004.

[3] J. W. Wiechers and N. Musee, "Engineered inorganic nanoparticles and cosmetics: facts, issues, knowledge gaps and challenges," *Journal of biomedical nanotechnology*, vol. 6, no. 5, pp. 408–431, 2010.

[4] R. Ravichandran, "Nanotechnology applications in food and food processing: innovative green approaches, opportunities and uncertainties for global market," *International Journal of Green Nanotechnology: Physics and Chemistry*, vol. 1, no. 2, pp. P72–P96, 2010.

[5] I. Matsui, "Nanoparticles for electronic device applications: a brief review," *Journal of chemical engineering of Japan*, vol. 38, no. 8, pp. 535–546, 2005.

[6] W. J. Stark, P. R. Stoessel, W. Wohlleben, and A. Hafner, "Industrial applications of nanoparticles," *Chemical Society Reviews*, vol. 44, no. 16, pp. 5793–5805, 2015.

[7] D. J. McClements and H. Xiao, “Is nano safe in foods? establishing the factors impacting the gastrointestinal fate and toxicity of organic and inorganic food-grade nanoparticles,” *npj Science of Food*, vol. 1, no. 1, pp. 1–13, 2017.

[8] N. R. Yacobi, F. Fazllolahi, Y. H. Kim, A. Sipos, Z. Borok, K.-J. Kim, and E. D. Crandall, “Nanomaterial interactions with and trafficking across the lung alveolar epithelial barrier: implications for health effects of air-pollution particles,” *Air Quality, Atmosphere & Health*, vol. 4, no. 1, pp. 65–78, 2011.

[9] A. Elsaesser and C. V. Howard, “Toxicology of nanoparticles,” *Advanced Drug Delivery Reviews*, vol. 64, no. 2, pp. 129–137, 2012.

[10] N. Phogat, S. A. Khan, S. Shankar, A. A. Ansary, and I. Uddin, “Fate of inorganic nanoparticles in agriculture,” *Advanced Materials Letters*, vol. 7, no. 1, pp. 3–12, 2016.

[11] A. A. Deniz, S. Mukhopadhyay, and E. a. Lemke, “Single-molecule biophysics: at the interface of biology, physics and chemistry.” *Journal of the Royal Society, Interface / the Royal Society*, no. 18, pp. 15–45.

[12] H. Abdel-Haq, “Blood exosomes as a tool for monitoring treatment efficacy and progression of neurodegenerative diseases,” *Neural regeneration research*, vol. 14, no. 1, p. 72, 2019.

[13] P. R. Srinivas, B. S. Kramer, and S. Srivastava, “Trends in biomarker research for cancer detection,” *Lancet Oncology*, vol. 2, no. 11, pp. 698–704, 2001.

[14] A. Sharma and S. K. Lal, "Zika virus: Transmission, detection, control, and prevention," *Frontiers in Microbiology*, vol. 8, no. FEB, pp. 1–14, 2017.

[15] E. Alegre, L. Zubiri, J. L. Perez-Gracia, M. González-Cao, L. Soria, S. Martín-Algarra, and A. González, "Circulating melanoma exosomes as diagnostic and prognosis biomarkers," *Clinica Chimica Acta*, pp. 28–32.

[16] A. Schneider and M. Simons, "Exosomes: vesicular carriers for intercellular communication in neurodegenerative disorders," *Cell Tissue Research*.

[17] D. R. Walt, "Optical Methods for Single Molecule Detection and Analysis," *Analytical Chemistry*, 2012.

[18] S. W. Hell, "Far-field optical nanoscopy." *Science (New York, N.Y.)*, vol. 316, no. 5828, pp. 1153–1158, 2007.

[19] E. Rittweger, K. Y. Han, S. E. Irvine, C. Eggeling, and S. W. Hell, "STED microscopy reveals crystal colour centres with nanometric resolution," *Nature Photonics*, vol. 3, no. 3, pp. 144–147, 2009.

[20] S. W. Hell and J. Wichmann, "Breaking the diffraction resolution limit by stimulated emission: stimulated-emission-depletion fluorescence microscopy," *Optics Letters*, no. 11, p. 780.

[21] M. J. Rust, M. Bates, and X. Zhuang, "Sub-diffraction-limit imaging by stochastic optical reconstruction microscopy (STORM)," *Nature Methods*, vol. 3, no. 10, pp. 793–795, 2006.

[22] S. Van De Linde, A. Löschberger, T. Klein, M. Heidbreder, S. Wolter, M. Heilemann, and M. Sauer, "Direct stochastic optical reconstruction microscopy with standard fluorescent probes," *Nature Protocols*, vol. 6, no. 7, pp. 991–1009, 2011.

[23] E. Betzig, G. H. Patterson, R. Sougrat, O. W. Lindwasser, S. Olenych, J. S. Bonifacino, M. W. Davidson, J. Lippincott-Schwartz, and H. F. Hess, "Imaging Intracellular Fluorescent Proteins at Nanometer Resolution," *Science*, no. 5793, pp. 1642–1645.

[24] L. Yin, W. Wang, S. Wang, F. Zhang, S. Zhang, and N. Tao, "How does fluorescent labeling affect the binding kinetics of proteins with intact cells?" *Biosensors and Bioelectronics*, pp. 412–416.

[25] M. P. Clausen and B. C. Lagerholm, "The probe rules in single particle tracking." *Current protein & peptide science*, no. 8, pp. 699–713.

[26] M. Á. Aguirre, K. D. Long, N. Li, S. L. Manoto, and B. T. Cunningham, "Detection and Digital Resolution Counting of Nanoparticles with Optical Resonators and Applications in Biosensing," *Chemsensors*, vol. 6, no. 13, pp. 1–26, 2018.

[27] D. Bachurski, M. Schuldner, P. H. Nguyen, A. Malz, K. S. Reiners, P. C. Grenzi, F. Babatz, A. C. Schauss, H. P. Hansen, M. Hallek, and E. Pogge von Strandmann, "Extracellular vesicle measurements with nanoparticle tracking analysis?An accuracy and repeatability comparison between NanoSight NS300 and ZetaView," *Journal of Extracellular Vesicles*, no. 1.

[28] J. A. Gallego-Urrea, J. Tuoriniemi, and M. Hassellöv, “Applications of particle-tracking analysis to the determination of size distributions and concentrations of nanoparticles in environmental, biological and food samples,” *TrAC Trends in Analytical Chemistry*, vol. 30, no. 3, pp. 473–483, 2011.

[29] “Nanoparticle tracking analysis nta.” [Online]. Available: https://www.malvernpanalytical.com/en/products/technology/nanoparticle-tracking-analysis

[30] J. Lee, W. Shen, K. Payer, T. P. Burg, and S. R. Manalis, “Toward attogram mass measurements in solution with suspended nanochannel resonators,” *Nano letters*, vol. 10, no. 7, pp. 2537–2542, 2010.

[31] S. Olcum, N. Cermak, S. C. Wasserman, K. S. Christine, H. Atsumi, K. R. Payer, W. Shen, J. Lee, A. M. Belcher, S. N. Bhatia, and S. R. Manalis, “Weighing nanoparticles in solution at the attogram scale,” *Proceedings of the National Academy of Sciences*, vol. 111, no. 4, pp. 1310–1315, 2014.

[32] S. Olcum, N. Cermak, and S. R. Manalis, “Precision mass measurements in solution reveal properties of single cells and bioparticles,” in *2015 IEEE International Electron Devices Meeting (IEDM)*. IEEE, 2015, pp. 13–5.

[33] S. Wang, X. Shan, U. Patel, X. Huang, J. Lu, J. Li, and N. Tao, “Label-free imaging, detection, and mass measurement of single viruses by surface plasmon resonance,” *Proceedings of the National Academy of Sciences*, vol. 107, no. 37, pp. 16 028–16 032, 2010.

[34] A. M. Maley, G. J. Lu, M. G. Shapiro, and R. M. Corn, “Characterizing Single Polymeric and Protein Nanoparticles with Surface Plasmon Resonance Imaging Measurements,” *ACS Nano*, vol. 11, no. 7, pp. 7447–7456, 2017.

[35] W. Zhang, L. Huang, C. Santschi, and O. J. Martin, “Trapping and sensing 10 nm metal nanoparticles using plasmonic dipole antennas,” *Nano Letters*, vol. 10, no. 3, pp. 1006–1011, 2010.

[36] E. Kim, M. D. Baaske, and F. Vollmer, “Towards next-generation label-free biosensors: recent advances in whispering gallery mode sensors,” *Lab on a Chip*, no. 7, pp. 1190–1205.

[37] F. Vollmer and S. Arnold, “Whispering-gallery-mode biosensing: Label-free detection down to single molecules,” *Nature Methods*, vol. 5, no. 7, pp. 591–596, 2008.

[38] J. Su, A. F. Goldberg, and B. M. Stoltz, “Label-free detection of single nanoparticles and biological molecules using microtoroid optical resonators,” *Light: Science & Applications*, no. 1, p. e16001.

[39] O. Mudanyali, E. Mcleod, W. Luo, A. Greenbaum, A. F. Coskun, Y. Hennequin, C. P. Allier, and A. Ozcan, “Wide-field optical detection of nanoparticles using on-chip microscopy and self-assembled nanolenses,” *Nature Photonics*, vol. 7, no. 3, pp. 247–254, 2013.

[40] M. U. Daloglu, A. Ray, Z. Gorocs, M. Xiong, R. Malik, G. Bitan, E. Mcleod, and

A. Ozcan, “Computational On-Chip Imaging of Nanoparticles and Biomolecules using Ultraviolet Light.”

[41] R. W. Taylor and V. Sandoghdar, “Interferometric Scattering Microscopy: Seeing Single Nanoparticles and Molecules via Rayleigh Scattering,” *Nano Letters*, vol. 19, no. 8, pp. 4827–4835, 2019.

[42] O. Avci, N. Ünlü, A. Özkumur, and M. Ünlü, “Interferometric Reflectance Imaging Sensor (IRIS)?A Platform Technology for Multiplexed Diagnostics and Digital Detection,” *Sensors*, no. 7, pp. 17 649–17 665.

[43] C. L. Hsieh, “Label-free, ultrasensitive, ultrahigh-speed scattering-based interferometric imaging,” *Optics Communications*, no. March, pp. 69–74.

[44] M. Delor, H. L. Weaver, Q. Yu, and N. S. Ginsberg, “Imaging material functionality through three-dimensional nanoscale tracking of energy flow,” *Nature materials*, pp. 1–7, 2019.

[45] C. A. Poynton, “Smpte tutorial:?gamma? and its disguises: The nonlinear mappings of intensity in perception, crts, film, and video,” *SMPTE journal*, vol. 102, no. 12, pp. 1099–1108, 1993.

[46] H. Siedentopf and R. Zsigmondy, “Uber sichtbarmachung und größenbestimmung ultramikoskopischer teilchen, mit besonderer anwendung auf goldrubingläser,” *Annalen der Physik*, vol. 315, no. 1, pp. 1–39, 1902.

[47] G. G. Daaboul, D. S. Freedman, S. M. Scherr, E. Carter, A. Rosca, D. Bernstein, C. E. Mire, K. N. Agans, T. Hoenen, T. W. Geisbert, M. Selim Ünlü, and J. H. Connor, "Enhanced light microscopy visualization of virus particles from Zika virus to filamentous ebolaviruses," *PLoS ONE*, vol. 12, no. 6, pp. 1–15, 2017.

[48] G. G. Daaboul, P. Gagni, L. Benussi, P. Bettotti, M. Ciani, M. Cretich, D. S. Freedman, R. Ghidoni, A. Y. Ozkumur, C. Piotto, D. Prosperi, B. Santini, M. Selim Ünlü, and M. Chiari, "Digital Detection of Exosomes by Interferometric Imaging," *Scientific Reports*.

[49] M. Piliarik and V. Sandoghdar, "Direct optical sensing of single unlabelled proteins and super-resolution imaging of their binding sites." *Nature communications*, p. 4495.

[50] P. Kukura, H. Ewers, C. Müller, A. Renn, A. Helenius, and V. Sandoghdar, "High-speed nanoscopic tracking of the position and orientation of a single virus," *Nature Methods*, no. 12, pp. 923–927.

[51] G. de Wit, J. S. H. Danial, P. Kukura, and M. I. Wallace, "Dynamic label-free imaging of lipid nanodomains," *Proceedings of the National Academy of Sciences*, no. 40, pp. 12 299–12 303.

[52] O. Avci, M. I. Campana, C. Yurdakul, and M. Selim Ünlü, "Pupil function engineering for enhanced nanoparticle visibility in wide-field interferometric microscopy," *Optica*, no. 2, pp. 247–254.

[53] J. T. Trueb, O. Avci, D. Sevenler, J. H. Connor, and M. S. Ünlü, "Robust

Visualization and Discrimination of Nanoparticles by Interferometric Imaging," *IEEE Journal of Selected Topics in Quantum Electronics*, vol. 23, no. 2, 2017.

[54] U. Aygun, O. Avci, E. Seymour, D. D. Sevenler, H. Urey, M. S. Ünlü, and A. Y. Ozkumur, "Low cost flatbed scanner label-free biosensor," in *Optics and Biophotonics in Low-Resource Settings II*, vol. 9699, 2016, p. 969906.

[55] U. Aygun, O. Avci, E. Seymour, H. Urey, M. Ünlü, and A. Ozkumur, "Label-Free and High-Throughput Detection of Biomolecular Interactions Using a Flatbed Scanner Biosensor," *ACS Sensors*, vol. 2, no. 10, 2017.

[56] U. Aygun, H. Urey, and A. Yalcin Ozkumur, "Label-free detection of nanoparticles using depth scanning correlation interferometric microscopy," *Scientific Reports*, 2019.

[57] M. Cretich, F. Damin, and M. Chiari, "Protein microarray technology: how far off is routine diagnostics?" *The Analyst*, no. 3, pp. 528–542.

[58] X. Fan, I. M. White, S. I. Shopova, H. Zhu, J. D. Suter, and Y. Sun, "Sensitive optical biosensors for unlabeled targets: A review," *analytica chimica acta*, vol. 620, no. 1-2, pp. 8–26, 2008.

[59] G. G. Daaboul, R. S. Vedula, S. Ahn, C. Lopez, A. Reddington, E. Ozkumur, and M. S. Ünlü, "LED-based interferometric reflectance imaging sensor for quantitative dynamic monitoring of biomolecular interactions." *Biosensors & bioelectronics*, no. 5, pp. 2221–7, jan.

[60] E. Ozkumur, J. W. Needham, D. a. Bergstein, R. Gonzalez, M. Cabodi, J. M. Gershoni, B. B. Goldberg, and M. S. Unlü, "Label-free and dynamic detection of biomolecular interactions for high-throughput microarray applications." *Proceedings of the National Academy of Sciences of the United States of America*, vol. 105, no. 23, pp. 7988–7992, 2008.

[61] J. De Feijter, d. J. Benjamins, and F. Veer, "Ellipsometry as a tool to study the adsorption behavior of synthetic and biopolymers at the air–water interface," *Biopolymers: Original Research on Biomolecules*, vol. 17, no. 7, pp. 1759–1772, 1978.

[62] J. Piehler, A. Brecht, and G. Gauglitz, "Affinity detection of low molecular weight analytes," *Analytical Chemistry*, vol. 68, no. 1, pp. 139–143, 1996.

[63] E. Ozkumur, A. Yalçin, M. Cretich, C. A. Lopez, D. A. Bergstein, B. B. Goldberg, M. Chiari, and M. S. Unlü, "Quantification of DNA and protein adsorption by optical phase shift." *Biosensors & bioelectronics*, vol. 25, pp. 167–172, 2009.

[64] G. Comina, A. Suska, and D. Filippini, "Towards autonomous lab-on-a-chip devices for cell phone biosensing," *Biosensors and Bioelectronics*, pp. 1153–1167.

[65] J. C. Contreras-Naranjo, Q. Wei, and A. Ozcan, "Mobile Phone-Based Microscopy , Sensing , and Diagnostics," *IEEE Journal of Selected Topics in Quantum ELectronics*, vol. 22, no. 3, pp. 392–405, 2016.

[66] V. Oncescu, M. Mancuso, and D. Erickson, “Cholesterol testing on a smartphone,” *Lab Chip*, no. 4, pp. 759–763.

[67] S. Feng, R. Caire, B. Cortazar, M. Turan, and A. Wong, “Terms of Use Immunochromatographic Diagnostic Test Analysis Using Google Glass,” no. 3, pp. 3069–3079, 2014.

[68] A. Ozcan, “Mobile phones democratize and cultivate next-generation imaging, diagnostics and measurement tools.” *Lab on a chip*, pp. 3187–3194.

[69] Z. Göröcs, Y. Ling, M. D. Yu, D. Karahalios, K. Mogharabi, K. Lu, Q. Wei, and A. Ozcan, “Giga-pixel fluorescent imaging over an ultra-large field-of-view using a flatbed scanner.” *Lab on a chip*, no. 22, pp. 4460–6, nov.

[70] D. Sevenler and M. S. Ünlü, “Numerical techniques for high-throughput reflectance interference biosensing,” *Journal of Modern Optics*, pp. 1–6.

[71] V. Romanov, S. N. Davidoff, A. R. Miles, D. W. Grainger, B. K. Gale, and B. D. Brooks, “A critical comparison of protein microarray fabrication technologies,” *Analyst*, no. 6, pp. 1303–1326.

[72] S. L. Seurynck-Servoss, A. M. White, C. L. Baird, K. D. Rodland, and R. C. Zangar, “Evaluation of surface chemistries for antibody microarrays,” *Analytical Biochemistry*, vol. 371, no. 1, pp. 105–115, 2007.

[73] C. Boozer, J. Ladd, S. Chen, S. Jiang, and S. Anal, “DNA Directed Protein Immobilization for Simultaneous Detection of Multiple Analytes by Surface Plas-

mon Resonance Biosensor," *Analytical Chemistry*, vol. 78, no. 5, pp. 1515–1519, 2006.

[74] E. Seymour, G. G. Daaboul, X. Zhang, S. M. Scherr, N. L. Ünlü, J. H. Connor, and M. S. Ünlü, "DNA-Directed Antibody Immobilization for Enhanced Detection of Single Viral Pathogens," *Analytical Chemistry*, p. 151007095420006.

[75] L. V. Wang and H.-i. Wu, *Biomedical Optics: principles and imaging.* Wiley, 2007.

[76] N. Metropolis, A. W. Rosenbluth, M. N. Rosenbluth, A. H. Teller, and E. Teller, "Equation of state calculations by fast computing machines," *The journal of chemical physics*, vol. 21, no. 6, pp. 1087–1092, 1953.

[77] H. Haario, M. Laine, A. Mira, and E. Saksman, "Dram: efficient adaptive mcmc," *Statistics and Computing*, vol. 16, no. 4, pp. 339–354, 2006.

[78] O. Avci, R. Adato, A. Y. Ozkumur, and M. S. Ünlü, "Physical modeling of interference enhanced imaging and characterization of single nanoparticles," *Optics Express*, no. 6, p. 6094.

[79] L. Novotny and B. Hecht, *Principles of nano-optics.* Cambridge university press, 2012.

[80] K. Denzer, M. Kleijmeer, H. Heijnen, W. Stoorvogel, and H. Geuze, "Exosome: From Internal Vesicle of the Multivesicular Body to Intercellular Signaling Device," *Journal of Cell Science*, vol. 113, no. 19, pp. 3365–3374, 2000.

[81] Y. H. Soung, S. Ford, V. Zhang, and J. Chung, "Exosomes in cancer diagnostics," *Cancers*, vol. 9, no. 1, 2017.

[82] S. A. Melo, L. B. Luecke, C. Kahlert, A. F. Fernandez, S. T. Gammon, J. Kaye, V. S. LeBleu, E. A. Mittendorf, J. Weitz, N. Rahbari, C. Reissfelder, C. Pilarsky, M. F. Fraga, D. Piwnica-Worms, and R. Kalluri, "Glypican-1 identifies cancer exosomes and detects early pancreatic cancer," *Nature*, no. 7559, pp. 177–182.

[83] M. Tucci, F. Mannavola, A. Passarelli, L. S. Stucci, M. Cives, and F. Silvestris, "Exosomes in melanoma: A role in tumor progression, metastasis and impaired immune system activity," *Oncotarget*, vol. 9, no. 29, pp. 20 826–20 837, 2018.

[84] C. Masaoutis, C. Mihailidou, G. Tsourouflis, and S. Theocharis, "Exosomes in lung cancer diagnosis and treatment. From the translating research into future clinical practice," *Biochimie*, vol. 151, pp. 27–36, 2018.

[85] M. K. S. Tang and A. S. T. Wong, "Exosomes: Emerging biomarkers and targets for ovarian cancer," *Cancer Letters*, no. 1, pp. 26–33.

[86] J. Pan, M. Ding, K. Xu, C. Yang, and L. J. Mao, "Exosomes in diagnosis and therapy of prostate cancer," *Oncotarget*, vol. 8, no. 57, pp. 97 693–97 700, 2017.

[87] F. Bray, J. Ferlay, I. Soerjomataram, R. L. Siegel, L. A. Torre, and A. Jemal, "Global cancer statistics 2018: GLOBOCAN estimates of incidence and mortality worldwide for 36 cancers in 185 countries," *CA: A Cancer Journal for Clinicians*, vol. 68, no. 6, pp. 394–424, 2018.

[88] American Cancer Society, "Cancer Facts & Figures 2019," p. 76.

[89] J. D. Schiffman, P. G. Fisher, and P. Gibbs, "Early detection of cancer: past, present, and future," *American Society of Clinical Oncology Educational Book*, vol. 35, no. 1, pp. 57–65.

[90] G. Brock, E. Castellanos-Rizaldos, L. Hu, C. Coticchia, and J. Skog, "Liquid biopsy for cancer screening, patient stratification and monitoring," *Translational Cancer Research*, vol. 4, no. 3, pp. 280–290, 2015.

[91] J. Ko, E. Carpenter, and D. Issadore, "Detection and isolation of circulating exosomes and microvesicles for cancer monitoring and diagnostics using micro-/nano-based devices." *The Analyst*, pp. 450–460.

[92] K. W. Witwer, E. I. Buzas, L. T. Bemis, A. Bora, C. Lässer, J. Lötvall, E. N. Nolte-?t Hoen, M. G. Piper, S. Sivaraman, J. Skog *et al.*, "Standardization of sample collection, isolation and analysis methods in extracellular vesicle research," *Journal of extracellular vesicles*, vol. 2, no. 1, p. 20360, 2013.

[93] C. Y. Soo, Y. Song, Y. Zheng, E. C. Campbell, A. C. Riches, F. Gunn-Moore, and S. J. Powis, "Nanoparticle tracking analysis monitors microvesicle and exosome secretion from immune cells," *Immunology*, vol. 136, no. 2, pp. 192–197, 2012.

[94] F. Liu, O. Vermesh, V. Mani, T. J. Ge, S. J. Madsen, A. Sabour, E.-C. Hsu, G. Gowrishankar, M. Kanada, J. V. Jokerst *et al.*, "The exosome total isolation chip," *ACS nano*, vol. 11, no. 11, pp. 10 712–10 723, 2017.

[95] V. Brinkmann, U. Reichard, C. Goosmann, B. Fauler, Y. Uhlemann, D. S.

Weiss, Y. Weinrauch, and A. Zychlinsky, "Neutrophil extracellular traps kill bacteria," *Science*, vol. 303, no. 5663, pp. 1532–1535, 2004.

[96] B. Cortjens, J. van Woensel, and R. Bem, "Neutrophil extracellular traps in respiratory disease: guided anti-microbial traps or toxic webs?" *Paediatric respiratory reviews*, vol. 21, pp. 54–61, 2017.

[97] J. Park, R. W. Wysocki, Z. Amoozgar, L. Maiorino, M. R. Fein, J. Jorns, A. F. Schott, Y. Kinugasa-Katayama, Y. Lee, N. H. Won *et al.*, "Cancer cells induce metastasis-supporting neutrophil extracellular dna traps," *Science translational medicine*, vol. 8, no. 361, pp. 361ra138–361ra138, 2016.

[98] G. Schönrich and M. J. Raftery, "Neutrophil extracellular traps go viral," *Frontiers in immunology*, vol. 7, p. 366, 2016.

[99] T. A. Fuchs, A. Brill, D. Duerschmied, D. Schatzberg, M. Monestier, D. D. Myers, S. K. Wrobleski, T. W. Wakefield, J. H. Hartwig, and D. D. Wagner, "Extracellular dna traps promote thrombosis," *Proceedings of the National Academy of Sciences*, vol. 107, no. 36, pp. 15 880–15 885, 2010.

[100] A. A. Al-Haidari, N. Algethami, M. Lepsenyi, M. Rahman, I. Syk, and H. Thorlacius, "Neutrophil extracellular traps promote peritoneal metastasis of colon cancer cells," *Oncotarget*, vol. 10, no. 12, p. 1238, 2019.

[101] Y. Döring, O. Soehnlein, and C. Weber, "Neutrophil extracellular traps in atherosclerosis and atherothrombosis," *Circulation research*, vol. 120, no. 4, pp. 736–743, 2017.

[102] L. Wang, X. Zhang, X. Zhou, and D. Wang, "Hyperglycemia induces neutrophil extracellular traps formation through an nadph oxidase-dependent pathway in diabetic retinopathy," *Frontiers in immunology*, vol. 9, p. 3076, 2018.

[103] N. de Buhr and M. von Köckritz-Blickwede, "How neutrophil extracellular traps become visible," *Journal of immunology research*, vol. 2016, 2016.

[104] S. Bruns, O. Kniemeyer, M. Hasenberg, V. Aimanianda, S. Nietzsche, A. Thywißen, A. Jeron, J.-P. Latgé, A. A. Brakhage, and M. Gunzer, "Production of extracellular traps against aspergillus fumigatus in vitro and in infected lung tissue is dependent on invading neutrophils and influenced by hydrophobin roda," *PLoS pathogens*, vol. 6, no. 4, p. e1000873, 2010.

[105] M. Böhmer and J. Enderlein, "Orientation imaging of single molecules by wide-field epifluorescence microscopy," *Journal of the Optical Society of America B*, vol. 20, no. 3, p. 554, 2007.

[106] H. Uji-i, A. Deres, B. Muls, S. Melnikov, J. Enderlein, and J. Hofkens, "Defocused imaging in wide-field fluorescence microscopy," in *Fluorescence of Supermolecules, Polymers, and Nanosystems.* Springer, 2007, pp. 257–284.

APPENDIX

A.1 *Flatbed Scanner Characterization*

Determination of spatial resolution

Resolutions of flatbed scanners are reported in dot per inch (dpi), which is mainly related with the interpolated output image size. We implemented ISO 12233 technique to determine the spatial resolution of our hardware platform. We imaged a slightly (5°) tilted edge which is between etched silicon and oxide region as show in Figure A.1. Image is upsampled, rotated by using Affine transform. Edge spread function, line spread function and modulation transfer function is calculated as shown in Figure A.1c-e, respectively. MTF50 point determined as 0.42 cycle/pixel width, which corresponds to 0.0792 $cycle/\mu m$ (pixel width of 5.3 μm). Corresponding spatial resolution is 12.62 μm.

Determination of Depth of Field

As GRIN lens array is used, depth of field of CIS scanners is low. Scanner glass provides a fixed distance between the lens array and the document to achieve one-to-one imaging. In order to determine the depth of field of the imaging system, sample is tilted and scanned. As shown in Figure A.2-b, alignment marks on the sensor chip is only visible in a relatively narrow z-distance range ($\sim$ 250 μm).

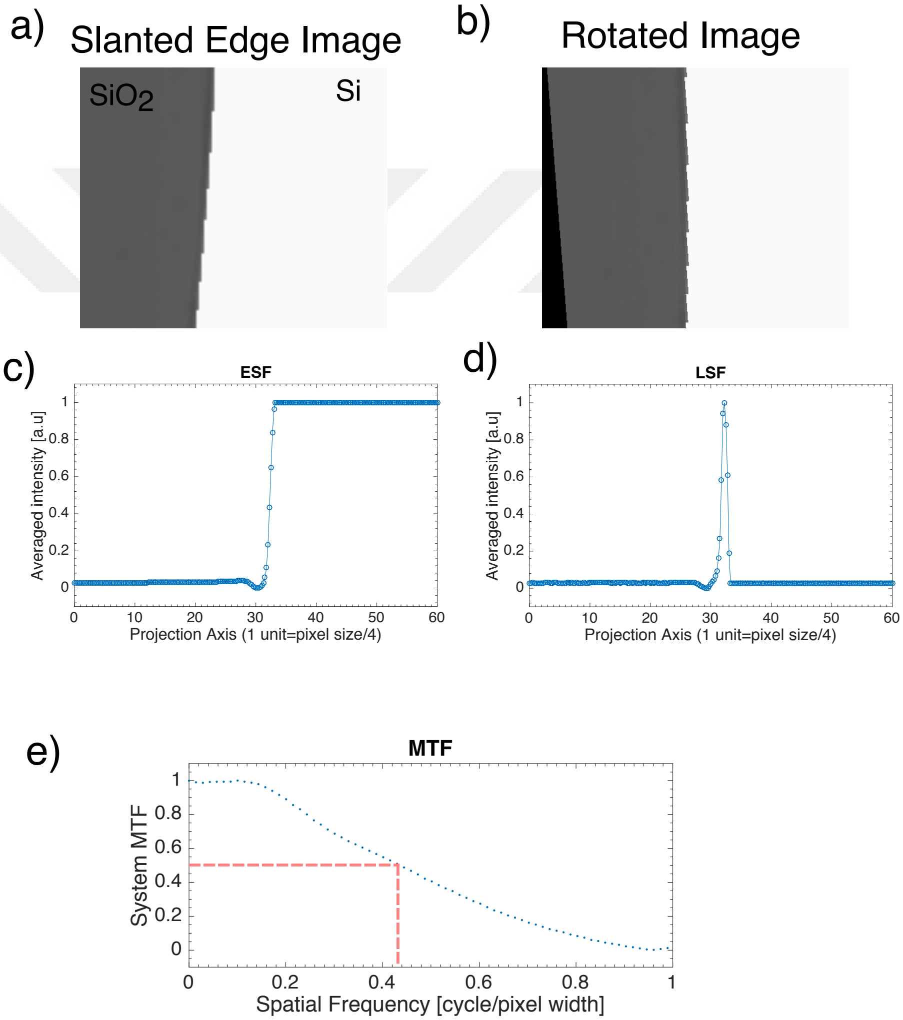

Figure A.1: Spatial resolution is determined by applying slanted edge technique

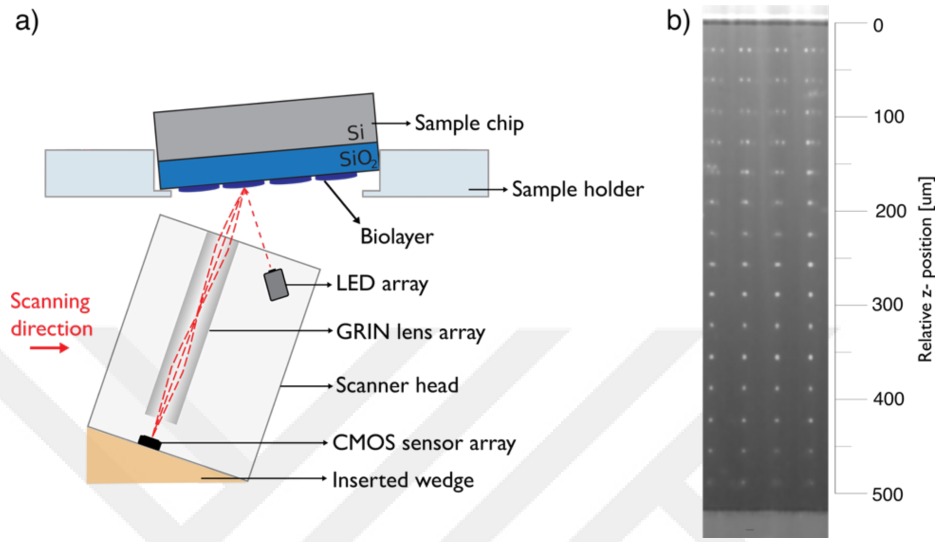

Figure A.2: a) Measurement configuration b) Image of the tilted sensor chip

A.2 Theoretical Model

In [79], PSF of a single scatterer on a substrate is given. This section closely follows their derivation, except defocus effect is also considered [105, 106]. A point dipole can be imaged using an optical system shown in Figure A.3. Radiated wave is collected by first lens ($f_1 = f$) and then focused to an image sensor by second lens ($f_2 = f' > f$). Unit vectors are defined as

$$\hat{\mathbf{n}}_\rho = \begin{pmatrix} \cos\phi \\ \sin\phi \\ 0 \end{pmatrix} ; \hat{\mathbf{n}}_\phi = \begin{pmatrix} -\sin\phi \\ \cos\phi \\ 0 \end{pmatrix} ; \hat{\mathbf{n}}_\theta = \begin{pmatrix} \cos\theta\cos\phi \\ \cos\theta\sin\phi \\ -sin\theta \end{pmatrix} ; \tag{A.1}$$

in terms of cartesian coordinates. Radiation at far field can be written as (Eq.10.32) in [79]),

$$\mathbf{E}_\infty(\theta,\phi) = \begin{pmatrix} E_\theta \\ E_\phi \end{pmatrix} = \frac{k_1^2}{4\pi\epsilon_0\epsilon_1}\frac{e^{ik_1r}}{r}\begin{pmatrix} \Phi_2\cos\theta\cos\phi & \Phi_2\cos\theta\sin\phi & -\Phi_1\sin\theta \\ -\Phi_3\sin\phi & \Phi_3\cos\phi & 0 \end{pmatrix}\begin{bmatrix} \mu_x \\ \mu_y \\ \mu_z \end{bmatrix} \tag{A.2}$$

where

$$\Phi_1 = [e^{-ik_1z_0\cos\theta} + r^p(\theta)e^{ik_1z_0\cos\theta}]e^{ik_1z_d\cos\theta} \tag{A.3a}$$

$$\Phi_2 = [e^{-ik_1z_0\cos\theta} - r^p(\theta)e^{ik_1z_0\cos\theta}]e^{ik_1z_d\cos\theta} \tag{A.3b}$$

$$\Phi_3 = [e^{-ik_1z_0\cos\theta} + r^s(\theta)e^{ik_1z_0\cos\theta}]e^{ik_1z_d\cos\theta} \tag{A.3c}$$

Here, effect of defocus (z_d) is also introduced as a phase term [105, 106].

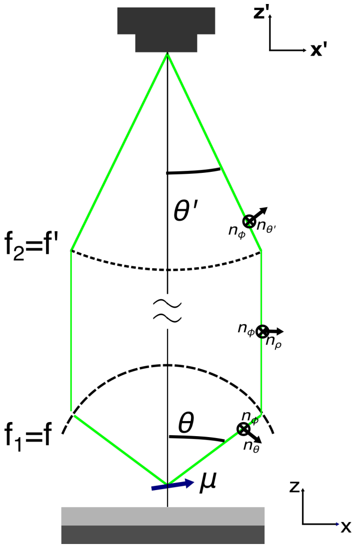

Figure A.3: Geometrical representation of the imaging system and definition of coordinates

After refraction from the first lens field will be,

$$\mathbf{E}_{\infty}^{(\mathbf{1})}(\theta,\phi)=[E_{\theta}.\hat{\mathbf{n}}_{\rho}+E_{\phi}.\hat{\mathbf{n}}_{\phi}]\sqrt{\frac{n_1}{\cos\theta}} \tag{A.4}$$

similarly after refraction from second lens, field can be written as

$$\mathbf{E}_{\infty}^{(\mathbf{2})}(\theta',\phi)=[E_{\theta}.\hat{\mathbf{n}}_{\theta'}+E_{\phi}.\hat{\mathbf{n}}_{\phi}]\sqrt{\frac{n_1\cos\theta'}{n_3\cos\theta}} \tag{A.5}$$

and field distribution near focal plane of second lens can be found by applying a near to far field transform and integrating (Eq.3.47 in [79])

$$\mathbf{E}(\rho',\psi',z')=\frac{ik_3f'e^{-ik_3f'}}{2\pi}\int_0^{\theta'_{\max}}\int_0^{2\pi}\mathbf{E}_{\infty}^{(\mathbf{2})}(\theta',\phi)e^{ik_{z3}z}e^{ik_3\rho'\sin\theta'\cos(\phi-\psi')}\sin\theta' d\theta' d\phi \tag{A.6}$$

and from Figure A.3, it is apparent that θ' and θ are related with each other such as

$$\frac{\sin\theta}{\sin\theta'}=\frac{f'}{f}=M \tag{A.7}$$

where M is magnification of the imaging system. Furthermore k_{z3} in Eq. (A.6) can be written as in terms of θ

$$k_{z3}=k_3\sqrt{1-\sin^2\theta'}=k_3\sqrt{1-\sin^2\theta(\frac{f}{f'})^2} \tag{A.8}$$

which can be further simplified using paraxial approximation

$$k_{z3}\simeq k_3-\frac{k_3}{2}\sin^2\theta(\frac{f}{f'})^2 \tag{A.9}$$

Using these simplifications and changing the variables ($d\theta' = f/f' \cos\theta d\theta$ and $\cos\theta' \simeq 1$), Eq. (A.6) can be written as

$$\mathbf{E}(\rho', \psi', z') = \frac{ik_3 f' e^{-ik_3 f'}}{2\pi}(\frac{f}{f'})^2 ...$$

$$... \int_0^{\theta_{max}} \int_0^{2\pi} \mathbf{E}_\infty^{(2)}(\theta, \phi) e^{ik_3 z'} e^{-ik_3/2 \sin^2\theta (f/f')^2 z'} e^{ik_3 \rho' \sin\theta f/f' \cos(\phi-\psi')} \sin\theta \cos\theta d\theta d\phi \quad \text{(A.10)}$$

Solving this integral together with the Eq. (A.5) will give field distribution near image plane due to arbitrary point dipole near dielectric substrate.

In this work to simplify the model, we assume that the dipole orientation is in horizontal direction (i.e. x-oriented). For x oriented dipole ($\mu = \mu_x \hat{\mathbf{n}}_x$) far field after refraction from the focusing lens (Eq. (A.5)) can be written as

$$\mathbf{E}_{\infty,\mu_x}^{(2)}(\theta, \phi) = \frac{k_1^2}{4\pi\epsilon_0\epsilon_1} \frac{e^{ik_1 f}}{f} [\Phi_2 \cos\theta \cos\phi \hat{\mathbf{n}}_{\theta'} - \Phi_3 \sin\phi \hat{\mathbf{n}}_\phi] \sqrt{\frac{n_1 \cos\theta'}{n_3 \cos\theta}} \mu_x \quad \text{(A.11)}$$

and replacing unit vectors with their cartesian forms.

$$\mathbf{E}_{\infty,\mu_x}^{(2)}(\theta, \phi) = \frac{k_1^2}{4\pi\epsilon_0\epsilon_1} \frac{e^{ik_1 f}}{f} [\Phi_2 \cos\theta \cos\phi \begin{pmatrix} \cos\phi \\ \sin\phi \\ 0 \end{pmatrix} - \Phi_3 \sin\phi \begin{pmatrix} -\sin\phi \\ \cos\phi \\ 0 \end{pmatrix}] \sqrt{\frac{n_1 \cos\theta'}{n_3 \cos\theta}} \mu_x \quad \text{(A.12)}$$

$$\mathbf{E}_{\infty,\mu_x}^{(2)}(\theta, \phi) = \frac{1}{2} \frac{k_1^2}{4\pi\epsilon_0\epsilon_1} \frac{e^{ik_1 f}}{f} \begin{bmatrix} (\Phi_2 \cos\theta + \Phi_3) + (\cos\theta \Phi_2 - \Phi_3) \cos\ 2\phi \\ (\cos\theta \Phi_2 - \Phi_3) \sin\ 2\phi \\ 0 \end{bmatrix} \sqrt{\frac{n_1 \cos\theta'}{n_3 \cos\theta}} \mu_x \quad \text{(A.13)}$$

inserting (A.13) into (A.10) we can calculate the electric field near the focus. Here, using the following mathematical relations integrations can be simplified carrying out the integration over ϕ

$$\int_{0}^{2\pi} \cos(n\phi) e^{ix\cos(\phi-\psi)} d\phi = 2\pi(i^n) J_n(x)\cos(n\psi) \tag{A.14a}$$

$$\int_{0}^{2\pi} \sin(n\phi) e^{ix\cos(\phi-\psi)} d\phi = 2\pi(i^n) J_n(x)\sin(n\psi) \tag{A.14b}$$

where J_n is the n_{th} order Bessel function. Final expression contains integration over θ only

$$\mathbf{E}_{(\mu_x)}(\rho', \psi', z') = \frac{ik_3 f' e^{-ik_3 f'}}{2\pi} (\frac{f}{f'})^2 \frac{1}{2} \frac{k_1^2}{4\pi\epsilon_0\epsilon_1} \frac{e^{ik_1 f}}{f} . e^{k_3 z'} \sqrt{\frac{n_1}{n_3}} \begin{bmatrix} I_0 + I_2 \\ I_2' \\ 0 \end{bmatrix} \mu_x \tag{A.15}$$

where integrals (I_0, I_2 and I_2') are defined as

$$
\begin{aligned}
I_0 &= \int_0^{\theta_{max}}\int_0^{2\pi}(\Phi_2\cos\theta+\Phi_3)e^{-ik_3/2(f/f'\sin\theta)^2z'}e^{ik_3\rho'/M\sin\theta\cos(\phi-\psi')}\sin\theta\sqrt{\cos\theta}d\phi d\theta \\
&= \int_0^{\theta_{max}}(\Phi_2\cos\theta+\Phi_3)e^{-ik_3/2(f/f'\sin\theta)^2z'}2\pi J_0(k_3\rho' f/f'\sin\theta)\sin\theta\sqrt{\cos\theta}d\theta \qquad \text{(A.16a)}
\end{aligned}
$$

$$
\begin{aligned}
I_2 &= \int_0^{\theta_{max}}\int_0^{2\pi}(\Phi_2\cos\theta-\Phi_3)(\cos 2\phi)e^{-ik_3/2(f/f'\sin\theta)^2z'}e^{ik_3\rho' f/f'\sin\theta\cos(\phi-\psi')}\sin\theta\sqrt{\cos\theta}d\phi d\theta \\
&= -\cos(2\psi')\int_0^{\theta_{max}}(\Phi_2\cos\theta-\Phi_3)e^{-ik_3/2(f/f'\sin\theta)^2z'}2\pi J_2(k_3\rho' f/f'\sin\theta)\sin\theta\sqrt{\cos\theta}d\theta
\end{aligned}
\qquad \text{(A.16b)}
$$

$$
\begin{aligned}
I_2' &= \int_0^{\theta_{max}}\int_0^{2\pi}(\Phi_2\cos\theta-\Phi_3)(\sin 2\phi)e^{-ik_3/2(f/f'\sin\theta)^2z'}e^{ik_3\rho' f/f'\sin\theta\cos(\phi-\psi')}\sin\theta\sqrt{\cos\theta}d\phi d\theta \\
&= -\sin(2\psi')\int_0^{\theta_{max}}(\Phi_2\cos\theta-\Phi_3)e^{-ik_3/2(f/f'\sin\theta)^2z'}2\pi J_2(k_3\rho' f/f'\sin\theta)\sin\theta\sqrt{\cos\theta}d\theta
\end{aligned}
\qquad \text{(A.16c)}
$$

Magnitude of field distributions due to x- oriented dipole on image plane is shown in Figure A.3.

A.3 Additional NETs Images

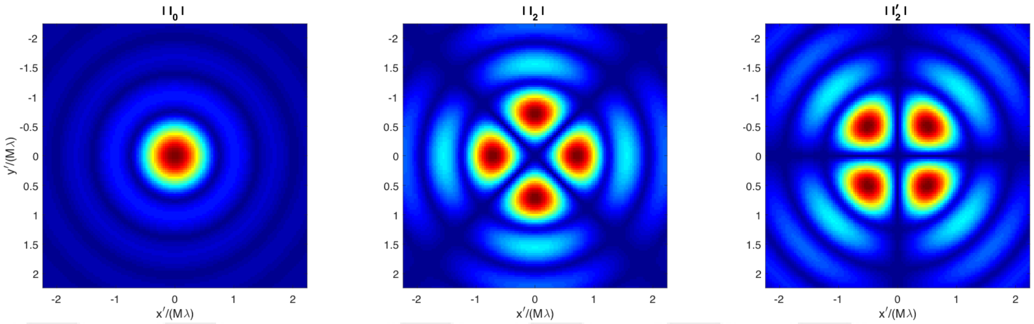

Figure A.4: Transfer function components for horizontal oriented dipole I_0, I_2 and I_2'

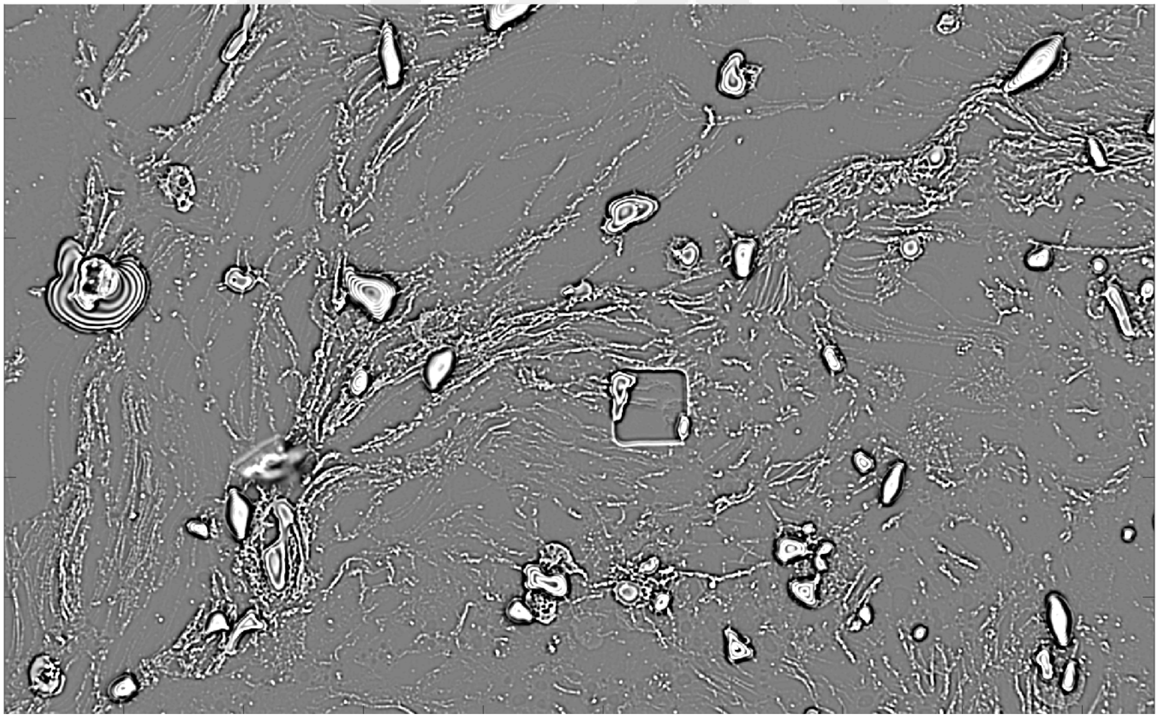

Figure A.5: Captured Neutrophil Extracellular Traps (NETs) Image

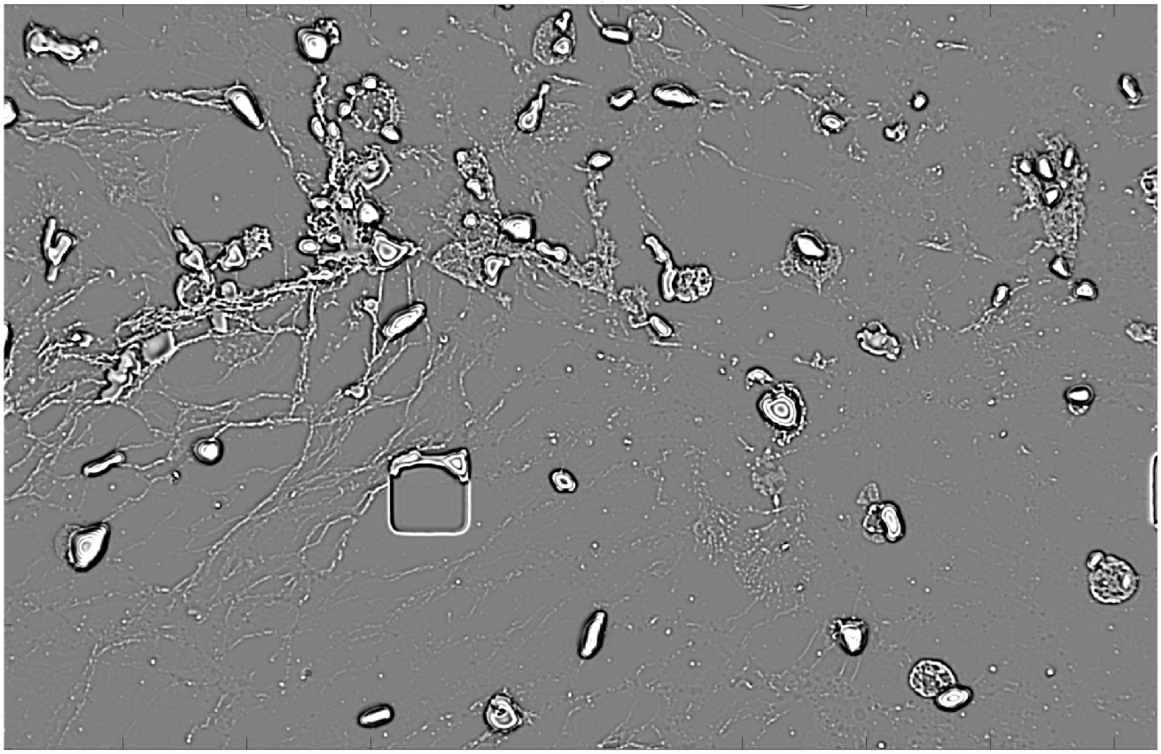

Figure A.6: Captured Neutrophil Extracellular Traps (NETs) Image